Sensing and interferometry, including design and characterisation of special optical fibres

Andrew Michie

A thesis submitted for the degree of
Doctor of Philosophy
at the University of Sydney
29th of August, 2008

The University of Sydney

Statement of Originality

To the best of my knowledge, this thesis contains no copy or paraphrase of work due to other persons, except where duly acknowledged.

None of this work has been presented for any degree at the University of Sydney or elsewhere.

Andrew Michie

Table of Contents

Chapter 1. Introduction 8
- 1.1 Historical background 8
- 1.2 Structure of this thesis 9
  - (a) Chapters 9
  - (b) Appendices 10
- 1.3 Technology background 11
- 1.4 Significance 12
- 1.5 Acknowledgements 12
  - (a) Work wholly attributed to others 13
  - (b) Work of the author and others 14
  - (c) Work wholly attributable to the author 14
- 1.6 Contributing publications 15

Chapter 2. Background 17
- 2.1 Non-linear polarisability 17
  - (a) Linear polarisability in dielectrics 17
  - (b) Non-linear polarisability in dielectrics 17
  - (c) Quadratic non-linearity 18
  - (d) Cubic non-linearity 19
- 2.2 The susceptibility tensor 20
- 2.3 The tensor elements and permutation symmetry 20
- 2.4 Electro-optics in non-linear dielectrics 21
- 2.5 Thermal poling of twin-hole optical fibre 22
- 2.6 Linear electro-optic response and polarisation dependence 23
- 2.7 Interferometric optical fibre sensing 24
- 2.8 Common mode rejection 25
  - (a) Sagnac interferometer 25
  - (b) Twin core fibre 26
  - (c) Two polarisation mode interferometer (TPI) 26
- 2.9 Voltage Sensing 27
  - (a) Introduction 27
- 2.10 Birefringence in optical fibres 29

Chapter 3. The low coherence interferometer and signal processing system 31
- 3.1 The Mach-Zehnder two polarisation interferometer (MZ-TPI) 31
- 3.2 The Michelson two polarisation interferometer (M-TPI) 33
- 3.3 The M-TPI for voltage sensing 34
- 3.4 The voltage sensor signal processing scheme 36
- 3.5 The fast phase finder algorithm 38
- 3.6 Fourier transform theory in brief 38

Chapter 4. Polarisation dependence of the linear electro-optic coefficient in thermally poled twin-hole silica fibre 41
- 4.1 Thermal poling background 41
- 4.2 Experiments 42
- 4.3 Discussion and conclusion 50

Chapter 5. Twin-hole fibre design considerations 52
- 5.1 Introduction 52
  - (a) Method 1 52

(b) Method 2 53
(c) Method 3 54
5.2 Mode field diameter in step index fibres 55
5.3 The twin-hole fibre cross section 56
5.4 Fourier Decomposition Method with Adjustable Boundary Conditions (FDMABC) results 57
5.5 Marcuse model results 59
5.6 Comparison with previous methods 60
5.7 Designing a new twin-hole fibre 60
5.8 Multi-wavelength interrogation of thermally poled twin-hole fibre 62
5.9 Conclusion 66
Chapter 6. Generation 1 of the voltage sensing and signal processing system 67
6.1 Introduction 67
6.2 Experiments 67
6.3 Results and discussion 68
6.4 Conclusion 72
Chapter 7. Generation 2 of the voltage sensing and signal processing system 74
7.1 Introduction 74
7.2 Generation 2 voltage sensing system design 74
7.3 Generation 2 operating wavelength 77
7.4 Generation 2 twin-hole fibre 78
7.5 Generation 2 signal processing implementation 79
7.6 Experiments 80
(a) The internal electrode test 81
(b) The parallel plate electrode test 84
(c) Coiled fibre lab sensor configuration 86
7.7 Conclusion 89
Chapter 8. Generation 3 of the voltage sensing and signal processing system 91
8.1 Introduction 91
8.2 Generation 3 voltage sensing system design 91
8.3 Interferometer wavelength sensitivity 93
8.4 Generation 3 twin-hole fibre 93
8.5 Helical coiling the double flat fibre 94
8.6 Experiments 95
(a) Results using a sample of OD-0265-FN @ 230µm diameter 95
(b) Results using a sample of OD-0265-FN @ 250µm diameter 101
Chapter 9. Temperature independent highly birefringent photonic crystal fibre 106
9.1 Introduction 106
9.2 Temperature dependence in HiBi fibres 107
(a) Bow-tie and Panda fibre 107
(b) Highly birefringent photonic crystal fibre 108
9.3 Methods 108
(a) Experiments 108
(b) Group and modal birefringence analysis 110
9.4 Results 113
(a) Temperature dependence experiments 113
(b) Determining the wavelength dependence of the HiBi-PCF 114
Chapter 10. Spun elliptically birefringent photonic crystal fibre for current sensing 117
10.1 Introduction 117

10.2 Elliptical birefringence 120
(a) Background 120
10.3 Current sensitivity 121
10.4 Measurement approach 122
(a) Introduction 122
(b) Birefringence measurement 123
(c) Temperature dependence measurements 124
10.5 Results and Discussion 124
10.6 Conclusion 126
Chapter 11. Conclusion 128
11.1 Interferometry 128
11.2 The signal processing system 129
11.3 The application to voltage sensing 129
11.4 Insights into poling 130
(a) Polarisation dependence 130
(b) Multi-wavelength experiments 131
11.5 The application to characterisation of HiBi PCFs 131
11.6 Opportunities for further research work 131
11.7 The commercial opportunity 132
Appendix A Non linear optics and tensors for poling 133
A.1 Notations, conventions and symmetry arguments 133
A.2 Electric impermeability, index ellipsoid, dielectric constant and refractive index 133
A.3 Alternative notations 135
A.4 Linking together the non-linear susceptibilities, and the Pockels and Kerr coefficients 136
Appendix B Tensors for poling – polarisation dependence, symmetry considerations and notation conventions 139
B.1 Power series 139
B.2 Poling optical fibre 140
B.3 Symmetries of the poled substance 144
(a) Isotropic 144
B.4 Neumann’s principle 148
B.5 Shorthand notation 149
B.6 Notation conventions and variations 149
Appendix C Phase and Group Birefringence in single mode fibres 151
(a) Phase and group birefringence 151
(b) Retardance in birefringent fibre 153
Appendix D References 154

Table of Figures

2-1 A typical twin-hole fibre cross section 23
2-2 Basic Sagnac interferometer 25
2-3 Alan Rogers' proposed all fibre voltage sensor configuration [25] 27
2-4 Coiled poled fibre illustration 28
2-5 Cross sections of bow-tie, Panda, and HiBi-PCF from left to right 30
3-1 The Mach-Zehnder two polarisation interferometer (MZ-TPI) 32
3-2 MZ-TPI output spectrum or interferogram 33
3-3 M-TPI configured using thermally poled twin-hole fibre 34
4-1 M-TPI used to determine the DLEO of the thermally poled twin-hole silica fibre 43
4-2 MZI with polarisation control 46
4-3 Measured $r33$ and $r31$ values. Data marked X and Y polarised light correspond to $r33$ and $r31$respectively. 47
4-4 Twin-hole fibre cross section 48
4-5 M-TPI input and output spectra with +125 and -125V DC applied across internal electrodes 49
4-6 Visualisation of the second order non-linear layer in thermally poled fibre, showing the wrapping around the core (image provided by Hong Lin An)[36, 37] ... 51
5-1 Images obtained from the literature using method 1. Corresponding authors for the images from left to right Alley & Brueck 1998, Myrén & Margulis 2005, and Blazkiewicz et al 2001 [17, 34, 44]. 53
5-2 Results obtained using method 2 by Kudlinski, Quiquempois et al[45-47] 54
5-3 Results obtained using method 3 showing a highly localised non-linear region partially surrounding the core [image provided by Honglin An and Fleming] 54
5-4 Reconstructed refractive index profile of the twin-hole fibre OD-0133-03A and cross sectional image showing the elliptical core and proximity to the anode hole 57
5-5 The FDMABC mode intensity profile at 834nm; intensity is shown on the z axis using arbitrary units 58
5-6 The FDMABC mode intensity profile at 1550nm; intensity is shown on the z axis using arbitrary units 59
5-7 Mode field diameter calculations using both the FDMABC method and the Marcuse model 60
5-8 Mode field diameter versus NA for core diameters of 1.6, 2.4, and 3.2 microns . 61
5-9 Mode field diameter versus NA for core diameters of 1.6, 2.4, and 3.2 microns . 62
5-10 The all fibre multi-wavelength Mach-Zehnder interferometer 63
5-11 OD-0133-03B fibre cross section 64
5-12 Linear electro-optic response at 4 different wavelengths 65
5-13 Linear electro-optic response versus wavelength 65
6-1 A schematic diagram of generation 1 of the voltage sensor signal processing system 68
6-2 Five cycle internal electrode AC test – 20 volt peak to peak 69
6-3 Five cycle internal electrode AC test – 80 volt peak to peak 69
6-4 Five cycle internal electrode AC test – 160 volt peak to peak 70
6-5 Five cycle internal electrode AC test – 240 volt peak to peak 70
6-6 Five cycle internal electrode AC test – 320 volt peak to peak 71
6-7 Five cycle internal electrode AC test – response linearity 72
7-1 Czerny-Turner monochromators or compact spectrometer 75

7-2 A typical interferogram operating in the 820 – 900nm band 76
7-3 The Spectral Products SM-820 compact spectrometer and custom interface board 77
7-4 Sony ILX-511 relative sensitivity versus wavelength...78
7-5 OD-0133-03B fibre cross section...79
7-6 Schematic diagram of generation 2 of the signal processing system 80
7-7 The Smart Digital Optics Pty Limited digital signal processing board.................80
7-8 Generation 2 logged output. 82
7-9 XY plot :- Optically measured voltage versus Test voltage (V RMS)..................83
7-10 Illustration of the parallel plate electrode, external field test 84
7-11 The parallel plate configuration sensing system response at 50Hz.....................85
7-12 Ghost view illustration of a field deployable voltage sensor showing the coiled poled silica fibre...87
7-13 OD-0133D cross section...88
7-14 coiled fibre configuration sensing system response at 50Hz...............................89
8-1 Schematic diagram of generation 2 of the signal processing system 92
8-2 Oriel compact spectrometer and interface electronics...92
8-3 OD-0265-FN fibre cross section...94
8-4 Double flat fibre coiling illustration 95
8-5 Internal electrode test for 1.35 m device 97
8-6 Plate electrode test for 1.35 m device...98
8-7 Left: Press board tubing and coiled double flat fibre, Right: Porcelain insulator and end electrode plates. 99
8-8 Left: Magnetic voltage transformer used to both generate and monitor the test voltage, Right: A coiled sensor being tested without the porcelain insulator............100
8-9 Coiled sensor test for 1.35 m device..100
8-10 Transient recording – test voltage switched on 101
8-11 Transient recording – test voltage switched off...102
8-12 Transient recording – switch on zoomed in...102
8-13 Transient recording – switch off zoomed in..103
8-14 Linearity test using 1 cycle averaging 104
8-15 Linearity test using 1 second averaging 104
8-16 Accuracy test showing amplitude measurement errors 105
8-17 Accuracy test showing phase measurement errors..105
9-1 A bow-tie fibre cross section clearly showing the dark bow-tie shaped borosilicate regions that form the stress applying parts 108
9-2 SEM image of the cross-section of the fibre 109
9-3 Experimental set up for measuring group birefringence 109
9-4 A typical interferogram as measured on the optical spectrum analyzer..............110
9-5 Temperature dependence of modal birefringence for a bow-tie fibre and HiBi-PCF 114
9-6 Birefringence as a function of wavelength of a bow-tie fibre and the HiBi-PCF115
10-1 Spun Hi-Bi photonic crystal fibre cross-section..119
10-2 Representation of polarisation states and birefringence in Poincaré space 121
10-3 Experimental set up for measuring the ellipticity of the spun HiBi PCF 123
10-4 Interferograms recorded both when the periodic modulation is extinguished and also when it is maximised..125
10-5 Group birefringence versus temperature for both a conventional stress birefringence Panda fibre and the Spun HiBi -PCF..126

Chapter 1. Introduction

This thesis presents my work in the area of optical fibre sensing, and optical fibre design and characterisation along with the interferometric and signal processing techniques that were developed along the way. This work has resulted through highly rewarding and productive collaborations and my collaborators and their contributions are acknowledged in the following text.

1.1 Historical background

At the outset, the focus of this work was to develop a voltage sensor using thermally poled silica optical fibre to measure the electric fields arising from high voltage electricity transmission lines. This has remained the central focus of this work, however through necessity and opportunity the work has extended to interferometry, signal processing and characterisation of specialty optical fibres used for sensing.

The origins of the voltage sensor project began earlier, with a 3 year collaborative project between the University of Sydney's Optical Fibre Technology Centre (OFTC), the Australian National University (ANU) and the industrial partners TransGrid and Asea Brown-Boveri (ABB). For the first two years of the project the team at ANU that included Prof Barry Luther-Davies, Dr Anna Samoc and Dr Marek Samoc, focussed on the development of a special polymer optical fibre that possessed a longitudinal electro-optic response that could be readily deployed as a voltage sensor. However this proved to be a difficult task and in the last year of the project it was decided to investigate the possibility of using thermally poled silica fibre possessing a transverse electro-optic response. At this point the project became focused on a voltage sensor configuration based on thermally poled silica fibre that was conceived earlier by Dr Ian Bassett and Mrs Margareta Bjarme of the OFTC and ABB respectively. This became the topic of a jointly owned patent and effectively instigated the work presented in this thesis.

The many improvements in the voltage sensor, that are embodied in this thesis, have arisen due to the collaborative contributions of a number of researchers; Dr. Ian Bassett, Mrs. Margareta Bjarme, Dr John Haywood, Mr John Ingram, Prof Simon Fleming, Mr. Mamdouh Matar, Mr Albert Canagasaby, Mr Phil Hambley, Mr Peter Henry and myself. I have received financial support during my PhD candidature through two generous scholarships presented to me by TransGrid and ABB. More broadly the work has been supported by various institutions; TransGrid (formerly Pacific Power), ABB Australia, ABB Sweden, the Australian research council (ARC), the Australian photonics cooperative research centre (APCRC), and the OFTC.

1.2 Structure of this thesis

(a) **Chapters**

Chapter 1 contains the introduction where the origins and motivations for this work are presented and my supervisors and collaborators are acknowledged. A brief technical background is also presented along with a summary of the publications arising out of this work.

Chapter 2 of this thesis provides the important background information which is a prerequisite for the analysis and discussion which follows.

Chapter 3 describes in detail the all-fibre interferometry used both for sensing and fibre characterisation. The signal processing methods and algorithms are also explained in detail preparing the reader for the experimental and analytical work presented in chapters 4, 6 – 10.

Chapter 4 presents an experimental study of the polarisation dependence of the linear electro-optic response in the thermally poled twin-hole fibres. A discussion regarding the magnitude of the experimentally determined polarisation dependence and the apparent disagreement with theory is included.

Chapter 5 presents a discussion about the design and optimisation of the twin-hole fibre used for the voltage sensor. A non-destructive method is presented for localising the non-linear region in the thermally poled twin-hole fibre by probing the fibre over a broad wavelength range.

Chapters 6-8 present the fibre optic voltage sensor (FOVS) systems as they have evolved through 3 generations of the signal processing system. The chapters describe and summarise the experimental methods and results. A considerable portion of the effort was in the construction, test and trouble shooting of both the optical and electronic systems. The results presented are examples of the results obtained after the systems had been optimised.

Chapter 9 presents the characterisation of temperature independent highly birefringent photonic crystal fibre (HiBi-PCF). A thorough analysis of birefringence in photonic crystal fibre and the experimental fibre characterisations are included.

Chapter 10 extends the study of HiBI-PCFs with the introduction of a spun HiBI-PCF for current sensing. Again a thorough analysis and fibre characterisation is included.

Chapter 11 is the conclusion that summarises the preceding analysis and experiments. Some plans and opportunities for further work are also highlighted.

(b) Appendices

Appendix A presents some essential elements of non-linear optics and explains how electro-optic responses arise through optical non-linearity. Some of the alternative notations used are explained.

Appendix B describes in detail the tensor nature of non-linear optics and explains the commonly used shorthand notations that are used to simplify the presentation of non-linear optical properties. The symmetry arguments used in the analysis are presented allowing the polarisation dependence of the induced electro-optic response in poled silica fibres to be studied.

Appendix C provides a background covering the necessary aspects of birefringent fibres and is intended to help understand the work presented on characterisation of HiBI-PCFs presented in chapters 9 and 10.

Appendix D is a bibliography listing all the reference material.

1.3 Technology background

The work presented in this thesis requires an understanding of three main areas of physical science and an introductory discussion of each topic is included in chapter 2 of this thesis with more detailed analysis presented in the appendices. The three main topics that need to be discussed are briefly introduced below.

1. **Non-linear polarisability in poled optical fibre.** The phenomenon known as thermal poling is used as the basis for producing the special fibre needed for voltage sensing [1, 2]. Thermal poling induces a small linear electro-optic response that essentially makes poled fibres responsive to electric fields. Electric fields can then be approximately integrated to determine the potential difference between two points and this is the basis of the voltage sensor. To understand the origins of the linear electro-optic response a discussion of non-linear polarisability in transparent media is presented in chapter 2.

2. **All fibre interferometry.** The voltage sensor system presented in this thesis is based on an all fibre, low coherence, interferometric system that is designed to exploit the small linear electro-optic response observed in thermally poled fibres and convert it into an optical phase shift. The induced, electro-optic, phase shift can then be monitored by remotely interrogating the interferometer. Designing the final embodiment of the sensing interferometer has been a trade off between various factors and to support the chosen configuration a discussion comparing classical interferometry and all fibre interferometry is presented in chapter 2.

3. **Birefringence and retardance in optical fibre.** The interferometric sensing, and fibre characterisation methods presented in this thesis depend on birefringence. The linear electro-optic response observed in poled fibres is polarisation dependent, resulting in an electro-optically induced birefringence. Light traversing a length of birefringent fibre will experience retardance between the polarisation modes. In the case of the poled fibres the retardance is then modulated by the electric field. This basic method has been extended in this thesis to include the characterisation of a recently introduced type of optical fibre known as photonic crystal fibre (PCF) [3]. Recently highly

birefringent PCFs have been produced which are particularly useful for their high birefringence and low temperature dependence [4-8].

1.4 Significance

In 1977 Alan Rogers presented a summary of the application of “Optical methods for measurement of voltage and current on power systems” [9]. In 1981 Rogers proposed intrinsic optical fibre voltage sensing [10], at around the same time optical fibre current sensing was proposed by Smith in 1978 [11]. Optical fibre current sensing has been intensively researched by many individuals and institutions; however the same cannot be said for optical fibre voltage sensing. The conventional transformers used for measuring both current and voltage are known in the industry as instrument transformers and they have served the needs of the electric power transmission industry well. Until recently there has not been a strong motivation to adopt optical fibre based technology. The emergence of new very high voltage (> 800kV) AC transmission systems and the proliferation of high voltage DC power transmission systems has placed new demands on instrument transformers. At present the technology for voltage sensing at high voltage that has been most broadly adopted by the electricity transmission industry is known as the capacitive voltage transformer (CVT). The CVT suffers from transient response problems, and resonance in the connected circuits, that have been largely addressed through careful design and selection of components and the dielectric materials [12]. At present none of the manufacturers of CVT based systems offer solutions above 800kV. A voltage sensing system based entirely on thermally poled silica offers a potential solution above 800kV, and removes the transient response and resonance issues. These factors explain the interest and involvement of ABB and TransGrid in supporting this work.

1.5 Acknowledgements

I have been very fortunate to have had exceptional levels of support from all my supervisors, collaborators, and colleagues. I have also received financial support through two generous scholarships presented to me by TransGrid and ABB to

undertake my PhD. My principal supervisor has been Dr. Ian Bassett and I cannot thank him enough for his guidance, support and encouragement. I have also been ably co-supervised by two of the most capable and creative researchers I have known, Dr John Haywood and Prof John Canning. Margareta Bjarme of ABB has also effectively acted as a co-supervisor throughout my studies and her technical and managerial input has been crucial to the progress and direction of the work. Steve Jones of TransGrid has been a long term supporter of this work and he has made significant contributions of both technical and managerial nature throughout. David Toogood and Tony Lee of ABB have also been long term supporters and contributors to the voltage sensor work.

The characterisation of the HiBi-PCFs presented in chapters 9 and 10 would not have been possible without the PCF fabrication research team at the OFTC that produced the fibres. The team was lead by Prof John Canning and Dr Katja Digweed and included Dr Mattias Åslund, Mr Brian Ashton, Mr Michael Stevenson, Mr Peter Henry and Mr Justin Digweed.

I would also like to acknowledge the support of the Australian Photonics Cooperative Research Centre, and the Australian Research Council in providing facilities.

The work which is described in this thesis can be split into three categories: that which can be wholly attributed to others, that which is the joint product of myself (the author) and others, and that which can be wholly attributed to the author.

(a) Work wholly attributed to others

- The conception of the optical fibre voltage sensor based on coiled, thermally poled, silica fibre can be attributed to Dr. Ian Bassett (University of Sydney-USYD) and Margareta Bjarme (Asea Brown-Boveri – ABB) and predates the author’s involvement in the project. This invention is protected by a patent jointly owned by the USYD and ABB.
- The initial conception, construction and design of the signal processing scheme is attributable to Dr John Haywood (USYD).

(b) **Work of the author and others**

- The conception of the low coherence interferometric sensing system was the joint effort of Dr John Haywood and the author.
- The design and development of the signal processing algorithms to process the output from the voltage sensor system was the joint effort of Dr John Haywood and the author.
- The design, construction and testing of the high speed optical spectrum analyser and the attached signal processing electronics and algorithms were the joint effort of Dr John Haywood, Mr John Ingram, and the author.
- The improvements in the fabrication methods for the twin-hole fibre were the joint effort of Mr Peter Henry and the author.
- The analysis and modelling of both the twin-hole fibre and the highly birefringent photonic crystal fibre were the joint effort of Dr Nader Issa, Dr Alex Argyros and the author.

(c) **Work wholly attributable to the author**

The remainder of the work presented here is the sole work of the author. This includes

- The design and implementation of the all fibre Mach Zehnder Interferometer (MZI) for in situ poling and characterisation with polarisation control.
- The design and implementation of the reflection configuration low coherence interferometric sensing system. Earlier designs of the interferometer were focussed on balancing the optical path lengths and effectively making the interferometer largely wavelength insensitive. The author proposed a design with a small and deliberate path imbalance that results in strong and repeatable wavelength dependence. The signal processing system then monitors this.
- The design and implementation of the multiple wavelength all fibre MZI.
- The characterisation scheme for both the HIBI PCFs and the spun PCFs.

1.6 Contributing publications

First author publications

1. Conference paper “Polarisation dependence of the linear electro-optic coefficient in thermally poled twin-hole silica fibre” A.Michie, I.Bassett, and J.Haywood. EWOFS 04, Santander, Spain June 2004.

2. Journal paper “Temperature independent highly birefringent photonic crystal fibre”, A.Michie, J.Canning, K.Lyytikainen, M.Aslund, and J.Digweed. Optics Express 12, 21 (2004) 5160-5165.

3. Conference paper “Athermal birefringence in a photonic crystal fibre” A.Michie, J.Canning, K.Lyytikainen, M.Aslund, and J.Digweed, AIP congress 2005, Canberra Australia.

4. Conference paper “A low coherence interferometric sensing method with analysis and experimental results for voltage sensing”, A.Michie, I.Bassett, and J.Haywood, OFS-17 2005

5. Conference paper “Temperature independent polarization maintaining fibre for sensing and interferometry”, A.Michie, J.Canning, K.Lyytikainen, M.Aslund, and J.Digweed, OFS-17 2005

6. Conference paper “Voltage sensing using thermally poled silica fibre”, A.Michie, I.Bassett, and J.Haywood, BGPP 2005

7. Conference paper “Characterisation of thermally poled twin hole silica fibre over a broad wavelength range”, A.Michie, K Digweed, J Ingram, I.Bassett, and J.Haywood ACOLS 2005

8. Journal paper “Electric field and voltage sensing using thermally poled silica fibre with a simple low coherence interferometer”, A.Michie, I.Bassett, and J.Haywood, Meas. Sci. Technol. 17 (2006) 1229-1233

9. Conference paper “Sensing electric fields using thermally poled silica at 50 Hz”, A.Michie, I.Bassett, and J.Haywood, OFS-18 2006

10. Conference paper “Spun Highly Birefringent Photonic Crystal Fibre for Current Sensing”, A.Michie, J.Digweed, J.Canning, B.Ashton, M.Stevenson, J.Digweed, I.Bassett, and J.Haywood, OFS-18 2006

11. Journal paper "Spun elliptically birefringent photonic crystal fibre", A.Michie, J.Canning, I.Bassett, J.Haywood, K.Digweed, M Aslund, B.Ashton, M.Stevenson, J.Digweed, A.Lau, and D.Scandurra", Optics Express 15, 4 (2007) 1811-1816.

12. Journal paper "Spun elliptically birefringent photonic crystal fibre for current sensing", A.Michie, J.Canning, I.Bassett, J.Haywood, K.Digweed, M Aslund, B.Ashton, M.Stevenson, J.Digweed, A.Lau, and D.Scandurra, Meas. Sci. Technol. 18 (2007) 3070-3074

13. Journal paper "Electric field and voltage sensing at 50Hz using a thermally poled silica fibre", A.Michie, I.Bassett, J.Haywood, and J.Ingram, Meas. Sci. Technol. 18 (2007) 3219-3222

14. Conference paper "Lab trials of an electricity transmission line voltage sensor based on thermally poled silica fibre", A.Michie, P.Hambley, I.Bassett, J.Haywood, P.Henry, and J.Ingram, BGPP 2007

15. Conference paper "Lab trials of an electricity transmission line voltage sensor based on thermally poled silica fibre", A.Michie, J.Ingram, I.M.Bassett, J.H.Haywood, P.Hambley, and P.Henry, OFS 19

Co-authored publications

1. Conference paper "Spun highly birefringent (Shi-Bi) photonic crystal fibre" K.Digweed, A.Michie, J.Canning, B.Ashton, M.Stevenson, J.Digweed, I.Bassett, and J.Haywood ACOLS 2006

2. Conference paper, " PCF HI-BI 2-sections Fibre Lyot Depolarisers" M. Matar, A. Michie, I. Bassett, J. Canning, J. Haywood, K. Digweed, , ACOFT 2006.

3. Conference paper, "2-Section PCF Hi-Bi Lyot Depolarisers", M. Matar, A. Michie, I. Bassett, J. Canning, J. Haywood, K. Digweed, , OFS 2006.

4. Conference paper , "Self aligning fibre for a fibre optic voltage sensor", P. Hambley, A. Michie, I. Bassett, P. Henry, J. Ingram, OFS 19

Chapter 2. Background

This is an introduction to the science required to understand the experiments, results and analysis presented in the subsequent chapters. Some of the important details are presented in the appendices to this thesis.

2.1 Non-linear polarisability

(a) **Linear polarisability in dielectrics**

When light or any electro-magnetic wave is incident on a dielectric material the charged particles within the dielectric oscillate and behave as forced oscillators. The movement of charged particles at the incident wave's frequency essentially creates dipoles within the dielectric and the material and can be considered as being polarised by the incident wave. Often a concept of charged particles constrained on springs is used to illustrate this response. The polarisability of the material P due to an incident electric field E can be represented schematically by the scalar equation

$$P = \varepsilon_0 \chi E \tag{2.1}$$

where ε_0 is the permittivity of free space and χ is known as the susceptibility of the material. The term χ describes the material's response to the incident electric field and χ is typically a function of the intensity, frequency and polarisation of the incident electric field. Familiar concepts in optics such as refractive index and absorption can be described in terms of the susceptibility χ [13] and the tensor character of the relationship between $P, E\ and\ \chi$ is introduced in section 2.2.

(b) **Non-linear polarisability in dielectrics**

The interaction of light with matter in ordinary circumstances is considered largely independent of the illumination intensity. However using the concept that the oscillating charges respond as though constrained by springs it can be seen that at some point the electric field may become so intense that the induced polarisation is in some way distorted and the springs are extended beyond their capacity to respond linearly. In practice this limit was not observed until the invention of the laser and non-linear optical phenomena were observed by Franken et al in 1961 [14]. This distortion of the polarisability in the presence of large incident fields can be treated by allowing the term χ in equation (2.1) to be a function of the incident field E. The scalar equation (2.1) can be rewritten as a power series in E as follows

$$P = \varepsilon_0\left(\chi^{(1)}E + \chi^{(2)}E^2 + \chi^{(3)}E^3 + \cdots\right) \tag{2.2}$$

Here $\chi^{(1)}$ represents the linear susceptibility described above and $\chi^{(2)}$, $\chi^{(3)}$ are known as the non-linear susceptibilities.

(c) Quadratic non-linearity

The lowest order non-linear term describes the response of the dielectric to the square of the incident electric field. This is often referred to as the second order non-linearity and the second order polarisability $P^{(2)} = \varepsilon_0\left(\chi^{(2)}E^2\right)$ gives rise to many interesting non-linear effects resulting through mixing of incident waves and inducing polarisation at sum and difference frequencies. A particularly useful example is the process known as parametric amplification where the generation of difference frequency polarisation is used to amplify a weak signal at frequency ω_s. This is achieved by introducing a high intensity pump at a higher frequency ω_p and due to the quadratic polarisation of the non-linear medium, energy is transferred to an idler wave at the difference frequency, $\omega_I = \omega_P - \omega_S$. The idler and the pump then interact, through essentially the same process, to amplify the original signal at the difference frequency i.e. $\omega_S = \omega_P - \omega_I$.

Frequency doubling is a special case of sum frequency generation where two effectively indistinguishable incident waves, at the same frequency ω, are mixed and due to the quadratic nonlinearity of the material polarisation occurs at the sum frequency 2ω.

These processes can be made effective, even if the quadratic non-linearity is relatively small, if the process can be distributed along the length of the dielectric medium and the condition known as phase matching is to some extent satisfied. For efficient parametric amplification phase matching requires that $k_I + k_s = k_P$ where $k_I, k_s\ and\ k_p$ are the wavenumbers corresponding to $\omega_I,\ \omega_s\ and\ \omega_p$ respectively [13, 15].

Sum frequency generation can also be achieved when mixing an incident wave $E_{(\omega)}$ at frequency ω with a DC electric field $E_{(DC)}$. In this case a component of the polarisation is induced at a product of the electric field strength $E_{(\omega)}$ and the DC electric field strength $E_{(DC)}$. This gives rise to the linear electro-optic response, or Pockels effect where the refractive index is linearly proportional to the applied DC electric field. Unlike parametric amplification and frequency doubling, the Pockels effect is observable at relatively low intensity and without the added constraint of phase matching. The Pockels effect was discovered in 1893 and second harmonic generation was first observed in silica optical fibre by Ohmori and Sasaki in 1982 [16]. Special optical fibres, prepared using a process known as poling, exhibit the Pockels effect and form the basis of the sensing fibre used in the voltage sensor presented in this thesis.

(d) **Cubic non-linearity**

Many materials are forbidden, due to symmetry constraints (see appendices A and B), from having even order non-linearities and often the third order non-linear polarisability $P^{(3)} = \varepsilon_0\left(\chi^{(3)}E^3\right)$, is the lowest order non-linear term. Again many interesting non-linear phenomena arise out of the third order non-linearity. Third harmonic generation can be achieved where an incident wave at frequency ω induces a polarisation at frequency 3ω due to the cubic non-linearity. Again for this process to be efficient, high intensity and third order non-linearity is required along with suitable phase matching.

The mixing of an incident wave at frequency ω with a DC electric field will result in a polarisation proportional to the product of the electric field strength $E_{(\omega)}$ and the square of the DC electric field strength ${E_{(DC)}}^2$. This is known as the Kerr effect or the quadratic electro-optic effect.

2.2 The susceptibility tensor

The convenient scalar form of the polarisability presented in equation 2.2 can be used to explain many of the interesting non-linear phenomena of interest. However it is somewhat schematic, as it ignores the tensor character of P, E and χ. The correct tensor version of equation 2.2 is

$$P_i = \varepsilon_0\left(\chi_{ij}{}^{(1)}E_j + \chi_{ijk}{}^{(2)}E_jE_k + \chi_{ijkl}{}^{(3)}E_jE_kE_{l+\cdots}\right), \tag{2.3}$$

where the summation notation over repeated indices is implied. The tensor version can be used when and if it is needed to describe particular non-linear phenomena.

Both the linear and non-linear susceptibilities are represented by tensors with rank n+1 where n is the order of the susceptibility. The linear susceptibility tensor $\chi_{ij}{}^{(1)}$ relates two vectors and is thus a tensor of rank 2 and can be represented by a 3X3 matrix with nine elements. The second order susceptibility tensor is a rank 3 tensor and has 27 elements. The third order susceptibility tensor is rank 4 and has 81 elements. These non-linear susceptibility tensors of rank 3 and above can no longer be represented by simple 2 dimensional matrices and although in many cases they can be greatly simplified the presentation and analysis becomes more complex.

2.3 The tensor elements and permutation symmetry

When using the susceptibility tensor to describe the transparent medium that is being studied a choice of co-ordinate system needs to be made. The electric field E can then be described in terms of components E_1, E_2 and E_3, and the linear susceptibility elements can be described by the a 3 X 3 matrix containing 9 elements of the form

$$\chi_{ij} = \begin{vmatrix} \chi_{11} & \chi_{12} & \chi_{13} \\ \chi_{21} & \chi_{22} & \chi_{23} \\ \chi_{31} & \chi_{32} & \chi_{33} \end{vmatrix} \tag{2.4}$$

The material polarisation P in the i direction is found by forming the appropriate scalar products $\chi_{ij}E_j$ and summing all the contributions for the i axis.

As mentioned above higher order susceptibility tensors are more complicated and the simple matrix representation is no longer possible. The second order susceptibility tensor is rank 3 and contains 3 x 3 x 3 = 27 elements of the form χ_{ijk} such as χ_{111} .

Similarly the second order contribution to the polarisation P is found by forming the appropriate scalar products $\chi_{ijk}\, E_i E_j$ and summing all the contributions for each axis.

The permutation symmetry property of the second order susceptibility tensor $\chi_{ijk}{}^{(2)}$ simply means that the susceptibility elements are independent of the order of the subscripts j, k e.g. $\chi_{ijk} = \chi_{ikj}$. Similarly, for the third order susceptibility tensor $\chi_{ijkl}{}^{(3)}$ the elements χ_{ijkl} are independent of the order of the subscripts $j, k, and\ l$ e.g. $\chi_{ijkl} = \chi_{ijlk} = \chi_{ilkj\ \ldots\ldots}$. This can be shown to be true regardless of material spatial symmetry properties and a detailed discussion can be found in appendix B (see appendix B.2) [13, 15].

The ensuing discussion uses both the shorthand scalar prescriptions and the full tensor prescriptions.

2.4 Electro-optics in non-linear dielectrics

The interaction of DC electric fields and optical frequency electric fields in a non-linear dielectric gives rise to a number of useful non-linear processes and an informative illustration of how these effects can come about is presented below. By simply considering the incident electric field as being comprised of a DC electric field at frequency $\omega = 0$ and an oscillating electric field an optical frequency ω i.e.

$$E_{(t)} = E_{(0)} + E_{(\omega)} \tag{2.5}$$

and substituting into equation 2.2 and expanding we obtain an expression for the induced polarisation $P = \varepsilon_0 \left(\chi^{(1)} E_{(t)} + \chi^{(2)} E_{(t)}{}^2 + \chi^{(3)} E_{(t)}{}^3 \ldots\right)$ i.e.

$$\begin{aligned} P = {} & \overbrace{\varepsilon_0 \left(\chi^{(1)} E_{(0)} + \chi^{(1)} E_{(\omega)}\right)}^{1} + \overbrace{\varepsilon_0 \left(\chi^{(2)} E_{(0)}{}^2\right)}^{2} + \overbrace{2\varepsilon_0 \left(\chi^{(2)} E_{(0)} E_{(\omega)}\right)}^{3} + \\ & \overbrace{\varepsilon_0 \left(\chi^{(2)} E_{(\omega)}{}^2\right)}^{4} + \overbrace{\varepsilon_0 \left(\chi^{(3)} E_{(0)}{}^3\right)}^{5} + \overbrace{3\varepsilon_0 \left(\chi^{(3)} E_{(0)}{}^2 E_{(\omega)}\right)}^{6} + \\ & \overbrace{3\varepsilon_0 \left(\chi^{(3)} E_{(0)} E_{(\omega)}{}^2\right)}^{7} + \overbrace{\varepsilon_0 \left(\chi^{(3)} E_{(\omega)}{}^3\right)}^{8} \ldots \end{aligned} \tag{2.6}$$

Term 1 in equation (2.6) represents the linear component of the induced polarisation.

Term 2 is simply the second order non-linear response to the incident DC electric field.
Term 3 represents an induced polarisation at the optical frequency that is directly proportional to the incident electric field. This gives rise to the electro-optic Pockels effect or linear electro-optic response that is explained in more detail in appendix A.

Term 4 is the second order non-linear response to the incident optical field and this gives rise to useful effects such as second harmonic generation and optical rectification.

Term 5 is simply the third order non-linear response to the incident DC electric field.

Term 6 represents an induced polarisation at the optical frequency that is directly proportional to the square of the incident electric field. This gives rise to the Kerr effect or quadratic electro-optic response that is explained in more detail in appendix A.

Term 7 represents an induced polarisation proportional to the square of the incident optical field and acting on the third order non-linearity of the dielectric. This acts effectively as a second order non-linear process and has been used to demonstrate second order non-linear processes such as a linear electro-optic response, and frequency doubling in centro-symmetric dielectrics that would otherwise have zero second order non-linearity [13].

Term 8 is the third order non-linear response to the incident optical field and this gives rise to useful effects such as third harmonic generation.

2.5 Thermal poling of twin-hole optical fibre

Amorphous glass that makes up the core and cladding of twin hole optical fibre is forbidden from having any second order non-linearity due to its material symmetry (see appendices A and B). The process of thermal poling induces a small second order nonlinearity that results in a small linear electro-optic response.

Thermal poling of optical fibre involves heating the fibre to around 300 degrees Celsius while DC electric fields of around 2 x 10^8 V/m are applied transversely across the core. Special optical fibres have been designed that incorporate two large longitudinal holes running the length of the fibre (See figure 2-1). Conducting electrodes can be inserted into these holes and electric fields can be applied transversely across the core region. After poling, these fibres retain a small electro-optic response, where the application of a DC electric field across the core, will result in a linear change in the fibre's refractive index [2]. Poled fibres used in this work typically have linear electro-optic or Pockels coefficients (LEO) of 0.2pm/V after thermal poling.

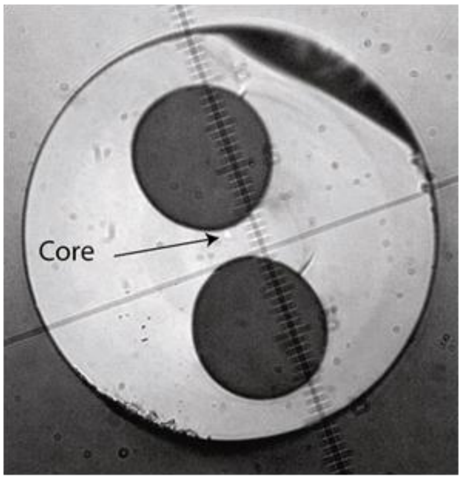

2-1 A typical twin-hole fibre cross section

2.6 Linear electro-optic response and polarisation dependence

The linear electro-optic response of the thermally poled fibres studied in this thesis has a small dependence on the input polarisation. A widely accepted model for the poling mechanism suggests that charge separation due to the migration of mobile ions produces large internal electric fields within the fibre after thermal poling [17, 18]. This internal electric field acts on the $\chi^{(3)}$ of the fibre to induce an effective $\chi^{(2)}$ using the same process described in section 2.4 above [18]. Symmetry arguments suggest that this process should result in a polarisation dependence that has a ratio of 3:1 between light polarised in the same direction as the poling field and light polarised in the orthogonal direction [19]. These symmetry arguments are presented in detail in appendix B using the tensor form of the non-linear susceptibility.

Exploiting this small polarisation dependence observed in thermally poled twin-hole fibre is used as the basis of the voltage sensor experiments presented in the subsequent chapters [20, 21].

2.7 Interferometric optical fibre sensing

Classical interferometer configurations such as the Michelson and Mach-Zehnder can be configured as all fibre interferometers by using commercially available optical couplers as beam splitters and re-combiners. The separate optical paths can be contained entirely within optical fibre. This provides significant advantages such as ease of coupling by fusion splicing and the ability to interrogate a sensing interferometer system remotely by delivering the light from a light source via an optical fibre. All fibre interferometry also introduces new challenges such as polarisation control and other environmental effects in the fibre arising through temperature and strain variations. These challenges can be largely addressed through the use of special optical fibres and careful interferometer design and it is in this area that often the greatest improvements in signal to noise performance can be attained [22].

Optical fibre sensing systems based on two-beam interferometric measurements rely on the measurand modulating the optical path length of one or both of the two separate optical paths. The sensing interferometer can be designed so that the measurand either modulates the effective refractive index of the sensing fibre, for example through the electro-optic or stress optic effect, and/or affects the physical path length by stretching or displacement. The resulting change in optical path length difference for the two optical paths produces a wavelength dependent intensity variation at the output ports of the interferometer. The interferometer can then be interrogated either with a narrow long coherence light source such as a laser, or in the case where the optical path length difference is small the interferometer can be interrogated with a broadband low coherence light source such as an amplified spontaneous emission source like a light emitting diode (LED). This is often known as low coherence interferometry and requires careful interferometer design since path length differences greater than the coherence length of the light source will result in loss of contrast of the fringes at the output ports (fringe fading).

Optical fibre sensors often benefit from reduced sensitivity demands compared with telecommunications devices such as electro-optic switches. The signal processing system can be designed to detect very small signals with noise floors as low as micro radians per root hertz [23]. Silica based optical fibre has been the preferred medium for optical fibre based telecommunications since it is a tremendously transparent (low loss) material that benefits from very low non-linearity. This apparently ideal medium is however not completely immune to external perturbations and although the response is small, silica optical fibres are sensitive to many things including electromagnetic interference through the electro-optic and magneto-optic effects (otherwise known as the Pockels, Kerr and Faraday effects). The challenge in designing optical fibre sensing interferometers is in making it sensitive only to the intended measurand and rejecting sources of ghost signals.

2.8 Common mode rejection

An essential part of any interferometer design is common mode rejection. If an interferometer is designed such that any perturbation that you don't want to measure creates an equal response for both optical paths then the net path length difference for the interferometer will be zero and this "common mode" effect is rejected. Special optical fibres and interferometers have been designed to maximise this effect and three special cases are listed below.

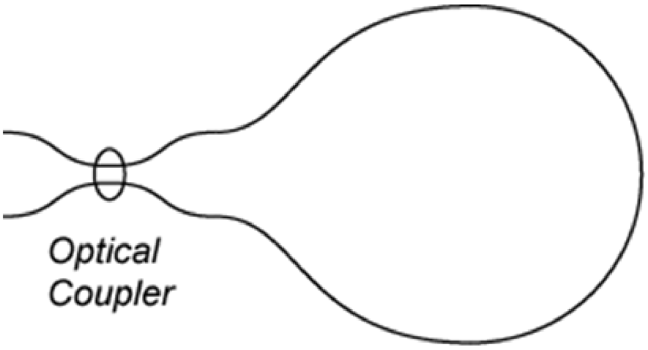

2-2 Basic Sagnac interferometer

(a) **Sagnac interferometer**

The Sagnac interferometer is configured such that the two separate optical paths traverse a single section of optical fibre but in opposite directions. In this case slowly varying environmental perturbations affect light travelling in opposite directions equally and common mode rejection is largely achieved. However non reciprocal effects such as gyroscopic rotation and the Faraday Effect produce a non reciprocal phase shift and this can be observed at the output ports of the interferometer.

(b) Twin core fibre

It is not always possible to implement a Sagnac configuration and if the measurand does not produce a non reciprocal effect then it becomes more difficult to optimize for common mode rejection. A compromise can be made by configuring the two optical paths to traverse through as near as possible the same physical space. One simple way to achieve this is to place the two fibres adjacently so that both fibres experience the same perturbations. While this method can prove to be effective, it has limited success especially in case of high temperature gradients.

A more effective solution is to use specialty fibre that has two optical cores. This effectively places the two optical paths even closer together and further improves common mode rejection. Twin core fibre presents other challenges such as difficulty in coupling separately into the two optical cores, difficulty in manufacturing the more complex structure and ultimately the fibre needs to have some differential response for the two separate cores to the measurand.

(c) Two polarisation mode interferometer (TPI)

When discussing polarisation effects in optical fibres it is often pointed out that the term single mode fibre is a little misleading. A so called single mode fibre that supports a single transverse mode will in most cases support two orthogonal polarisation modes. In the case of linearly birefringent fibre these two modes can be defined as x and y polarised modes where the Cartesian coordinate system is implied. The z axis is defined as the local fibre axis and x and y axes are the two local orthogonal transverse axes of the optical fibre. There are a few alternative terminologies used to describe polarisation modes and birefringent fibres in general and a more detailed explanation can be found in appendix C.

Relative to twin-core fibre a further improvement in common mode rejection can be made by dividing the two separate optical paths into the two polarisation modes. In this case the two optical paths traverse essentially the same physical space and common mode rejection is optimized. The challenge here is now that the interferometer is only sensitive to effects that produce a polarisation dependent response in the optical path length of the sensing fibre. This often results in a trade off between sensitivity and common mode rejection and requires that the polarisation dependence of the desired response is adequate. This method is the basis of the majority of the experimental work presented in this thesis and a more detailed discussion can be found in chapter 3.

2.9 Voltage Sensing

(a) **Introduction**

Measuring the electric fields arising from high voltage electricity transmission lines using optical fibres requires a linear electro-optic response. Early proposed designs based on the optical Kerr effect utilized a quadratic response where only the magnitude of the electric field could be determined (see figure 2-3) [10, 24, 25].

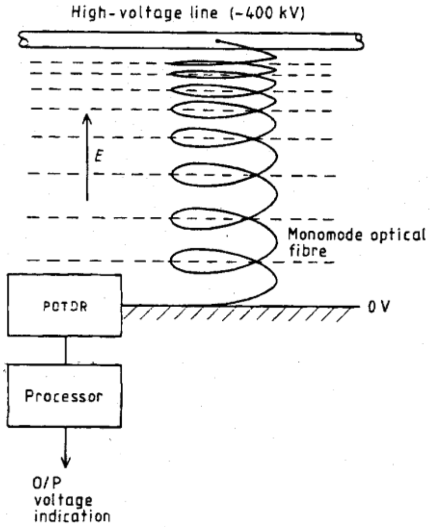

2-3 Alan Rogers' proposed all fibre voltage sensor configuration [25]

In his review article entitled “Distributed optical-fibre sensors” Rogers described the longitudinal linear electro-optic effect in amorphous silica as being ‘emphatically absent” [25]. Poled silica fibres however have a small residual transverse linear electro-optic response (LEO), typically 0.20pm/V that essentially forms the basis of an intrinsic optical fibre sensor for electric fields. To calculate the transmission line voltage we need to evaluate the tangential line integral of the electric field along some path between the two points A and B where the points A and B are at the high voltage transmission line, and the ground potentials respectively. i.e.

$$V = V_A - V_B = \int_A^B E.dl \tag{2.7}$$

Arranging the poled silica fibre in a helix produces a good approximation to equation (2.7). When averaged over a period of the helix, the response is approximately only to the component of the electric field along the axis of the helix (see figure 2-4). This approximation is better the more uniform the electric field. The helix may be regarded as inscribed on a uniform cylinder, and the sensitivity is highest if the local poling direction is parallel to the corresponding tangent plane of the helix. The fields to be measured in practice are of course non-uniform, and this method is valid only to the extent that a spatial average may be taken over a volume of radius r and depth p, where r is the radius of the helix and p the pitch. In other words, this method assumes that the field is sufficiently uniform in such a volume.

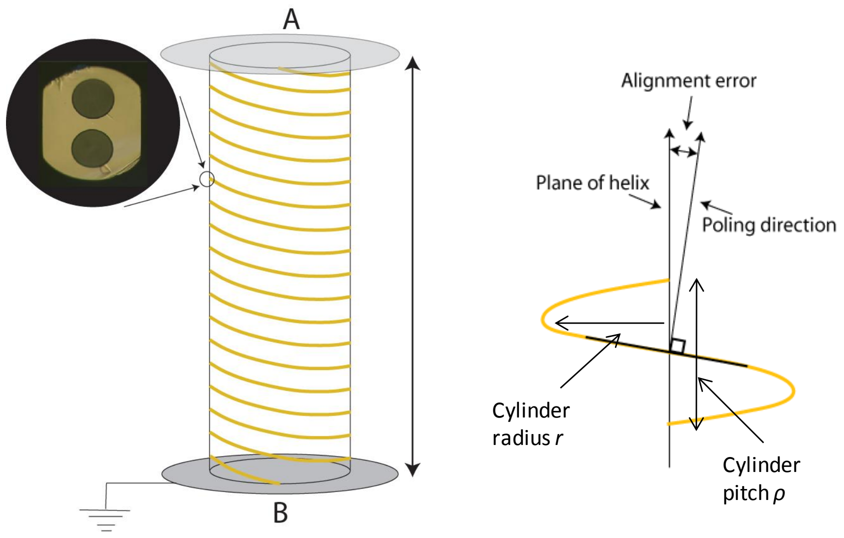

2-4 Coiled poled fibre illustration

Since the linear electro-optic response of the poled fibre is to transverse and not longitudinal electric fields the induced electro-optic response in the coiled fibre will be proportional to the integral $V = V_A - V_B = \int_A^B E.dl$ and a sensitivity constant will have to be experimentally determined. The voltage sensors presented in this thesis were all configured using the two polarisation interferometer as discussed in section 2.8c above. In this case the interferometer only responds if there is a differential linear electro-optic response (DLEO) for the two polarisation modes. Typically the ratio of the LEO for the two polarisation modes observed in the poled fibres presented in this thesis has been approximately 1.17:1 resulting in a DLEO of about 0.03pm/V.

2.10 Birefringence in optical fibres

A single mode optical fibre that has a difference in the effective refractive indices for the two polarisation modes is described as a birefringent fibre. The modal (or phase) birefringence is defined as [26, 27]

$$B_m = \left|n_x - n_y\right| \tag{2.8}$$

where n_x and n_y are the effective refractive indices (phase indices) for each polarisation mode. Modal birefringence produces retardance between polarisation modes when light traverses a length of fibre. Fibres with high birefringence (HiBi) act very effectively as polarisation maintaining (PM) fibres. Cross coupling, or transfer of energy between polarisation modes, is greatly reduced due to the large difference in phase indices. This results in very poor phase matching for any energy transfer process and often the birefringence is presented in the form of a beat length that corresponds to the physical length of fibre over which a 2π phase shift is accumulated between the two polarisation modes. The beatlength is given by

$$L_b = {}^{\lambda_0}/_{B_m}, \tag{2.9}$$

where λ_0 is the free space wavelength.

In applications such as telecommunications the group birefringence also needs to be considered. The group birefringence describes how a pulse disperses as it traverses along a birefringent fibre if the energy of the pulse is divided into the two polarisation modes. In the telecommunications industry this phenomenon is known as polarisation mode dispersion (PMD) and it is a significant problem at high data rates transmitted over long distances particularly if chromatic dispersion compensation has been implemented. The group birefringence is given by

$$B_g = \left(B_m(\lambda) - \frac{\lambda d B_m(\lambda)}{d\lambda}\right) \tag{2.10}$$

(see appendix C for details).

It can be seen that if the modal birefringence is independent of wavelength then the derivative term vanishes and the group and phase birefringence are equal. The birefringence found in conventional HiBi optical fibres can be attributed to either form or stress birefringence. Form birefringence is usually introduced by having an elliptical shaped core and/or cladding region. Stress birefringence arises through the stress-optic effect. By placing regions with different thermal expansion coefficients from the host material on either side of the core, differential stress for the x and y polarisation modes is introduced. The most commonly used stress birefringence fibres are bow-tie and Panda fibre. Example cross sections are shown in figure 2-5. Recently highly birefringent photonic crystal fibres (HiBi-PCFs) have emerged that possess significant form birefringence [8]. HiBi-PCFs provide not only higher birefringence than has been achievable with the conventional stress and form birefringent fibres discussed above but in addition they posses intrinsically low temperature dependence due to their single material construction [4, 7]. The interferometric sensing system developed for the voltage sensor has been adapted to characterise the temperature dependence of HiBi-PCFs and the results are presented in this thesis.

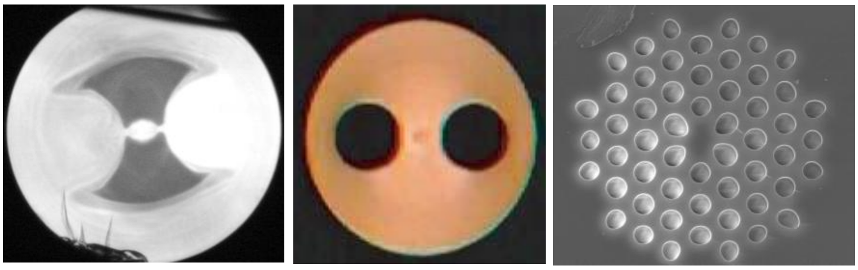

2-5 Cross sections of bow-tie, Panda, and HiBi-PCF from left to right

Chapter 3. The low coherence interferometer and signal processing system

3.1 *The Mach-Zehnder two polarisation interferometer (MZ-TPI)*

The common thread that links together all the work presented in this thesis is the low coherence interferometer and the signal processing method. The low coherence interferometer is based on the two polarisation interferometer (TPI) that was introduced in section 2.8c above and a more detailed description and analysis is presented below.

Polarised light can be launched equally into the two polarisation modes of a length of birefringent (sensing) fibre simply by aligning the input plane of polarisation at 45 degrees to the fibre's polarisation axes. As the light propagates along the birefringent fibre the two modes will accumulate a phase difference, or relative retardance. Light at the output end of the fibre can then be analysed with a polariser orientated at 45 degrees to the polarisation axes. The output polarisation will depend on the relative phase of light in the two polarisation modes at the output. An illustration of this configuration is presented in figure 3-1 below. It can be seen that at the input, light is effectively split into two separate optical paths. The two polarisation modes then propagate along the birefringent fibre and at the output end the optical paths are recombined in the polariser. If the relative retardance depends on a measurand, this TPI configuration is equivalent to a Mach-Zehnder Interferometer (MZI). For a uniform length of birefringent fibre the optical path lengths for each arm of the interferometer are $OPL_x = n_x L$, and $OPL_y = n_y L$ where n_x, and n_y are the effective refractive indices for the x, and y polarised modes respectively. The optical path length difference, or retardance, seen at the output is

$$\Delta OPL = \left(OPL_x - OPL_y\right) = \left(n_x L - n_y L\right) = \Delta n L = B_m L \qquad (3.1)$$

where B_m is the modal birefringence defined in section 2.10 above

The optical phase shift due the path imbalance is

$$\Delta\phi = {}^{2\pi\Delta OPL}/_{\lambda_0} = {}^{2\pi\Delta nL}/_{\lambda_0} \tag{3.2}$$

where λ_0 is the average free space wavelength.

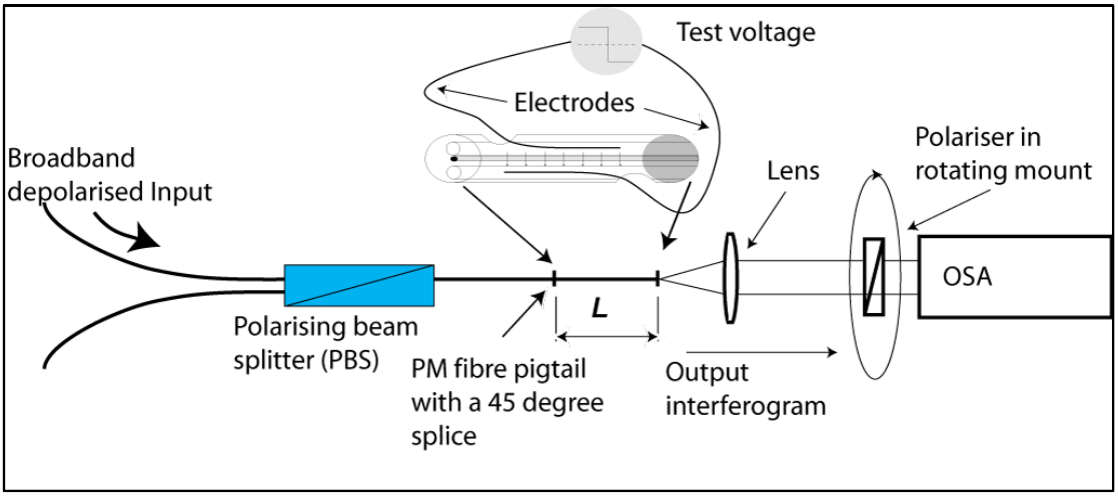

3-1 The Mach-Zehnder two polarisation interferometer (MZ-TPI)

By illuminating the interferometer with a broadband depolarised light source and recording the optical spectrum at the output, the input spectrum will emerge with a spectral modulation imposed by the interferometer (see figure 3-2 below). If the interferometer is carefully designed and constructed the spectral modulation can be clearly resolved using an optical spectrum analyser. If the length of birefringent fibre is then exposed to a perturbation that alters the birefringence then this will result in a change in the path imbalance and appear as a change in the phase and period of the spectral modulation.

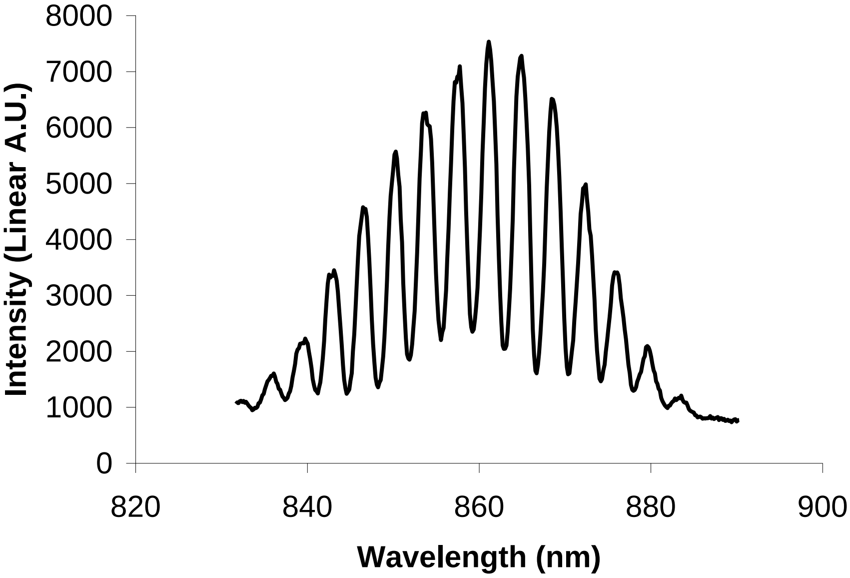

3-2 MZ-TPI output spectrum or interferogram

3.2 *The Michelson two polarisation interferometer (M-TPI)*

A Michelson two polarisation interferometer (M-TPI) can be constructed by launching light into the fibre through a polarising beam splitter (PBS) and reflecting the light back down the fibre at the far end. The orthogonal input polarisation port of the PBS can then be used as the output port of the interferometer and in this case the optical phase shift at the output is

$$\Delta\phi = {}^{4\pi\Delta nL}/_{\lambda_0}, \tag{3.3}$$

i.e. twice the phase shift seen in the MZ-TPI configuration. Most of the experiments presented in this thesis used an all fibre M-TPI constructed using a commercially available, 3 port polarisation beam splitter (PBS) with polarisation maintaining (PM) fibre pigtails as the polarisation splitter/combiner. Broadband depolarised light launched into an input arm of the PBS emerged at the output with light only in one polarisation mode of the output fibre pigtail. The output pigtail was then spliced to the sensing fibre with the polarisation axes orientated at 45 degrees. The light would then propagate along the sensing fibre and be reflected back along the fibre at the end by a mirror. When the light in the fibre arrives back at the 45 degree splice the two polarisation modes are recombined and the interferometer is closed. The PM fibre pigtail acts like an extension of the polarising beam splitter and effectively places the polariser at the 45 degree splice.

The illustration below shows a schematic configuration.

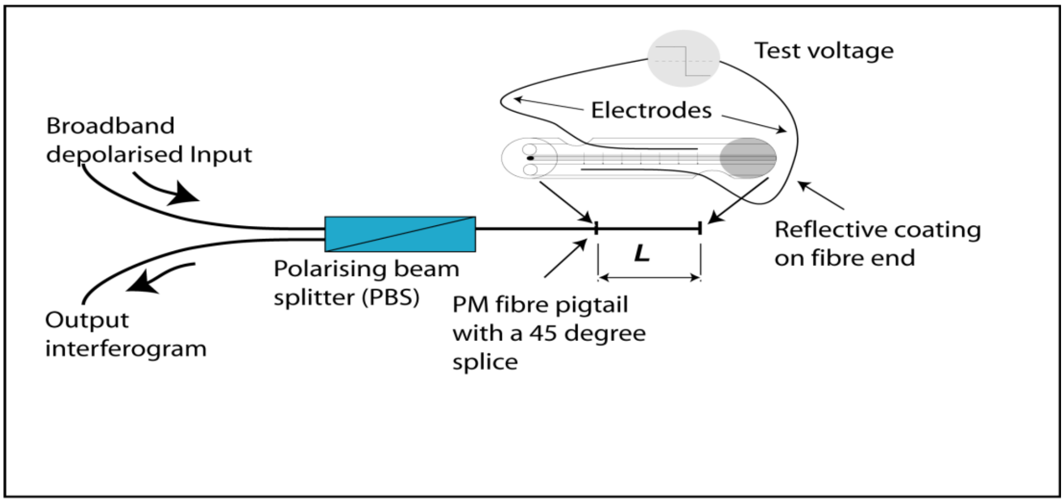

3-3 M-TPI configured using thermally poled twin-hole fibre

The greatest advantage of the all fibre M-TPI is that both the broadband depolarised input and the output spectrum can be delivered and retrieved remotely using standard low birefringence telecommunications fibre (SMF-28). For some experiments loss in the 45 degree splice was excessive and the experiments were reconfigured in transmission as a MZ-TPI.

3.3 The M-TPI for voltage sensing

Thermally poled silica can be used as the sensing fibre in the M-TPI to sense electric fields. The thermally poled silica fibre can be arranged helically as described in section 2.9(a) to approximate the integral of the electric field and measure the voltage. It has been demonstrated that the thermally poled twin-hole fibre has a linear electro-optic coefficient (LEO) that is different for the two polarisation modes and the difference can be referred to as the differential linear electro-optic coefficient (DLEO) (see chapter 4). The optical phase shift is given by

$$\Delta\phi = {}^{4\pi\Delta n(E)L}/_{\lambda_0} \tag{3.4}$$

where the birefringence of the thermally poled silica fibre $\Delta n(E)$ is a function of the electric field E. In practice the sensing section was made up of highly birefringent (HiBi) pigtailing fibre and thermally poled silica optical fibre, and as a result the birefringence is not uniform along the length of the sensing section. The optical path length difference for light in the two polarisation modes can be found by integrating the local birefringence along the length of the fibre .i.e.

$$\Delta OPL = 2\int n_x(\lambda)\,dl - \int n_y(\lambda)\,dl = 2\int \Delta n(\lambda)\,dl \tag{3.5}$$

where $n_x(\lambda)$ and $n_y(\lambda)$ are the local refractive indices of the x and y modes respectively and $\Delta n(\lambda)$ is the difference. The factor of two arises due to the reflect-back configuration of the interferometer.

The corresponding total phase shift is

$$\Delta\phi(\lambda) = \frac{4\pi}{\lambda}\int \Delta n(\lambda)\,dl \tag{3.6}$$

Since the term $\Delta n(\lambda)$ in equation (3.6) is made up of the sensing section's response to the applied voltage and other sources of birefringence, such as the HiBi fibre pigtails, then $\Delta n(\lambda)$ can be expressed as

$$\Delta n(\lambda) = kV_{ac} + \Delta n'(\lambda) \tag{3.7}$$

where k is a sensitivity constant that needs to be determined experimentally, $+\Delta n'(\lambda)$ represents all the other sources of birefringence, and V_{ac} is the applied voltage to be measured (typically at 50 or 60 Hz).

Substituting (3.7) into (3.6) the total phase difference at the centre wavelength λ becomes

$$\Delta\phi(\lambda) = \frac{4\pi}{\lambda}\int \left(kV_{ac} + \Delta n'(\lambda)\right) dl \tag{3.8}$$

and assigning l_s = physical length of sensing fibre and assuming the sensitivity k is constant along the length of the sensing fibre and the electric field seen by the sensing fibre is also constant then

$$\Delta\phi(\lambda) = \frac{4\pi}{\lambda} l_s k V_{ac} + \frac{4\pi}{\lambda} \int \Delta n'(\lambda)\, dl \tag{3.9}$$

The term $\frac{4\pi}{\lambda} \int \Delta n'(\lambda)\, dl$ in equation (3.9) represents the slowly varying or effectively DC phase of the interferometer and this term is likely to represent slow drifts associated with environmental perturbations such as temperature changes.

The term $\frac{4\pi}{\lambda} l_s k V_{ac}$ represents the sensing fibre's response to the applied voltage and this term responds linearly to the applied voltage V_{ac}.

The normalised intensity seen at the detector is then a periodic function of the phase shift described in equation (3.9) and since the detector is placed at the orthogonal input/output arm of the polarising beam splitter (PBS) to the launch arm, the output is a minimum when the total phase shift is an integer multiple 2π. It follows that the normalised output intensity is of the form

$$I_{(\lambda)} = \sin\big(\Delta\phi(\lambda)\big) = \sin\left(\frac{4\pi}{\lambda} l_s k V_{ac} + \psi\right) \tag{3.10}$$

where ψ represents the slowly varying phase term described in equation (3.10)
ie $\psi = \frac{4\pi}{\lambda} \int \Delta n'(\lambda)\, dl$

As a result if slow drifts are filtered out then the phase of the spectral modulation seen in the output spectrum, around the central wavelength of the light source, is linearly proportional to the applied AC voltage V_{ac}.

3.4 *The voltage sensor signal processing scheme*

To implement a voltage sensing system capable of measuring the response at 50 or 60Hz we need to collect output optical spectra and process the data to determine the phase of the periodic modulation with an effective sampling rate that eliminates aliasing. Nyquist’s theorem suggests that a sampling rate of 120 samples per second (sps) is sufficient to respond to a 60Hz test signal. However, the electricity transmission industry is also interested in measuring higher order harmonics and transient responses caused by faults and as a result sampling rates of 2 or 4 ksps have been used. The signal processing scheme developed for the experiments presented in this thesis is based on collecting the spectral data using a high speed optical spectrometer. The spectrometer is connected to a data acquisition system and the data is processed in a high speed digital signal processing system. Both the data acquisition system and the digital signal processing system were custom built for this project by the author and his collaborators.

To determine the phase of the periodic modulation seen in the output spectra a simplified version of a discrete Fourier transform was used. Ideally, in the absence of a test voltage or electric field the phase and period remains constant. In reality the interferometer will be subject to slow drifts due to factors such as temperature changes or other environmental effects. The strategy chosen for the signal processing scheme was to assume that the drifts were both small and slow relative to the 50 or 60 Hz test voltages. The signal processing system would be initialised by processing a single output spectrum in the absence of a test voltage and accurately determine the period and phase of the periodic modulation. It was then assumed that the period would remain approximately constant as it was largely determined by the inherent birefringence of the poled silica sensing fibre and any attached HiBi pigtailing fibre. The period was then stored and phase of the modulation, at the stored period, was monitored by acquiring and processing output spectra at the system sampling rate. Three generations of the signal processing system are presented in this thesis and the effective sampling rate has improved from approximately 0.5 sps to 1000sps and ultimately to 4800sps for the final version of the signal processing system.

The optical spectrometers used in this work record the spectra as discrete collections of samples or pixels. Typically a lab bench-top type optical spectrum analyser (OSA) will record the intensity at 500-1000 samples, equally spaced in wavelength between the start and stop wavelength. Unfortunately the maximum scan rate of OSAs is limited to approximately 1Hz. Recently, high speed compact spectrometers have become commercially available that use a linear array of detectors and the internal optics are designed so that a diffraction grating directs different wavelengths to each detector in the array. The intensity recorded at each detector is then clocked out to a data acquisition system and the optical spectrum can be reconstructed and processed in a digital signal processing system. Although the optics and internal layout of the commercially available compact spectrometers was ideal for our purposes unfortunately the electronic data acquisition system was not capable of fast real time data acquisition. In the course of this work three generations of custom made data acquisition electronic interfaces and the attached high speed digital signal processing system were developed. The three separate generations are described in chapters 6 to 8 which present the experiments and results obtained using each generation.

3.5 The fast phase finder algorithm

The signal processing algorithm used to recover the phase and period of the spectral modulation was based on a discrete Fourier transform (DFT) and a brief Fourier theory primer is presented in section 3.6 below. To simplify the analysis each spectrum, containing intensity values at 256 – 2048 equally spaced wavelengths, was considered as a time based signal. The entire spectrum was processed using a discrete Fourier transform and the magnitude and phase of each Fourier component was calculated. The component with the maximum magnitude was considered the component corresponding to the spectral modulation imposed by the M-TPI and the period of this component was stored in the signal processing system. The signal processing would then begin a monitoring loop that simply calculated the phase of the periodic modulation at the stored period at the effective sampling rate of the system.

3.6 Fourier transform theory in brief

The continuous Fourier transform of a periodic function $f(t)$ from the time domain (t) to the frequency domain (ω) is

$$F(\omega) = \int_{-\infty}^{\infty} f(t)e^{-i\omega t}\,dt \qquad (3.11)$$

where $i = \sqrt{-1}$ and $e^{-i\theta} = cos(\theta) - isin(\theta)$

Sampling the continuous function $f(t)$ above will provide a set of N samples that form part of a periodic extension of the form $x_{0,}\, x_{1,}x_{2,} \dots x_{k,} \dots x_{N-1,}$ where $x_k =$

x_{k+N} . In general $x_{k,}$ can be considered a complex number of the form $x_k = x_{real} - i\, x_{imag}$.

The discrete Fourier transform (DFT) of the N samples above is

$$X(n) = \frac{1}{N} \sum_{k=0}^{N-1} x(k) e^{-i\omega n}/_N \ , \ n = 0..N-1 \tag{3.12}$$

Although the sets of N samples collected from the spectrometer contain real numbers with zero imaginary part, the DFT will in general contain N complex Fourier components. The magnitude and phase of each component can be found as follows.

$$Magnitude = \ \|X(n)\| = \sqrt{\left(X(n)_{real} \times X(n)_{real} + X(n)_{imag} \times X(n)_{imag}\right)} \tag{3.13}$$

$$Phase = tan^{-1}\left(\frac{X(n)_{imag}}{X(n)_{real}}\right) \tag{3.14}$$

where

$$X(n)_{real} \ = \frac{1}{N} \sum_{k=0}^{N-1} x(k) \cos(\frac{\omega n}{N}) \tag{3.15}$$

$$X(n)_{imag} \ = \frac{1}{N} \sum_{k=0}^{N-1} x(k) \sin(\frac{\omega n}{N}) \tag{3.16}$$

The DFT for a single output spectrum is calculated to determine the period of the spectral modulation by selecting the Fourier component $X(max)$ that has the maximum magnitude. The signal processing then continually collects output spectra and the phase of the Fourier component $X(max)$ is then calculated for each spectrum. The calculated phase is then recorded as the output of the signal processing system. The time required to calculate the phase was optimised by storing cosine and sine look up tables at the period corresponding to $X(max)$. The sums set out in equations (3.15) and (3.16) above were calculated using consecutive spectral data sets $x(k)$ and the corresponding phase of the spectral modulation was determined using equation (3.14).

To determine the response of the system due to the applied AC test voltage V_{ac} the calculated phase was then filtered at 50 or 60 Hz.

As mentioned above the signal processing system has undergone considerable development and revisions throughout this project and the experiments are presented in subsequent chapters in a chronological order. For each generation a description of the signal processing scheme is included. However the basic method used is as discussed above for all three generations.

Chapter 4. Polarisation dependence of the linear electro-optic coefficient in thermally poled twin-hole silica fibre

4.1 Thermal poling background

Thermal poling of twin-hole optical fibre was introduced in chapter 2 section 2.5 above and has been widely studied by a number of research groups around the world including the optoelectronics research centre (ORC) at the University of Southampton, the European Union (EU) based "GLAMOROUS PROJECT", and the Optical Fibre Technology Centre (OFTC) at the University of Sydney, along with many other researchers around the world. Thermal poling has been an essential part of the work presented in this thesis; however it is not the central topic of the research. The work presented here has been primarily focussed on sensing, interferometry and design and characterisation of special optical fibres as indicated by the thesis title. For a detailed background in the topic of thermal poling of twin-hole optical fibre the reader is directed to the following two excellent references. The first reference constitutes a comprehensive background for thermal poling and the second is more recent and contains an excellent historical summary of the emergence of poling in its various forms.

1. "Thermally Poled Fibre Devices", Wei Xu, PhD thesis, University of Sydney, 1999 [28].
2. "Poling long lengths of Optical fibre", Ken Lee, PhD thesis, chapter 2.3, University of Sydney, 2006 [29].

Thermally poled twin-hole silica fibre possesses a small linear electro-optic (LEO) response where the refractive index responds linearly to an electric field applied transversely across the fibre core. As stated in section 2.6 above a widely accepted model for the poling mechanism suggests that "charge separation" due to the migration of mobile ions during poling results in a large internal "frozen in" electric field within the fibre after thermal poling. The frozen in electric field acts on the $\chi^{(3)}$ of the fibre to induce an effective $\chi^{(2)}$ using the process described in section 2.4 above [17, 18]. Using the charge separation model the analysis presented in Appendix B equation (B.44) suggests a differential linear electro-optic response (DLEO) for the two polarisation modes of the fibre where one polarisation mode is aligned with the poling direction and the frozen in electric field. Using the conventions described in appendix B section B.6 a ratio of Pockels coefficients $r_{33}\colon r_{31}$ of 3:1 is predicted. The experimental study presented in this chapter reports a much lower ratio of 1.17:1. This result is similar to that reported by Marckmann et al [30] in thermally poled planar waveguides where a ratios of 1.13:1 and 1.09:1 were reported for two separate samples. However Kazansky and Russell previously reported an approximate 3:1 ratio and presented an argument strongly supporting the charge separation model [31]. Despite these discrepancies the observed polarisation dependence in the thermally poled fibres studied here may prove adequate for the voltage sensing application. In this chapter the polarisation dependence of the linear electro-optic response is experimentally determined using two separate interferometric methods. This was the first experimental study in this work as it was essential to establish the existence and magnitude of the DLEO in thermally poled twin-hole silica fibre as an initial step towards the development of a voltage sensor.

4.2 Experiments

The Michelson-two polarisation interferometer (M-TPI) introduced in chapter 3 section 3.2 above is designed to respond to average birefringence or total retardance changes in the sensing section. A DLEO will result in a birefringence change that is a linear function of an electric field applied transversely across the core in the poling direction. Figure 4.1 shows an illustration of the M-TPI constructed using thermally poled silica fibre as the sensing fibre (as described in Chapter 3 section 3.3) that allowed the DLEO to be experimentally determined .

The presence of a non-zero DLEO is essential for the development of the proposed voltage sensor system; however measuring the DLEO only doesn't allow for the ratio

$r_{33}:r_{31}$ to be determined. For completeness an all fibre Mach-Zehnder interferometer (MZI) was constructed that allowed the r_{33} and r_{31} values to be determined individually.

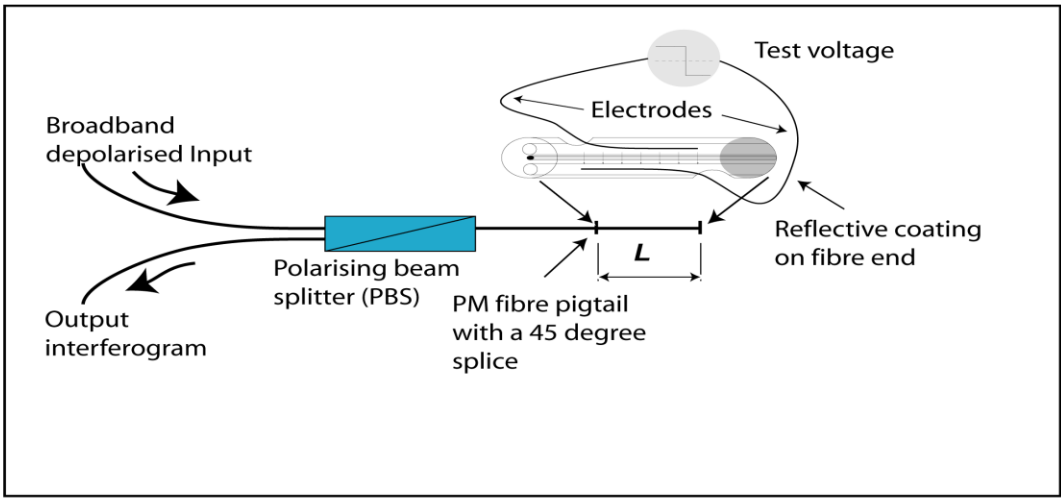

4-1 M-TPI used to determine the DLEO of the thermally poled twin-hole silica fibre

An illustration of the MZI is shown in figure 4-2 where the twin-hole fibre is placed in one arm. The interferometer was designed to excite only a single polarisation mode of the twin–hole fibre by placing a fibre pigtailed polariser at the input of the twin-hole fibre. The twin-hole fibre was pigtailed with polarisation maintaining (PM) fibre and the PM fibre was spliced with the polarisation axes of the PM fibre and the twin-hole fibre aligned. Polarisation controllers in each arm allowed the interferometer fringe contrast to be optimised. The reference arm of the interferometer included a fibre stretcher that relatively slowly (at approx 20Hz) dithered the interferometer through a few full fringes. Simultaneously an audio frequency electrical signal V_{ω} (250V peak to peak @ 8.5 kHz) was applied across the internal electrodes of the twin-hole fibre. The output arms of the interferometer were monitored using photo detectors and since the outputs are complementary i.e 180 degrees out of phase the outputs were summed in a differential amplifier. The output was then sampled using a data acquisition card at 100 ksps. Since the dithering was sufficient to drive the interferometer through a number of fringes, the difference between the maximum and minimum recorded values corresponded to the fringe contrast, $V_{contrast}$. The data was then processed to determine peak to peak audio frequency response at the quadrature points, V_{signal} . The electro-optically induced phase shift in the interferometer could then be determined using the following:-

$$\Delta\phi = 2sin^{-1}\left({}^{V_{signal}}\!\Big/\!{}_{V_{contrast}} \right) \tag{4.1}$$

where $\Delta\phi$ is the phase shift in radians.

Appendix A section A.4 describes the relationship between a DC electric field $E(0)$, the linear and quadratic electro-optic coefficients, and the induced refractive index change. If the third order non-linear term is assumed to be negligible in the following expression for the refractive index, $\mathrm{n}(E) = \mathrm{n} + \Delta\mathrm{n} = \mathrm{n} - \overbrace{\frac{1}{2}\mathrm{n}^3\ \mathfrak{r}E(0)}^{1} - \overbrace{\frac{1}{2}\mathrm{n}^3\ \mathfrak{s}E(0)^2}^{2}$ (see appendix A equation (A.10)) then the electro-optically induced index change due the second order non-linearity is

$$\Delta\mathrm{n} = \frac{1}{2}\mathrm{n}^3\ \mathfrak{r}E(0) \tag{4.2}$$

After poling, if the fibre is probed with the audio frequency signal V_ω then any response at probe frequency ω is due to the electric field E_ω and the linear electro-optic response described by the Pockels coefficient $\mathfrak{r}$. To calculate the electric field the fibre cross section and the position of the electrode wires within the holes must be known. Unfortunately there is considerable uncertainty in the exact position of the electrode wires making it difficult to calculate the electric field seen by the core. Xu proposed a method [28] to estimate an effective separation distance d_{eff} that allows the electric field seen by the core to be estimated using the following:-

$$E_{core} = {}^{V_\omega}\!\Big/\!{}_{d_{eff}} \tag{4.3}$$

where d_{eff} is calculated from the fibre cross section and electrode dimensions and the electrode is assumed to be in the centre of the hole as follows

$$d_{eff} = 2\frac{\boldsymbol{\varepsilon}}{\varepsilon_0} d_{air} + d_{spacing} \tag{4.4}$$

$d_{spacing}$ is the thickness of the glass bridge between the holes containing the core and d_{air} is the air gap between the surface of the electrode wire and the glass surface or edge of the hole. The electric permittivity $\boldsymbol{\varepsilon}$ over the permittivity of free space ε_0 i.e. $\frac{\boldsymbol{\varepsilon}}{\varepsilon_0}$ is the dielectric constant. Assuming the electrode is in the centre of the hole gives

$$d_{air} = \frac{1}{2}(d_{hole} - d_{wire}) \tag{4.5}$$

The phase shift recorded by interferometer using (4.1) above is equal to

$$\Delta\phi = \frac{2\pi L}{\lambda}\Delta\mathrm{n} \tag{4.6}$$

where L is the length of the poled section, and λ is the free space wavelength. Substituting the refractive index change $\Delta\mathrm{n} = \frac{1}{2}\mathrm{n}^3\,\mathfrak{r}$ into (4.4) leads to the following expression for $\mathfrak{r}$

$$\mathfrak{r} = \frac{\lambda d_{eff}}{\pi V_\omega L\mathrm{n}^3}\,\Delta\phi \tag{4.7}$$

where n is the refractive index of the fibre core.

Depending on the input polarisation either r_{33} or r_{31} is measured. Using the conventions described in appendix B section B.6, r_{33} corresponds to the input polarisation parallel to the poling direction and r_{31} corresponds to the input polarisation perpendicular to the poling direction.

Despite the uncertainty in the exact electrode position it is possible to determine the ratio $r_{33}\!:\!r_{31}$ by measuring r_{33} and r_{31} separately using the same test conditions i.e. with the same test voltage and assuming no change in the electrode position.

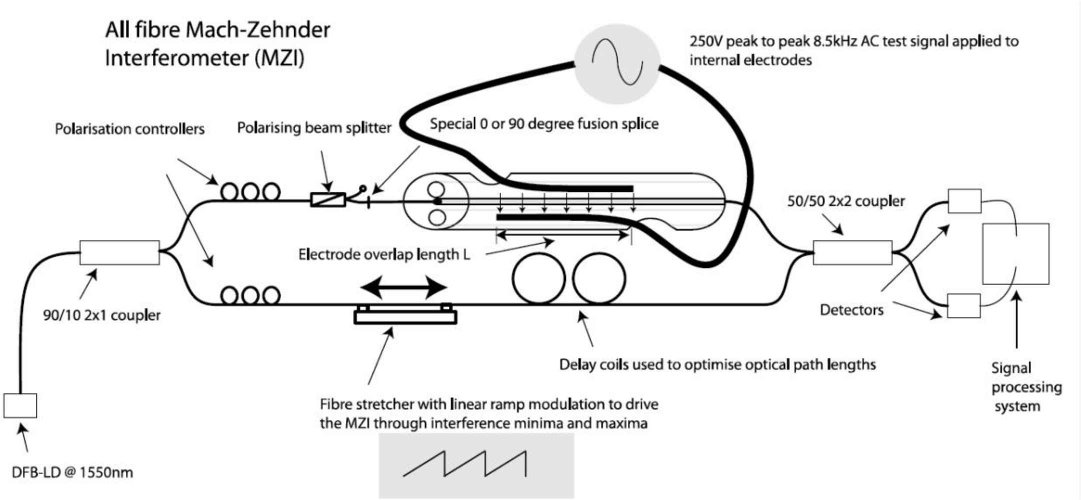

4-2 MZI with polarisation control

In the MZI, shown in figure 4-2 above, the input polarisation could be configured to measure either r_{33} or r_{31} separately by making either a 0 or 90 degree splice respectively between the output PM pigtail of the PBS and the input PM pigtail of the twin-hole fibre. The PM pigtails were made sufficiently long so that they could be spliced and respliced without disturbing or moving the twin-hole fibre and more importantly not changing the position of the internal electrode wires. This allowed the values of r_{33} and r_{31} to be logged for long enough to determine the average values for improved accuracy.

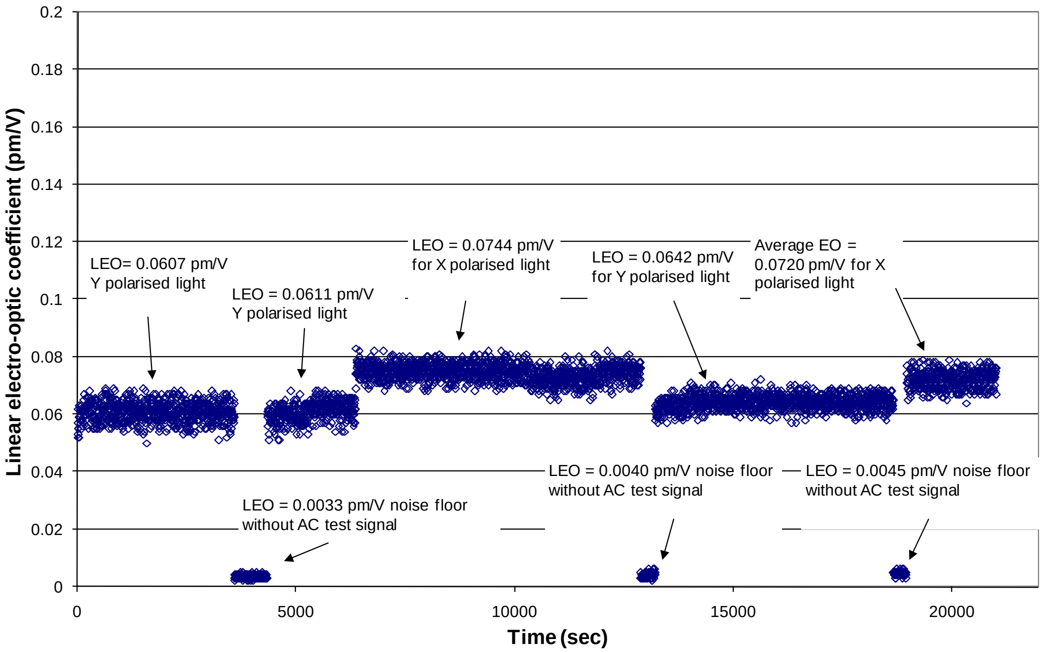

4-3 Measured r_{33} and r_{31} values. Data marked X and Y polarised light correspond to r_{33} and r_{31}respectively.

The thermally poled twin-hole, identified as OD-005-J, was fabricated at the OFTC and a cross sectional image is shown in figure 4.4. The fibre was designed to be single mode at 1550nm and the approximate fibre dimensions are; fibre diameter 250µm, hole diameter 90 µm, glass bridge thickness 19 µm, tungsten electrode wire diameter 50 µm and electrode overlap 480mm. The electrodes were inserted through side polished holes that exposed the internal holes. The twin-hole fibre was then thermally poled with 3kV DC applied across the internal electrodes while the fibre was maintained at 280 deg C for 30 minutes.

The linear electro-optic response of this type of thermal poled fibre is known to decay [32-34] and although there is evidence of fast decay processes directly after poling the linear electro-optic response is relatively stable after a few days. Margulis reported negligible decay over 12 months at room temperature for thermally poled fibres produced by the European Union (EU) based GLAMOROUS project [35]. To allow the fast decay processes to stabilise the r_{33} and r_{31} values were recorded about 4 weeks after poling using the methods described above. The logged values shown in figure 4.3 above were all recorded on the same day with only a small delay of approx 10 minutes between recordings when the input polarisation was swapped. Figure 4.3 shows that the average value for r_{33} is greater than the average value for r_{31} and continued swapping of the input polarisation produced good repeatability. However the experimentally determined value for the ratio $r_{33}:r_{31}$ was approximately 1.17:1.

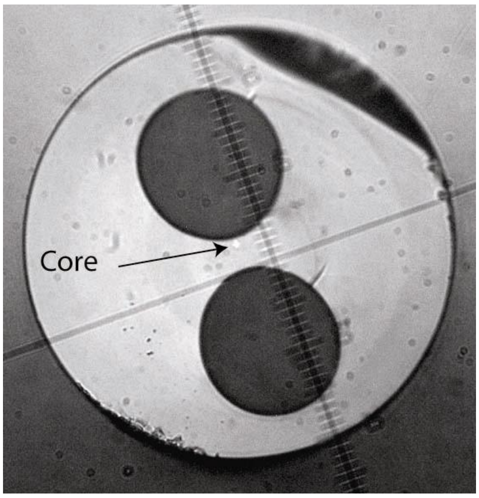

4-4 Twin-hole fibre cross section

In summary the experiment above confirmed that there is a small polarisation dependence in the electro-optic response for the tested sample of twin-hole thermally poled silica fibre.

The same sample of thermally poled twin-hole fibre was then used to configure the M-TPI as in figure 4.1 above. In this case the response is only due to the DLEO. This is essentially the same configuration as the proposed voltage sensor with the exceptions that the poled fibre is not coiled and the electrode wires are still inside the fibre. To interrogate the sensor a broad band erbium doped fibre –spontaneous emission source (EDF-ASE) was used to illuminate the M-TPI and the output spectrum was recorded using an optical spectrum analyser (ANDO 6315B). The output spectrum was recorded with both +125V and -125V applied across the internal electrode wires. The input and a pair of output spectra are shown in figure 4.5. A small phase shift can be seen in the periodic modulation between the two recorded output spectra. The data was then processed to calculate the phase difference. The DLEO was then calculated assuming the average position of the electrode wires within the holes was unchanged relative to the previous experiments using the MZI.

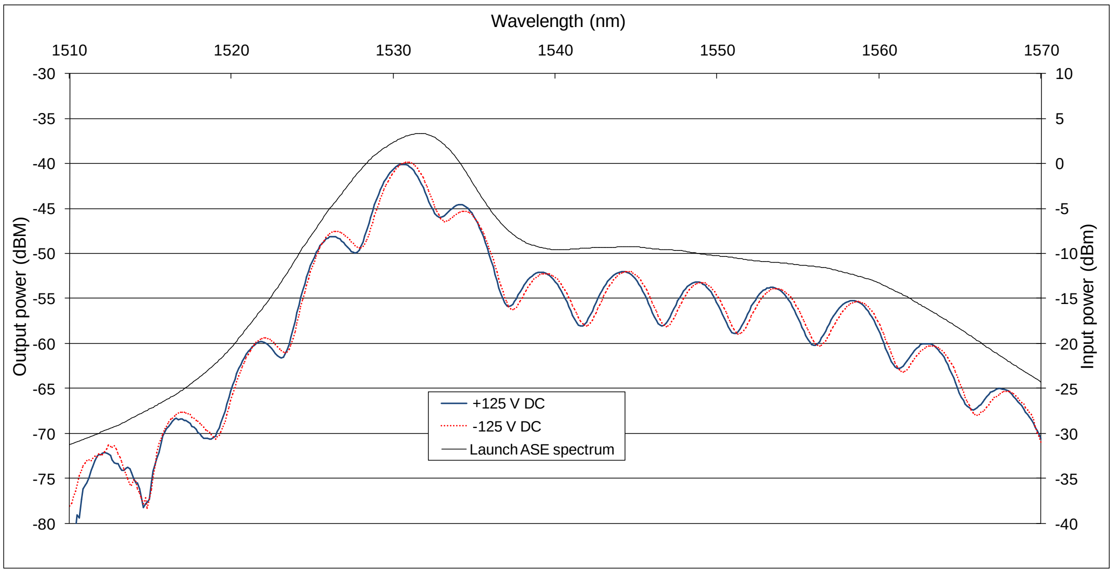

4-5 M-TPI input and output spectra with +125 and -125V DC applied across internal electrodes

In this case the electro-optically induced phase difference is simply the measured phase difference between the two recorded spectra. To calculate the DLEO i.e. r_{33} - r_{31} the following relationship can be used.

$$DLEO = r_{33} - r_{31} = \frac{\lambda d_{eff}}{\pi \Delta V L \mathrm{n}^3} \Delta\phi \qquad (4.8)$$

Where ΔV is the difference in the two test voltages. The experiment was repeated four times by collecting pairs of output spectra with both +125V and -125V (i.e. $\Delta V =$ 250V DC) applied across the core. The DLEO was then calculated for all four pairs of output spectra. The values returned by the four sequential tests were 0.0136, 0.0145, 0.0110, and 0.0140 pm/V giving an average of 0.0133pm/V. In the previous experiment using the MZI the values of r_{33} and r_{31} were determined separately by logging measurements and calculating two pairs of average values. In this case the DLEO was calculated simply by subtraction giving a DLEO of 0.0135 and 0.0080 pm/V.

In both experiments the experimental noise floor when no test voltage was applied was lower than the spread in subsequent measurements when the electrical test signal was applied. This was most likely due to the electrodes moving around under the influence of electrostatic force. Electrode movement will alter the electric field seen by the core even if the test voltage is stabilised.

4.3 Discussion and conclusion

The results from these two separate experiments clearly demonstrate that the linear electro-optic response for the thermally poled twin-hole fibre tested here is polarisation dependent. The second experiment using the M-TPI measured the differential linear electro-optic response only. This was the first experimental step towards demonstrating the feasibility of using the M-TPI combined with thermally poled twin-hole fibre for voltage sensing.

The measured ratio $r_{33}:r_{31}$ of 1.17:1 differs from the predicted ratio of 3:1. Departures from the assumptions used to arrive at the predicted 3:1 ratio are likely to be responsible for the difference. As stated above the ratio $r_{33}:r_{31}$ measured in thermally poled silica planar waveguides by Christensen et al was similar. More specifically, two possible causes for the discrepancies are:-

Firstly, in the analysis the electric field distribution, due to the frozen in field, around the core is assumed to be uniform and parallel across the core. Due to the mostly circular shape of the core, fibre, and the holes it is unlikely that the frozen in field has conveniently arranged itself as parallel charged plates. Recently Hong-lin An and Fleming have demonstrated using second harmonic generation microscopy that the migration of the non-linear region in thermally poled fibres is inhibited around the core, possibly by the core cladding interface [36, 37]. The resulting wrapping of the non-linear region around the core (see figure 4-6) would reduce the polarisation dependence and possibly contribute to the enhanced $\chi^{(3)}$ observed in thermally poled fibres by Xu et al [38]. The thermally poled planar waveguides studied by Markmann et al [30] may also have suffered from this wrapping effect even though the poling fields in the planar structure were more representative of the ideal parallel structure assumed in the analysis.

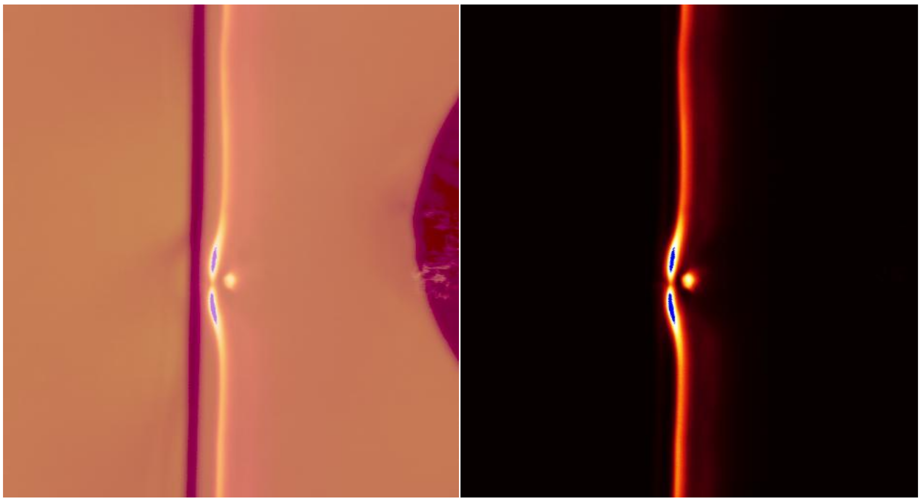

4-6 Visualisation of the second order non-linear layer in thermally poled fibre, showing the wrapping around the core (image provided by Hong Lin An)[36, 37]

A second assumption in the analysis is that the dielectric remains isotropic after thermal poling and that a frozen in electric field acting on the $\chi^{(3)}$ produces the second order non-linearity. The DC electric fields applied across the core during thermal poling are very strong and are near to the electric breakdown of silica. The assumption that the silica remains an isotropic dielectric after thermal poling is also unlikely. The presence of macroscopic alignment of dipoles will also cause a departure from the 3:1 ratio [39, 40].

Regardless, the purpose of this experimental study was to measure the DLEO of the thermally poled twin-hole fibre and confirm the response of the M-TPI is to the DLEO only and this has been achieved.

Chapter 5. Twin-hole fibre design considerations

5.1 Introduction

To help understand the linear electro-optic response seen in thermally poled twin-hole fibre it is useful to gain an understanding of the geometry of the non-linear region. Assuming the charge separation model is a major contributor to the enhanced non-linearity it would be reasonable to assume the region between the anode and cathode holes is where the partially trapped charges reside after poling [17, 18, 41-43]. Some very effective methods have been used to try to determine accurately the spatial distribution of both the trapped charges and the non-linear region itself.

Four methods that have provided insights into the charge distribution are listed below.

1. Observing differential longitudinal acid etch rates over the cross section of the poled fibre. The presence of ions alters the etch rate revealing a landscape that is representative of the distribution of ions [17, 34, 44].
2. Observing second harmonic generation during transverse acid etching and correlating the etched region with the local non-linearity [45-48].
3. Second harmonic generation optical microscopy. Focussing intense light and observing the second harmonic generation. This method provided good spatial resolution[36, 37].
4. Laser induced pressure pulse probing of charge distribution. Charge distribution has been mapped with a spatial resolution of approximately 3µm by monitoring laser pulse induced currents inside thermally poled fused silica [49].

(a) **Method 1**

The first method highlighted the presence of highly confined ridges where it is suggested that significant localisation of ion concentration has occurred. The images in figure 5-1 below are taken from the literature and in all three cases the acid etching is transverse to the poling direction. The clear ridges seen in the first image are of an acid etched thermally poled fused silica glass slide (or coverslip). The other two images are of thermally poled twin-hole silica fibre. The wrapping of the ion concentration region around the core can be seen in the middle image further supporting the argument presented in chapter 4 regarding the reduced polarisation dependence of the linear electro-optic response seen in poled fibres.

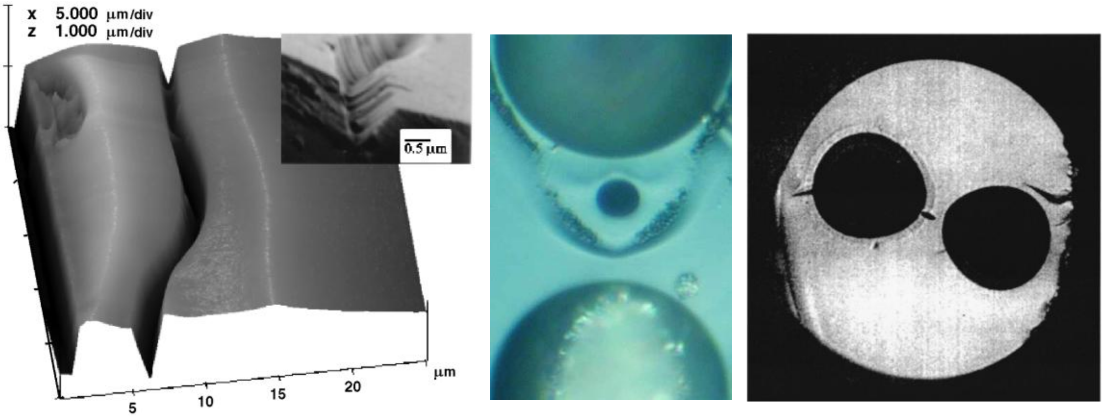

5-1 Images obtained from the literature using method 1. Corresponding authors for the images from left to right Alley & Brueck 1998, Myrén & Margulis 2005, and Blazkiewicz et al 2001 [17, 34, 44].

(b) Method 2

The second method involved acid etching parallel to the poling direction. The poled sample is illuminated and the magnitude of the second harmonic generation for the sample is monitored. As the sample is etched away both the thickness and the change in second harmonic generation is monitored. From the resulting data the magnitude of the local non-linearity can be assessed. This method revealed regions of not only large gradients in the magnitude of the local non-linearity but also of sign reversal, possibly indicating a change of sign of the frozen-in electric field.

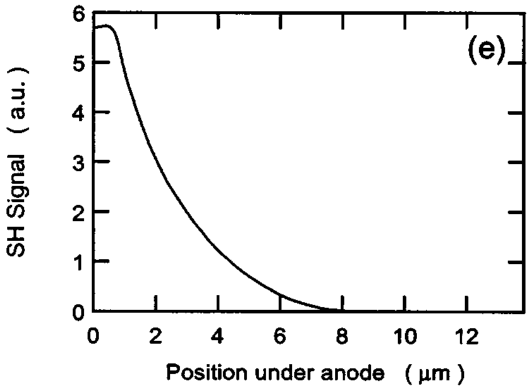

5-2 Results obtained using method 2 by Kudlinski, Quiquempois et al[45-47]

(c) **Method 3**

Method 3 provided good spatial resolution and allowed the distribution of the non-linear region to be mapped out.

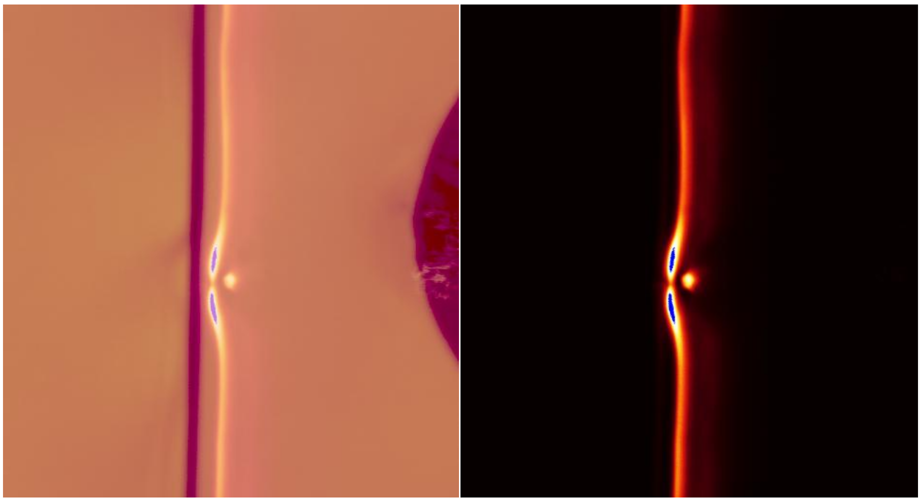

5-3 Results obtained using method 3 showing a highly localised non-linear region partially surrounding the core [image provided by Honglin An and Fleming]

These results suggest that when designing the twin-hole fibre cross section the position of the core between the anode and cathode hole is crucial in determining the ultimate electro-optic response of the poled fibre. Also note that the power distribution of the fundamental mode in a step index fibre is usually considered to be Gaussian in shape and light in the tails of the mode extend into the inner cladding region [50]. The measured electro-optic response of a poled fibre, monitored using light travelling in the core, is essentially a weighted average of the local electro-optic response over the region swept out by the mode as it travels along the length of the fibre. Since the mode can be large relative to the local scale of the non-linear distribution it is important to both position the core in a region of high average non-linearity, and design a refractive index profile that results in a mode that remains close to the core.

The literature suggests that the region near the anode hole potentially possesses higher non-linearity and early designs of twin-hole fibre for use in voltage sensing focussed on positioning the core very close (within 2-3 microns) of the anode hole to exploit the “anode effect” [44]. This region however is also a region of high non-uniformity as revealed by method 2 above and further supports the need for a highly confined mode.

In this chapter various analysis and design considerations for the twin-hole fibre are discussed. Experimental results showing larger than expected wavelength dependence in the linear-electro-optic response are presented, supporting the observation that the non-linear region is varying on a scale smaller than the scale of the mode. This concept is extended to the development of a non destructive test method that may lead to the optimisation of the overlap of the mode with the region of high average non-linearity and if used in-situ during poling may assist in optimising poling conditions.

5.2 Mode field diameter in step index fibres

The Marcuse model is often used for estimating the mode field diameter of a step index fibre at a particular operating wavelength. The Marcuse model uses a Gaussian shaped mode profile as an approximation for the intensity distribution of the mode [50]. The model has been widely used and tested particularly since the emergence of erbium doped fibre amplifiers (EDFAs) where maximising overlap of pump and signal modes at 980 and 1550nm is essential for optimising amplifier performance [51]. In the case of twin-hole fibre the core itself may be considered to have a step index profile but the presence of the two large holes should be considered in estimating the mode field diameter. Two approaches have been used here to estimate the mode field diameter. Firstly, the Marcuse model has been used, ignoring the presence of the holes, to estimate the mode field diameter of a real fibre cross section at four operating wavelengths. The wavelengths were selected to cover a broad range and also where semiconductor laser diodes are readily available i.e. 834, 980, 1310, and 1550nm. The chosen fibre had a cut-off wavelength below 820nm.

Secondly, since the emergence of photonic crystal fibres (PCFs) containing arrays of holes within a silica host, new methods have evolved to model the distribution of modes within such "holey" structures. A method known as "Fourier Decomposition Method with Adjustable Boundary Conditions" (FDMABC) was specifically developed to calculate accurately and efficiently the confinement loss in PCFs. FDMABC [52] has been used as an alternative method to model the mode distribution of twin hole fibre and a comparison of results using these two methods is included below.

5.3 The twin-hole fibre cross section

The cross sectional geometry of the fibre known as (OD-0133-03A) was measured accurately using an Olympus optical microscope and the refractive index was determined using a YORK refractive index profiler. The information was combined to form an accurate refractive index cross sectional profile. Figure 5-4 below shows the reconstructed refractive index profile using a 200 x 200 square grid matrix with each cell being 0.1 x 0.1 microns in size. Due to the close proximity of the core to the anode hole the grid was extended only to include the edge of the anode hole.

For many of the twin-hole fibres the core became elongated into an elliptical shape during the fibre drawing process due to the partial collapse of the holes. The collapse can be minimised by drawing at a relatively low temperature. However the ellipticity results in a significant and useful level of form birefringence. The ellipticity of the core, in this case a core that is approx 3.2 by 2.2 microns in diameter, resulted in a beat length of approximately 10mm at 1550nm. This provided the polarisation maintaining properties necessary for the voltage sensor experiments using the Michelson two polarisation interferometer (M-TPI).

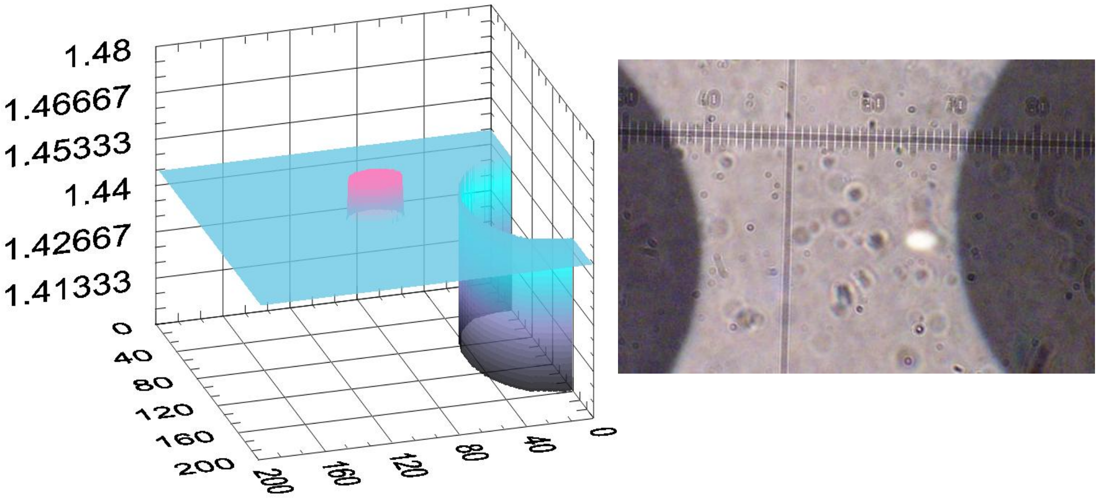

5-4 Reconstructed refractive index profile of the twin-hole fibre OD-0133-03A and cross sectional image showing the elliptical core and proximity to the anode hole

5.4 Fourier Decomposition Method with Adjustable Boundary Conditions (FDMABC) results

The FDMABC software outputs intensity versus the cross sectional matrix for both x and y polarised lowest order core (or fundamental mode). The intensity is plotted on the vertical axis in arbitrary units. Figure 5-5 shows intensity distribution for the x polarised fundamental mode at 834nm.

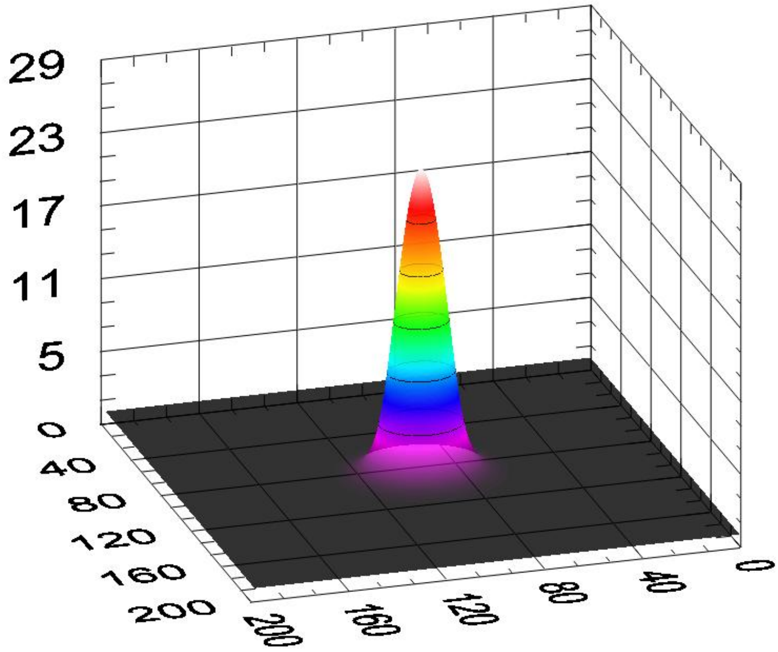

5-5 The FDMABC mode intensity profile at 834nm; intensity is shown on the z axis using arbitrary units

The mode field diameter is easily determined from the intensity plot using the standard definition i.e. when the intensity decays to e^{-2} from the peak power. In this case where the mode is slightly asymmetrical, due to the presence of the anode hole, the distance between the e^{-2} points on either side of the peak is used to determine the mode field diameter.

It can be seen from figure 5-5 that at 834 nm the light is highly confined to the core and the mode is almost symmetrical despite the presence of the anode hole so close to the right hand side of the core. Figure 5-6 shows that at 1550nm the mode begins to spread significantly and now the presence of the anode hole is clearly confining the mode more strongly on the anode hole side of the core. Clearly the presence of the anode hole is slightly reducing the mode field diameter as the wavelength is increased.

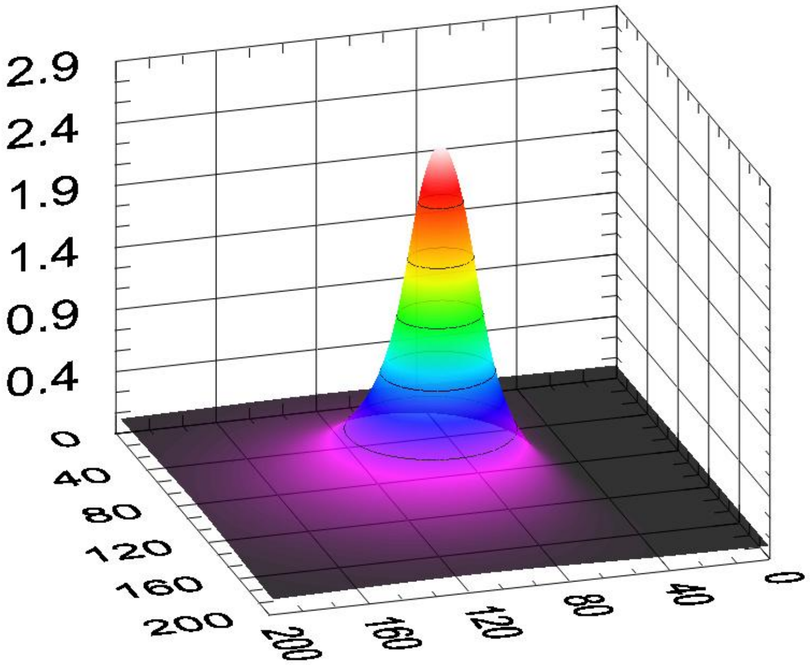

5-6 The FDMABC mode intensity profile at 1550nm; intensity is shown on the z axis using arbitrary units

5.5 *Marcuse model results*

The mode field diameter of a step index fibre, w_0 can be accurately estimated using

$$w_0 = a\left(0.65 + 1.619\mathrm{V}^{-3/2} + 2.879\mathrm{V}^{-6}\right) \tag{5.1}$$

where a is the radius of the core region, and V is the normalised frequency [50]. The normalised frequency can be calculated at any wavelength λ using

$$\mathrm{V} = \frac{2\pi a}{\lambda}\left(\sqrt{n_1^2 - n_2^2}\right) \tag{5.2}$$

where n_1 and n_2 are the core and cladding refractive indices respectively. The quantity $\sqrt{n_1^2 - n_2^2}$ is known as the numerical aperture (NA).

$$V = \frac{2\pi a}{\lambda}\left(\sqrt{n_1^2 - n_2^2}\right) = \frac{2\pi a}{\lambda}\mathrm{NA} \qquad (5.3)$$

From the fibre refractive index profile shown in figure 5-4 and using equations (5.1) and (5.2) the mode field diameter at 834, 980, 1310, and 1550nm was calculated.

5.6 *Comparison with previous methods*

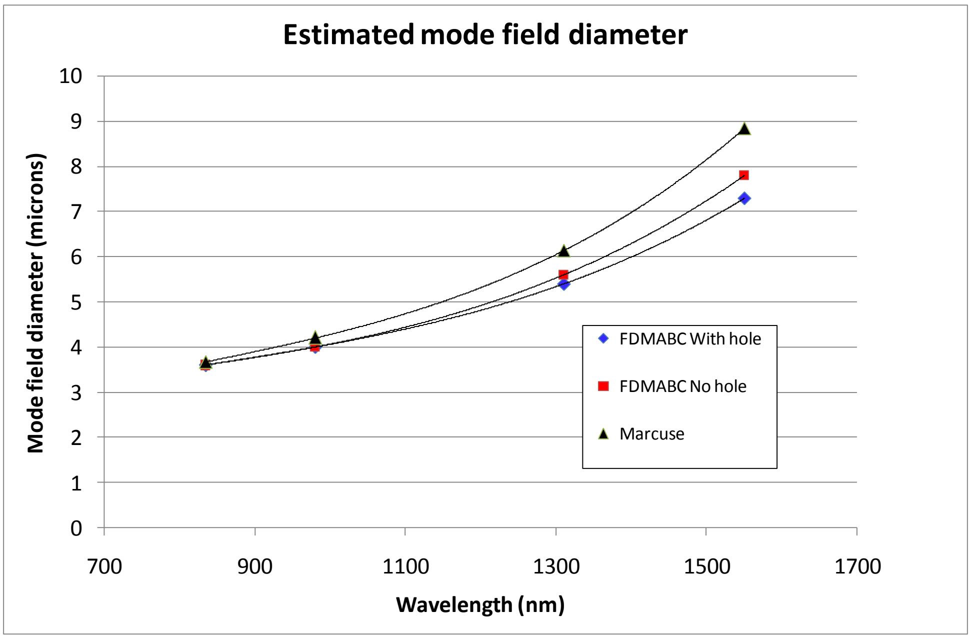

5-7 Mode field diameter calculations using both the FDMABC method and the Marcuse model

Figure 5-7 shows good agreement between the methods at the shorter end of the wavelength range. Since the fibre studied had a cut off wavelength around 800nm and a relatively high NA (0.19) the light is well confined to the core in this wavelength region and the presence of the hole has little or no influence on the mode profile. As the wavelength is increased the mode begins to spread out and the mode begins to see the anode hole. The result is that the calculated mode field diameter, using the two methods, begins to diverge as the wavelength is increased.

5.7 *Designing a new twin-hole fibre*

A new fibre was designed with a principal goal of providing a relatively small mode field diameter at the operating wavelength of 834nm. The study above suggested that when operating near to the cut-off wavelength the much simpler Marcuse model could be used for estimating the mode field diameter. The design was focussed on determining an optimum target core diameter given that a readily achievable range for the fibre NA of 0.2 to 0.3 was possible. Operation near to the cut-off wavelength also helped to minimise the mode field diameter for the resulting fibre.

The following graph shows the calculated mode field diameter versus the core NA for core diameters of 1.6, 2.4, and 3.2 microns respectively.

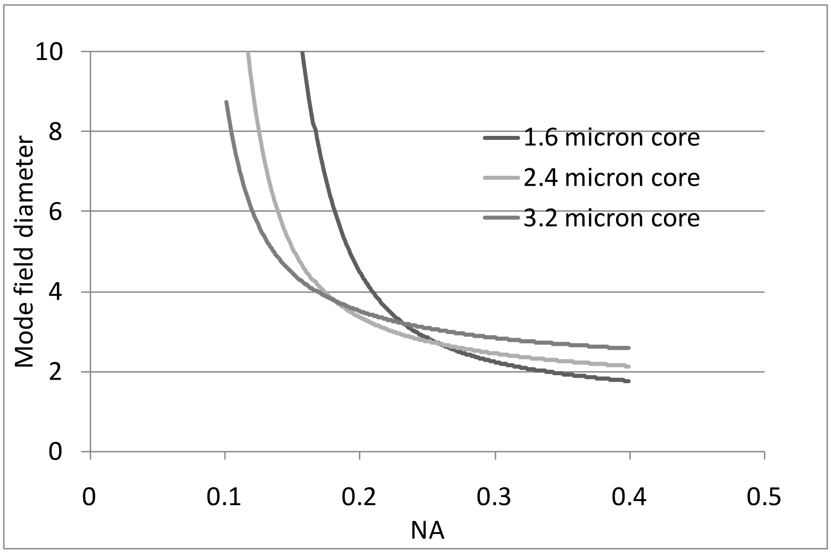

5-8 Mode field diameter versus NA for core diameters of 1.6, 2.4, and 3.2 microns

The plot of mode field diameter versus NA for a core diameter of 2.4 microns appears to be both relatively low and flat in the region spanned by an NA of 0.2 and 0.3. Integrating the mode field diameter, or area under the curve, between an NA of 0.2 and 0.3 showed a minimum when the core diameter is approximately 2.0 microns. It follows that selecting a core diameter of 2.0 microns and targeting an NA of 0.25 was a good starting point, with a resulting cut off wavelength estimated to be 785nm. Allowing for fabrication tolerances by calculating the cut off wavelength for the NA ranging from 0.24 – 0.26 and core diameter varying from 1.8 – 2.2 microns, gave a cut off wavelength ranging from 740nm to 830nm.

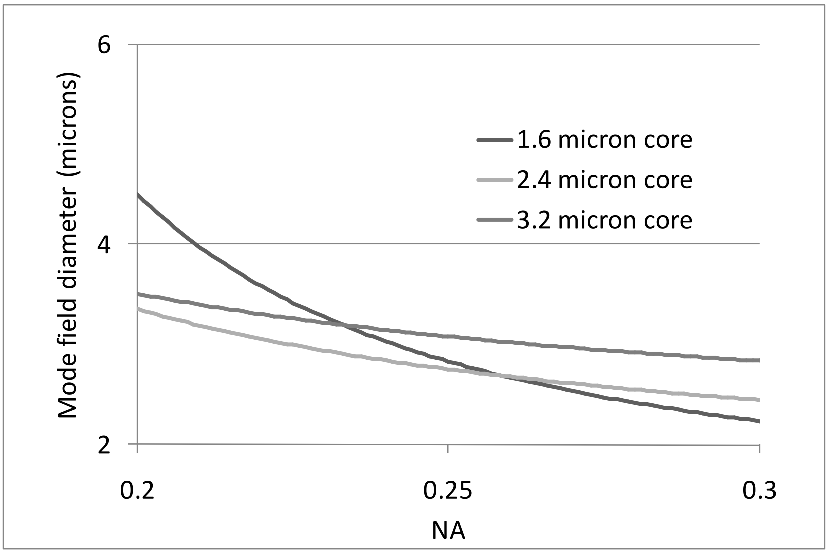

5-9 Mode field diameter versus NA for core diameters of 1.6, 2.4, and 3.2 microns

5.8 Multi-wavelength interrogation of thermally poled twin-hole fibre

On the basis of the discussion presented above an all fibre Mach-Zehnder interferometer (MZI) was designed and constructed that allowed the thermally poled fibre to be interrogated at four different wavelengths without the need for re-splicing or re-configuration of the interferometer. Figure 5-10 below shows an illustration of the all fibre MZI.

The wavelength division multiplexing (WDM) couplers used were designed for use in erbium doped fibre amplifiers, to both combine and separate the 980nm pump and the 1550nm signal. The fibre pigtails of the common port of the WDMs are designed to be single mode over a broad range of wavelengths so that, in the erbium doped fibre, both the 980nm pump and the 1550nm signal modes have maximum spatial overlap [51]. Fortunately the cut-off wavelength was below 834nm, and the WDMs also provided the necessary directivity at 834nm and 1310nm with some additional insertion loss.

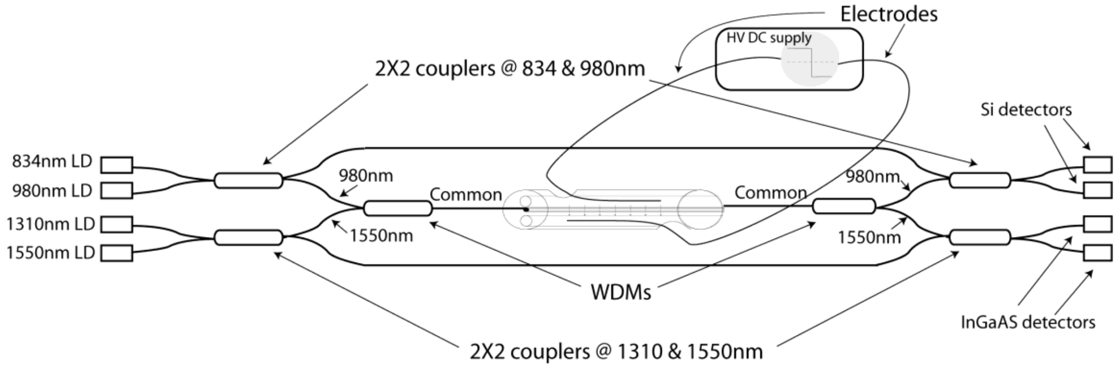

5-10 The all fibre multi-wavelength Mach-Zehnder interferometer

The thermally poled twin-hole fibre shown in figure 5-10 above can be interrogated at any of the four laser diode (LD) wavelengths simply by switching one LD on at a time. When using either the 834 or 980nm LD the output was monitored at the silicon detectors, and similarly the 1310 and 1550nm output was monitored at the InGaAs detectors. Switching interrogation wavelengths was a relatively straightforward process and only involved manually changing external electrical connections. More importantly it was possible to reconfigure the system without disturbing the twin-hole fibre in any way.

In chapter 4 a similar experiment using an all fibre MZI operating at a single wavelength was described and the Pockels coefficient was determined from the electro-optically induced phase shift using

$$\mathfrak{r} = \frac{\lambda d_{eff}}{\pi V_{\omega} L \mathrm{n}^3}\ \Delta\phi \tag{10.4}$$

When calculating $\mathfrak{r}$ over a range of wavelengths the fibre dispersion needs to be considered. To estimate the dispersion the Sellmeier equation has been used. The Sellmeier equation is an empirical relationship between refractive index and wavelength of the form:-

$$n^2(\lambda) = 1 + \frac{B_1\lambda^2}{\lambda^2 - C_1} + \frac{B_2\lambda^2}{\lambda^2 - C_2} + \frac{B_3\lambda^2}{\lambda^2 - C_3} = 1 + \sum_i \frac{B_i\lambda^2}{\lambda^2 - C_i} \tag{10.5}$$

The coefficients B_i and C_i can be found in handbooks and the values used to calculate the dispersion of OD-0133-03B were taken from Bansal and Doremus [53].

The following chart shows a chart recording of the measured Pockels coefficients for a section of thermally poled fibre probed at the 4 different wavelengths. The fibre number was OD-0133-03B and the poled section was 27.5cm in length. The sample was poled using 4kV DC at 300 deg C for 30 minutes and the following experiments were conducted 22 days after poling. A fibre cross section of OD-0133-03B is shown in figure 5-11 below where the close proximity of the core to the anode hole can be seen.

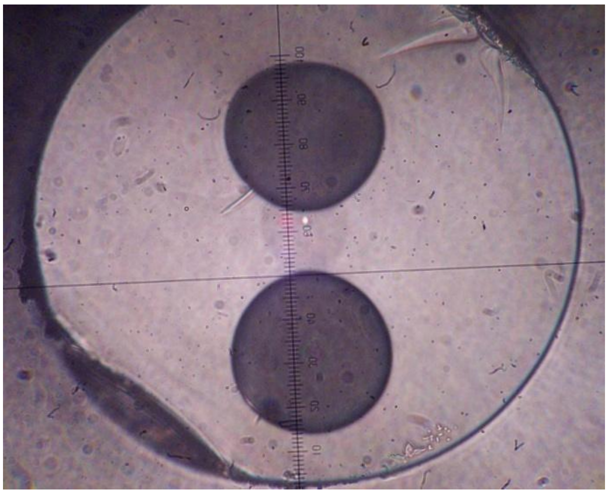

5-11 OD-0133-03B fibre cross section

Taking an average at each probe wavelength and plotting the average value for r versus wavelength indicates a stronger than expected wavelength dependence (see figure 5-13 below).

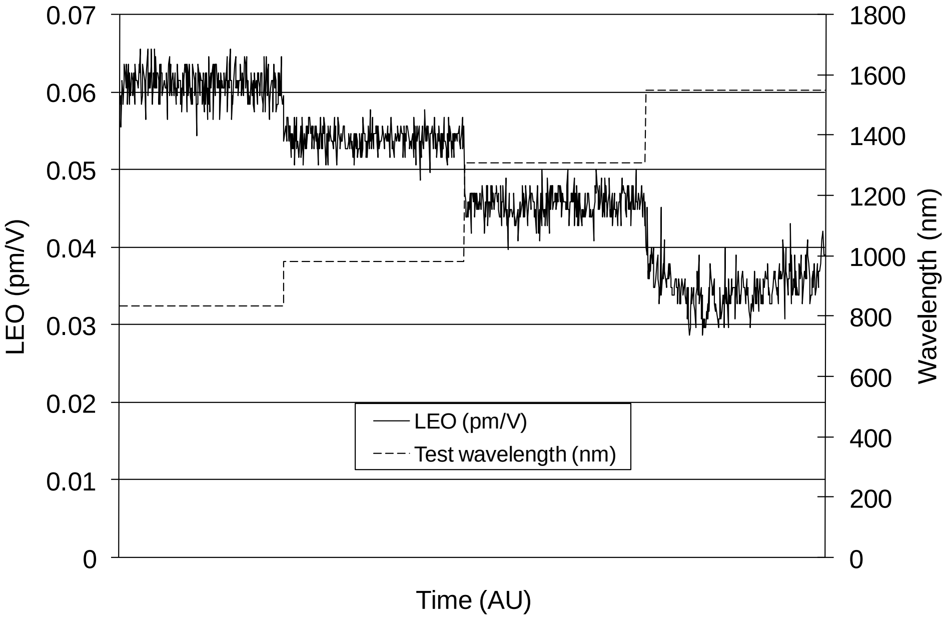

5-12 Linear electro-optic response at 4 different wavelengths

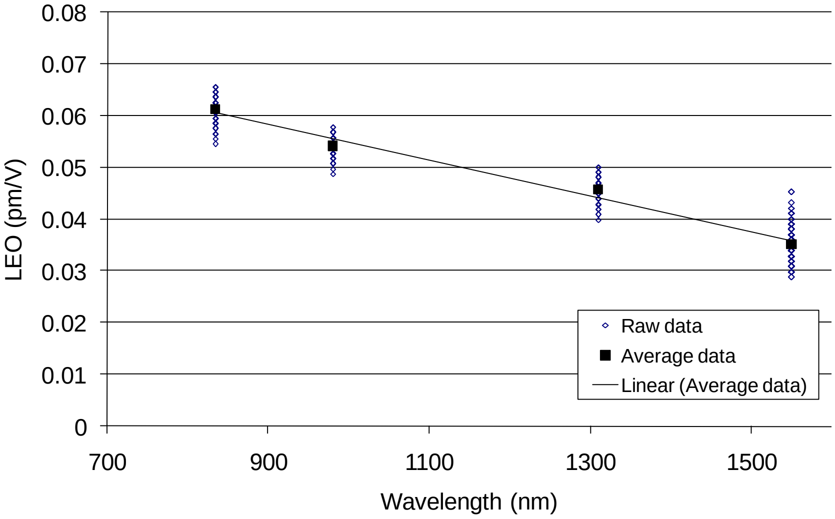

5-13 Linear electro-optic response versus wavelength

Changing the wavelength effectively changes the spatial resolution of the optical probe. Since the mode field diameter of the probe is larger than the physical core of the fibre, the probe is effectively sampling both the core and the inner cladding region. With increasing wavelength the probe samples deeper into the cladding region. The results presented in figure 5-13 show that the effective linear electro-optic coefficient is inversely related to the wavelength.

5.9 Conclusion

The conclusion that the non-linear region is non-uniform around the core of the twin-hole fibre is strongly supported by the multi-wavelength experiments presented in this chapter, and by the literature, and with all the methods discussed in section 5-1 above showing highly confined regions of high non-linearity. The multi-wavelength interrogation method presented here represents a non-destructive method that reveals information regarding the overlap of the region of high non-linearity with the core of the twin-hole fibre. In addition, monitoring the electro-optic response at multiple wavelengths during thermal poling may assist in optimising poling conditions.

Following the analysis and experiments presented in this chapter the twin-hole fibre design was revised to not only include a new target core diameter and NA but also the position of the core relative to the holes was revised. Subsequent designs of twin-hole fibre positioned the core symmetrically between the two holes since this is a region of improved uniformity, but perhaps slightly lower, non-linearity.

Chapter 6. Generation 1 of the voltage sensing and signal processing system

6.1 Introduction

Many improvements in the signal processing system have occurred throughout this work resulting in three separate generations of the signal processing system. Each generation has outperformed the previous in terms of spectral data acquisition speed, and data synchronisation. The data processing techniques outlined in chapter 3 section 3.4 – 3.6 remained approximately the same throughout the evolution of the 3 generations. This chapter describes the first generation that used all standard laboratory test equipment, such as the ANDO 6315B optical spectrum analyser (OSA), and allowed for a demonstration of the proposed voltage sensing methods

6.2 Experiments

Following on from the work presented in chapter 4 a signal processing system was constructed that allowed the Michelson-two polarisation interferometer (M-TPI) to be interrogated and tested with an approximately sinusoidal test voltage. The M-TPI was configured using a section of poled fibre from the same batch used in the previous experiments presented in chapter 4 (OD-005-J). The sine wave was effectively synthesized from 10 equally spaced DC voltages. At each DC voltage a complete output spectrum was recorded with the OSA. A lab computer (PC) running National Instruments Labview software controlled the generation of the DC test voltage via a D/A card and a DC amplifier, and the data acquisition from the OSA. The recorded spectra were also processed by the same PC using Labview. This automation of the test system allowed for both the generation of DC test voltages, and the recording of the output spectra at equally spaced time intervals. The speed was limited by the approximate 1 second acquisition time of the OSA. Since a single cycle of a sine wave was synthesized using 10 samples per cycle, over 10 seconds was required to complete a single cycle of testing. A block diagram of the test system is shown below.

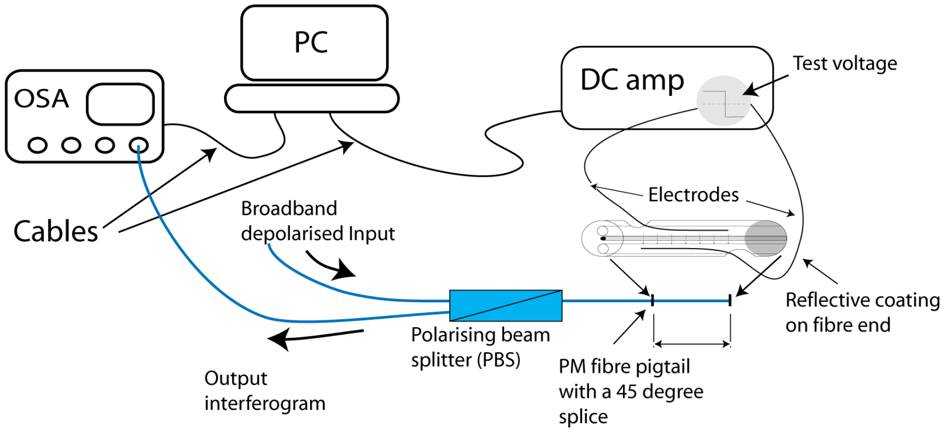

6-1 A schematic diagram of generation 1 of the voltage sensor signal processing system

Complete output spectra (interferograms) were collected at each applied DC voltage and the phase, period and amplitude of the spectral modulation were calculated for each interferogram using a discrete Fourier transform (DFT). This process was repeated for five complete cycles and using five different amplitudes.

6.3 Results and discussion

The raw results at five different AC test voltages are presented in figures 6-2 to 6-6 below. The red round dots represent the DC test voltages and a line joining the dots is drawn to help visualise the synthesised sinusoidal AC test voltage for five complete cycles. The dark blue diamonds represent the calculated phase of the periodic modulation seen in the recorded spectrum at each DC test voltage i.e. the response of the system. Again a line is drawn.

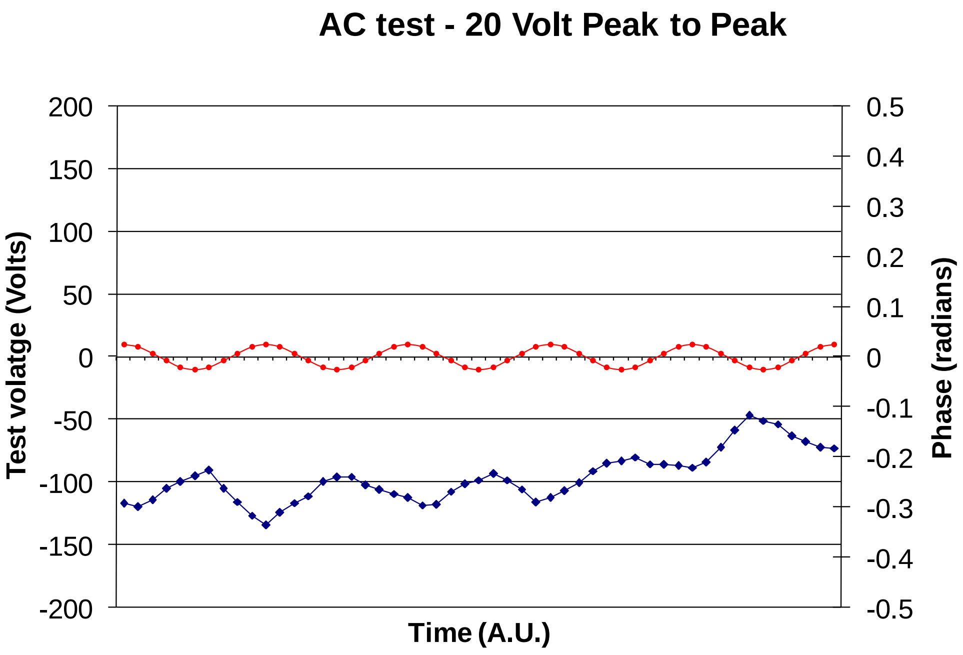

6-2 Five cycle internal electrode AC test – 20 volt peak to peak

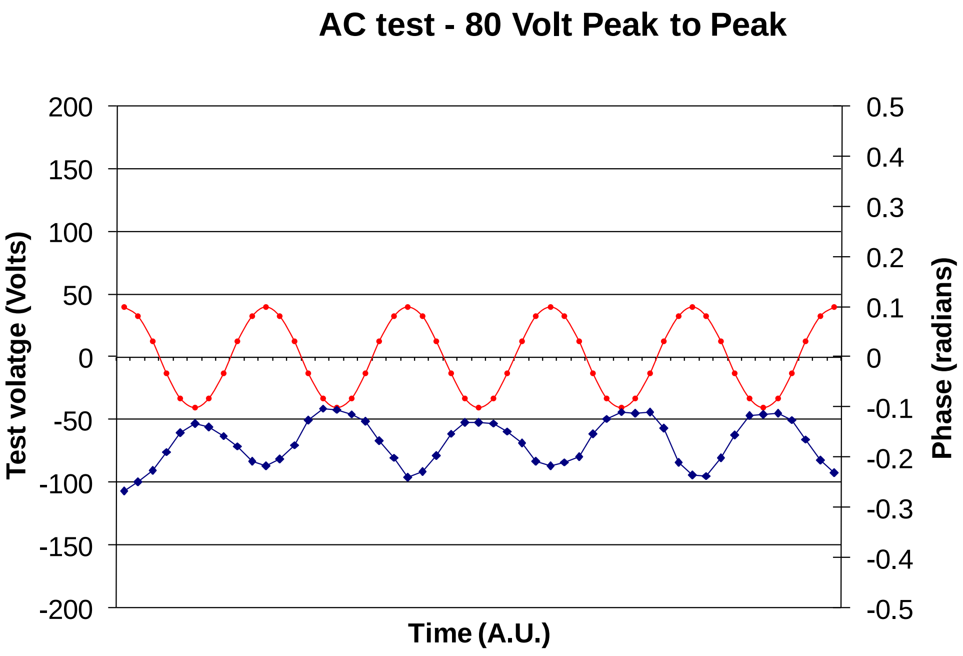

6-3 Five cycle internal electrode AC test – 80 volt peak to peak

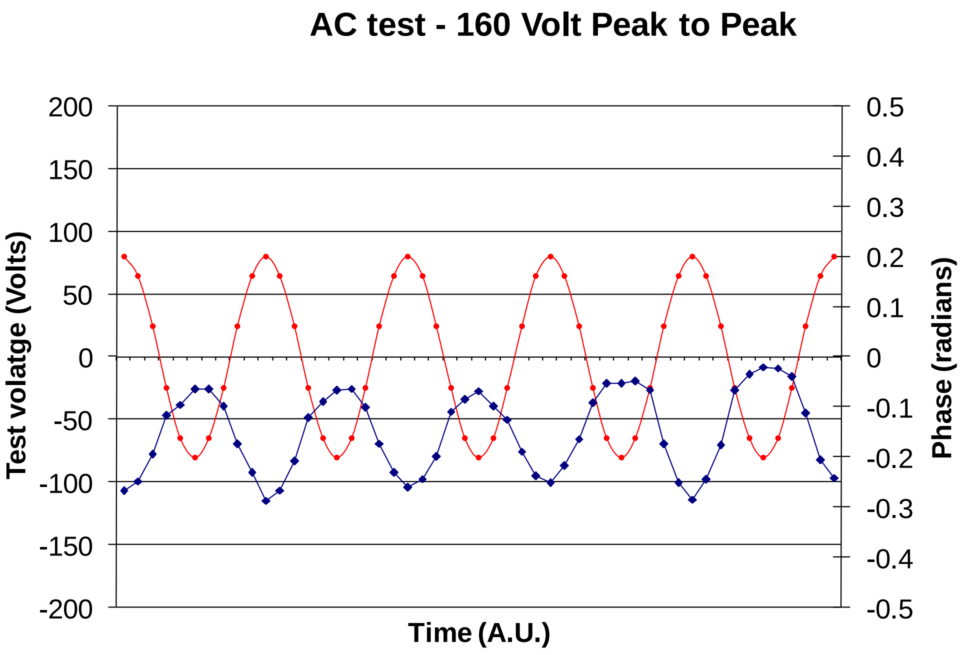

6-4 Five cycle internal electrode AC test – 160 volt peak to peak

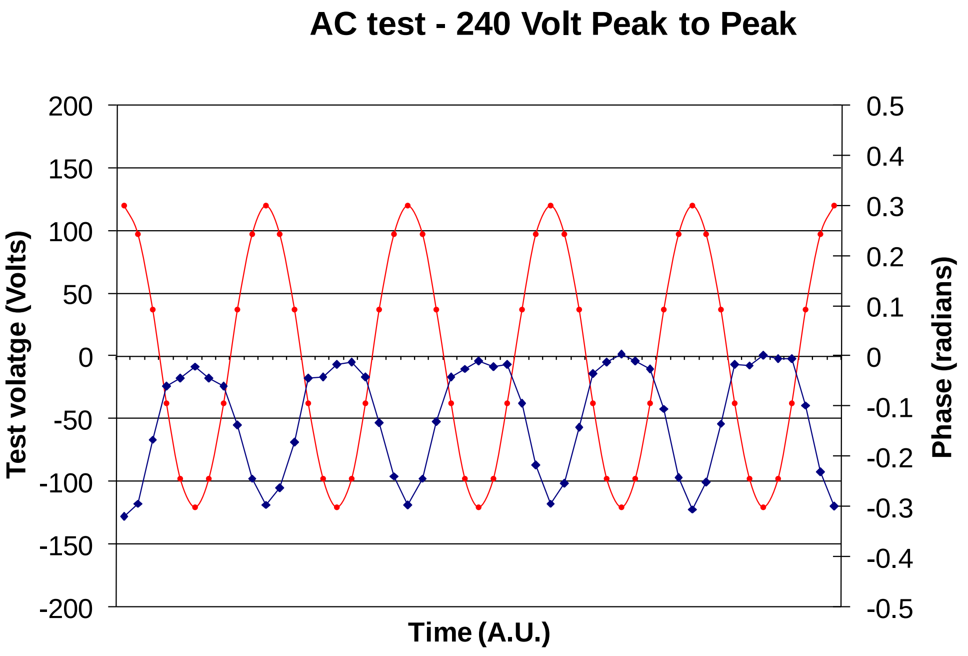

6-5 Five cycle internal electrode AC test – 240 volt peak to peak

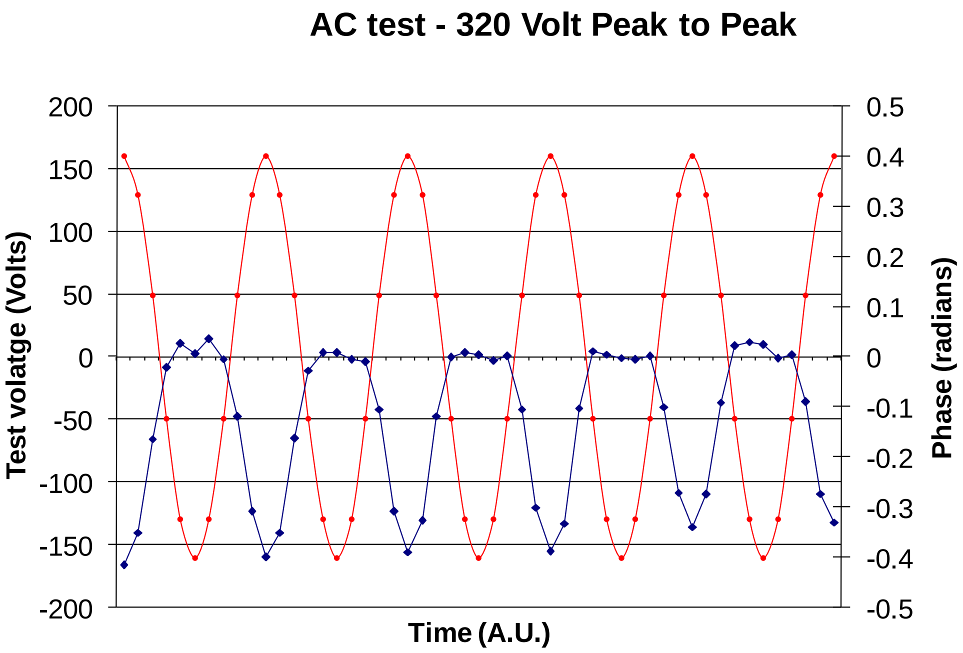

6-6 Five cycle internal electrode AC test – 320 volt peak to peak

The results shown in figures 6-2, 6-3 and 6-4 (at 20V, 80V and 160V peak to peak respectively) show a clear response at the frequency of the probe voltage. Some slower DC drifts are also present since the total time required to collect and process the five complete cycles is a few minutes. Drifts on this time scale are likely to be negligible when making measurements at 50-60 Hz. The results shown in figures 6-5, 6-6 (at 240V and 320V peak to peak respectively) again show a response at the applied test frequency; however some saturation can be seen in the response at large negative applied voltages. The origins of the saturation effect are likely to come from two main sources. Firstly, large negative test fields are effectively cancelling the frozen in field created after poling and minimising the linear electro-optic response of the sensing fibre. This is in agreement with earlier results observed for positive poling [18, 54].

And secondly, an effective second harmonic is generated in the probe electric field by the electrode movement inside the holes. If the electrodes are free to move when the test field is applied then this will appear as a distortion from the ideal sinusoidal test field, due to the change in the effective electrode separation distance.

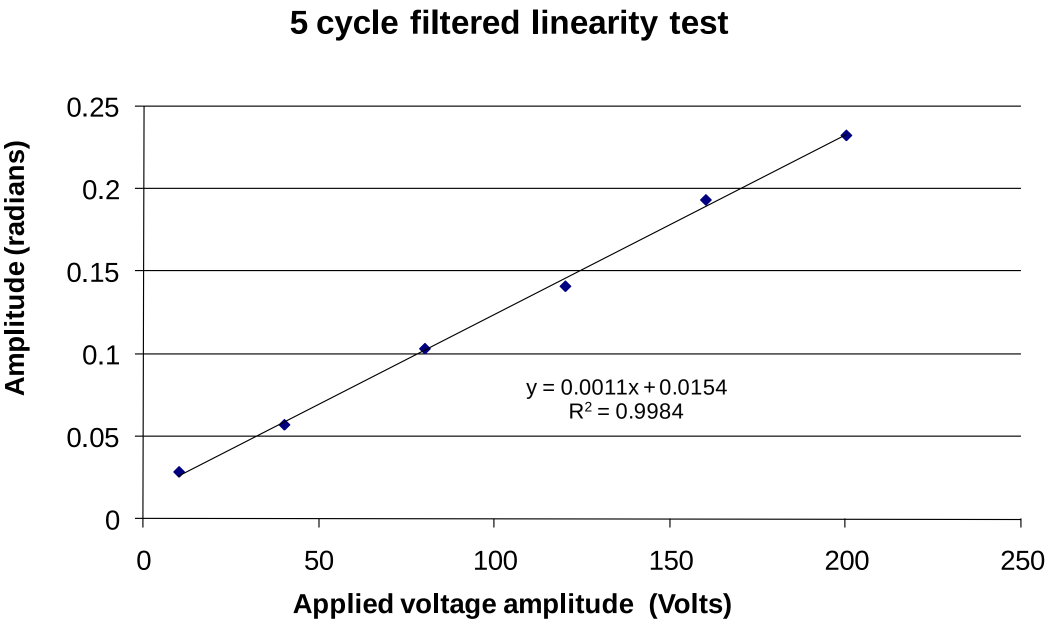

6-7 Five cycle internal electrode AC test – response linearity

The data was then further processed to retrieve the amplitude of the response of the interferogram's phase at the applied frequency. This filtered out both the slow DC drifts seen at the lower test amplitude range and the second harmonic response seen in the higher test amplitude range. Figure 6-7 shows that the filtered response is now quite linear over the test amplitude range from 10 Volts peak to 200 Volts peak. This strong linear response means if the polarity of the applied voltage is reversed then phase, or retardance, change is also reversed. This suggests that the linear electro-optic effect is significantly greater in this experiment than stress-optic effects created by the wires pushing on the core region as the voltage is applied, since charged electrodes will attract regardless of the polarity of the applied voltage. Electrostrictive refractive index changes may also be present as suggested by Godbout et al [55]. However, both the stress-optic and electrostrictive effects may have contributed to the observed second harmonic response mentioned above [56].

6.4 Conclusion

The work presented in this chapter was, at the time the experiments were conducted, aimed at demonstrating that the proposed interferometer and signal processing system was suitable as the basis for a voltage sensor system. In the results presented above the phase of the periodic modulation imposed on the broadband spectrum of the EDF-ASE source responded linearly to the applied probe voltage. The phase response was also stable with only slow drifts that can easily be filtered out in order to realise an AC voltage sensing system functioning at 50 or 60Hz. In summary these results demonstrate the system's potential as a basis for a full-scale voltage sensor with the potential for field deployment in the high voltage transmission and distribution industry. The remaining challenges are in realising high speed acquisition and processing of the interferograms and in packaging the coiled lengths of poled silica sensing fibre required to measure external fields arising in high voltage transmission and distribution applications. These challenges are largely addressed in the subsequent chapters.

Chapter 7. Generation 2 of the voltage sensing and signal processing system

7.1 Introduction

A voltage sensor system capable of accurately measuring the operating voltage in electricity transmission and distribution networks must also be capable of sampling the voltage at an effective sampling rate that is high enough to satisfy the needs of the network control system. For systems operating at 50 or 60 Hz Nyquist's theorem requires a minimum sampling rate of 100 or 120 samples per second (sps) to prevent aliasing. However effective transmission network control requires the measurement of transients and higher frequency harmonics, demanding a higher sampling rate. Commercial digital systems for measuring current at high voltage (instrument transformers) have operated at 1000, and 2000 sps. Recently a new international standard for digital interfacing of instrument transformers has emerged known as IEC-61850. The IEC-61850 standard has categories that require sampling at 4000 and 4800 sps for systems operating at 50 and 60Hz respectively. To address this issue a commercially available high speed spectrometer was incorporated into the signal processing system that allowed the effective sampling rate to be significantly improved. A description of this system, known as generation 2, and voltage sensor test results are presented in this chapter.

7.2 Generation 2 voltage sensing system design

Again a Michelson two polarisation interferometer (M-TPI) using thermally poled twin-hole silica fibre as the sensing fibre was constructed. The optical spectrum analyser was replaced with the high speed spectrometer supplied by Spectral Products

Pty Ltd known as the SM-820. The spectrometer design was based on a Czerny-Turner monochromator and a schematic of the internal construction is shown below in figure 7-1. The SM-820 used a Sony silicon charge coupled device (Si-CCD) as the detector array. The internal optics is arranged so that the light entering the spectrometer illuminates a large area of the diffraction grating to improve the resolving power of the spectrometer. The first diffracted order is then focussed by a mirror onto the detector array. Since the diffraction angle is a function of wavelength each detector in the array is illuminated with a different wavelength. The Si-CCD contained 2048 detectors (or pixels) and the data was clocked out in a serial fashion into a computer (PC) where the output spectrum was reconstructed. The reconstructed spectrum could then be processed using the method presented in the previous chapters i.e. monitor the phase of the periodic modulation seen in the interferograms.

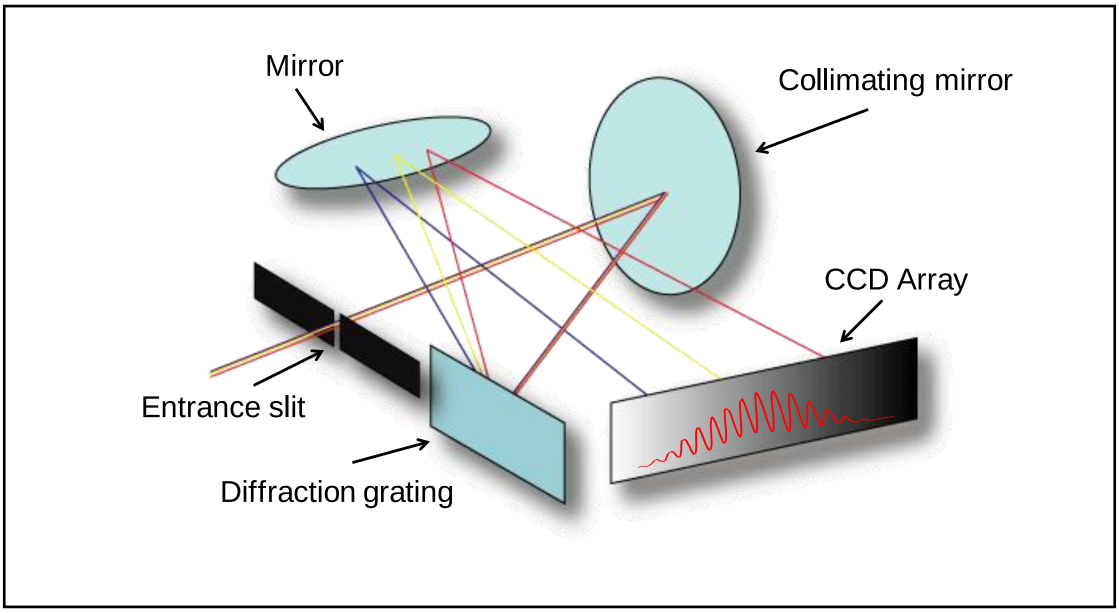

7-1 Czerny-Turner monochromators or compact spectrometer

The basic design of the Czerny-Turner monochromators, or compact spectrometer, appeared to be ideal for the voltage sensor application. The average periodicity seen in the typical interferogram shown in figure 7-2 was approximately 5nm. Wavelength resolution of approximately 1nm was readily achievable with the compact spectrometer by careful adjustment of the entrance slit.

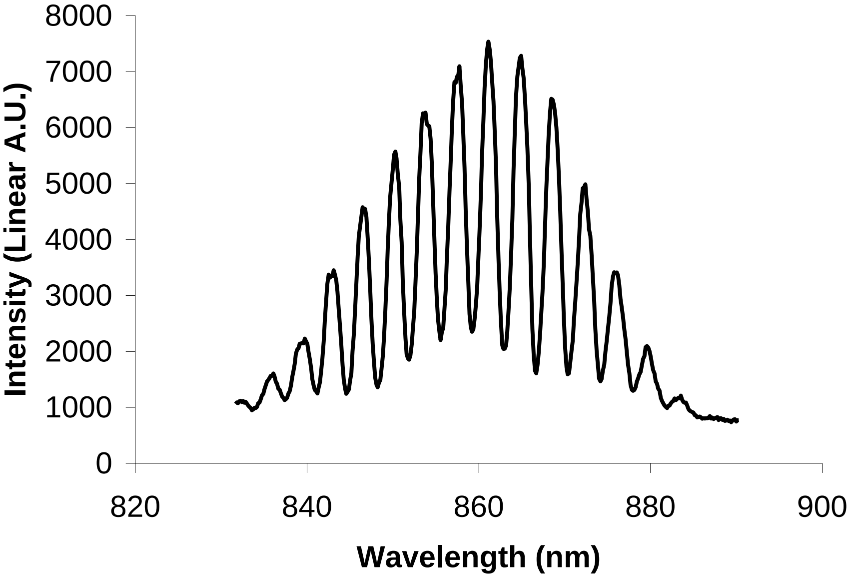

7-2 A typical interferogram operating in the 820 – 900nm band

The challenge in incorporating the compact spectrometer into the signal processing system was in acquiring the data at a sufficiently high rate and at a definite spacing in time. The spectral products SM-820 with its standard interface electronics and software provided a minimum integration time of 2ms. Using the standard interface there was a small delay between recordings of two spectra. The SM-820 PC interface was based on USB 1.0 and the time delay was variable and typically about 20ms. To overcome this problem a custom made PC interface was developed. The SM-820 optics and Si-CCD were retained and the custom interface gathered data from the Sony Si-CCD at a rate of either 500 or 1000 scans per second. A picture of the compact spectrometer and custom interface board is shown in figure 7-3 below. To stabilise the compact spectrometer system the input fibre launching optics and the compact spectrometer were securely mounted onto a heavy steel plate. Fine adjustment that allowed the detected power and wavelength resolution to be optimised was achieved using a precision xyz positioning stage and a collimating lens. The FC-PC type input fibre connector was made using special fibre (Fibercore SM800) that was single mode at the operating wavelength i.e. 820-900nm.

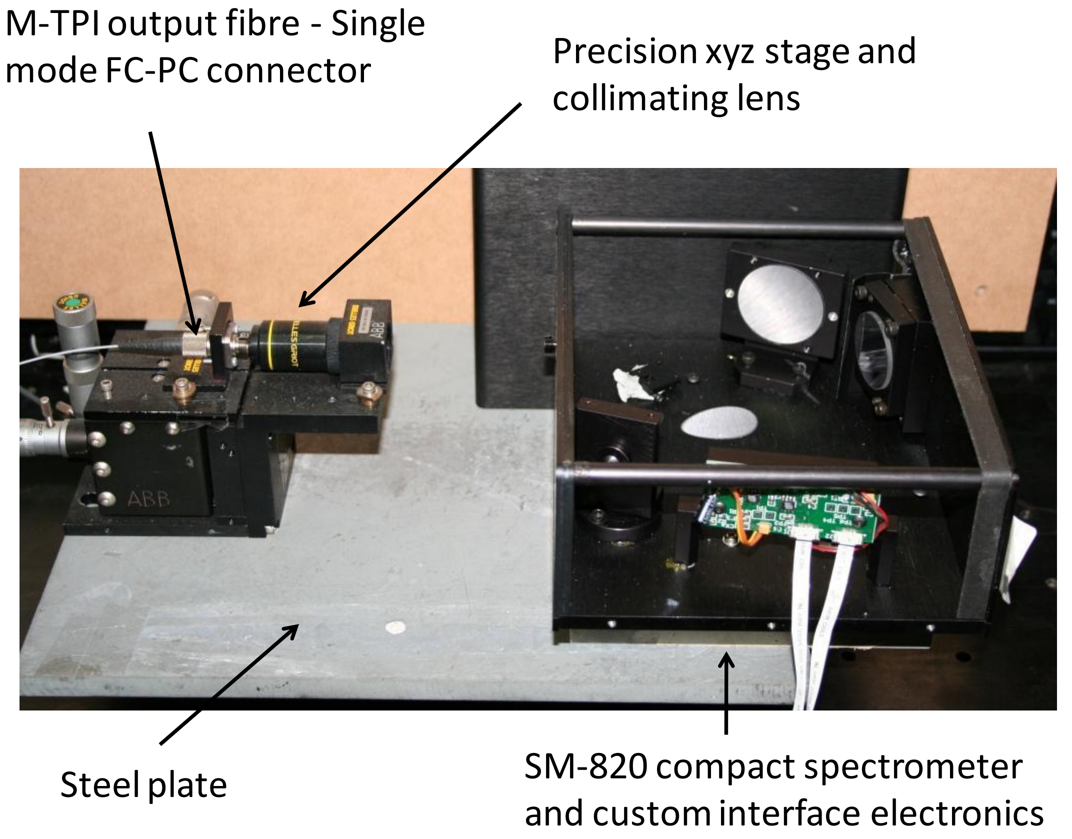

7-3 The Spectral Products SM-820 compact spectrometer and custom interface board

7.3 Generation 2 operating wavelength

The twin-hole fibre developed for the experiments presented in chapters 4 and 6 operated around 1550nm. The Sony ILX-511 Si-CCD effectively operates in the range 400-1000nm and required the development of a new twin-hole fibre that was single mode at the operating wavelength. A target operating wavelength of 820-900nm was chosen due to the availability of suitable light sources such as super-luminescent diodes (SLDs), special fibres, and components and the acceptable sensitivity of the Si-CCD in that wavelength range. Figure 7-4 below is taken from the data sheet for the Sony ILX-511 Si-CCD and shows the relative sensitivity versus wavelength. The relative sensitivity at the operating wavelength can be improved using anti-reflecting (AR) coatings.

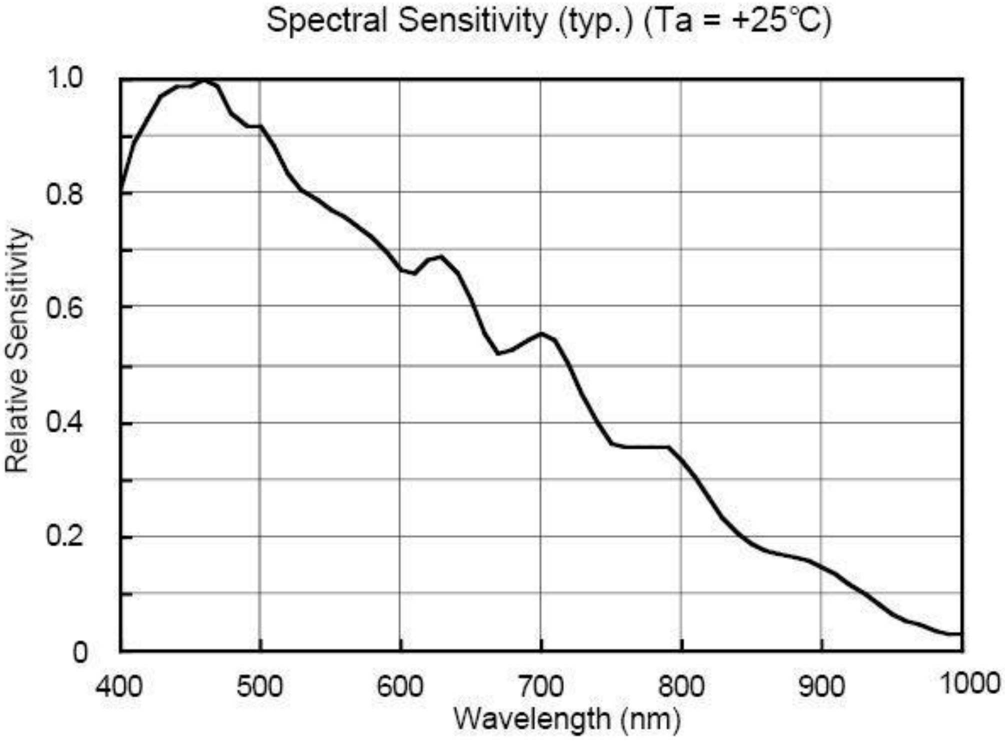

7-4 Sony ILX-511 relative sensitivity versus wavelength

7.4 Generation 2 twin-hole fibre

A single mode (at 820nm) twin-hole fibre known as OD-0133-03B was fabricated at the OFTC and a cross section is shown if figure 7-5 below. The external diameter was approximately 250µm and the two electrode holes were approximately 70-75 µm in diameter. The adjacent edges of the holes were separated by 28 µm and the edge of the core was placed only 3 µm away from the hole containing the positive poling electrode wire. The poling electrode wires were 50 µm diameter clean tungsten wire, supplied by Goodfellow in the UK, and they were inserted by side polishing the fibre to expose the holes.

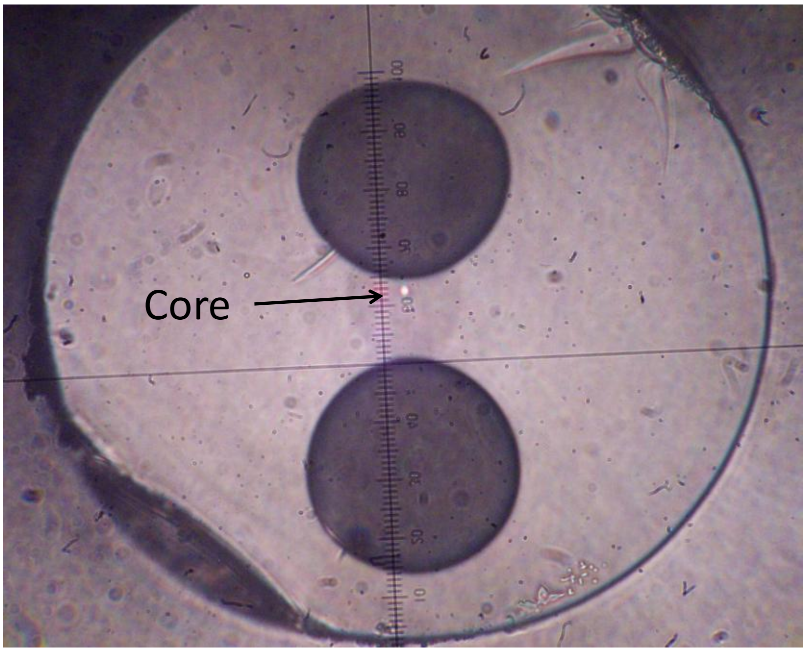

7-5 OD-0133-03B fibre cross section

Thermal poling OD-0133-03B at 300 deg C with 3.5kV DC for 20 minutes applied across the internal electrodes typically produced linear electro-optic coefficients after poling of approximately 0.06pm/V. Again this value was determined a few weeks after poling to allow any fast decay processes to pass.

7.5 Generation 2 signal processing implementation

A schematic diagram of the generation 2 signal processing system is shown in figure 7-6 below. The schematic diagram shows both interface electronics, and a digital signal processing board. The interface electronics acted as an electronic preamplifier for the analogue output from the Si-CCD array. The digital signal processing board, supplied by Smart Digital Optics Pty Limited, contained the high speed A/D converter and the necessary processing power to calculate the phase of the periodic modulation seen in the interferograms. The resulting calculated phase values were then transmitted to the PC via an Ethernet based connection.

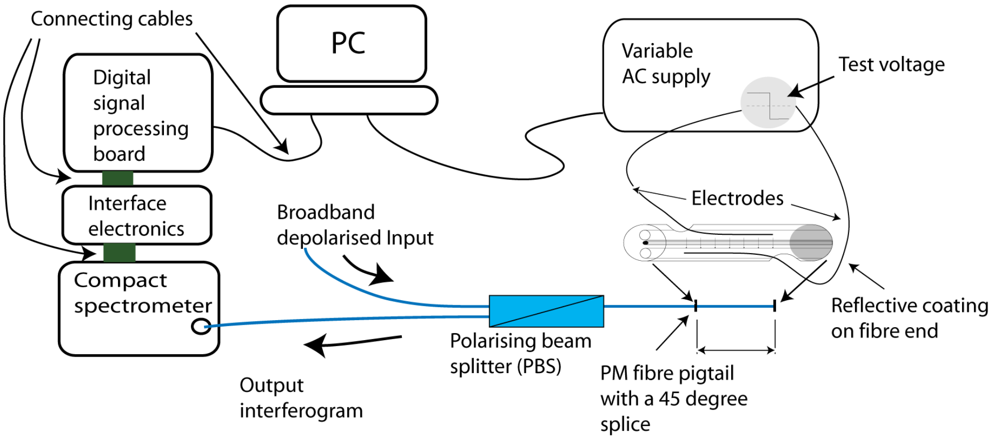

7-6 Schematic diagram of generation 2 of the signal processing system

7-7 The Smart Digital Optics Pty Limited digital signal processing board

7.6 Experiments

After completing the development and troubleshooting of the generation 2 signal processing system the following experiments were performed to characterise the voltage sensing system.

Firstly the signal processing system was optimised by applying test voltages across the internal electrode wires. This provided a good signal to noise ratio that allowed for the system linearity and noise floor to be characterised. The 50Hz sinusoidal test voltage was monitored with a National Instruments (NI) A/D converter card housed in the same PC running the NI Labview code that monitors the phase of the periodic modulation seen in the interferograms. The Labview code also calculated the RMS test voltage and the RMS optical measured voltage averaged over 1 second.

Secondly the electrode wires were removed and the sensing fibre placed between two parallel plate electrodes. This was the first test with an externally applied electric field.

And finally a new sensing fibre was coiled around a cylindrical former and electric fields were applied across plate electrodes placed at each end of the cylinder.

(a) The internal electrode test

A sample of OD-0133-03B was prepared with a polarisation maintaining (PM) pigtail and tungsten electrodes were inserted, by side polishing, with approximately 31 cm of overlap. The sample was then thermally poled over the electrode overlap region at 300 deg C with 3.5kV DC for 20 minutes. This poled device was then configured using the M-TPI and the generation 2 signal processing system discussed above.

Interferograms were collected at a rate of 500 complete spectra per second and the phase of the periodic modulation was also calculated at the same rate allowing electric field measurements up to 250Hz. To determine the response of the sensing system at the frequency of the applied electric field, i.e. 50Hz, the RMS amplitude of the variation of the calculated phase at the applied frequency was calculated. This was calculated by averaging over 1 second blocks of the raw phase data. The RMS optically measured voltage was calculated from the RMS phase values in radians and then scaled by making the average recorded conventional and optical values, at approximately 75V RMS, equal. The test voltage was then varied in steps and the logged data is shown in figure 7-8 below.

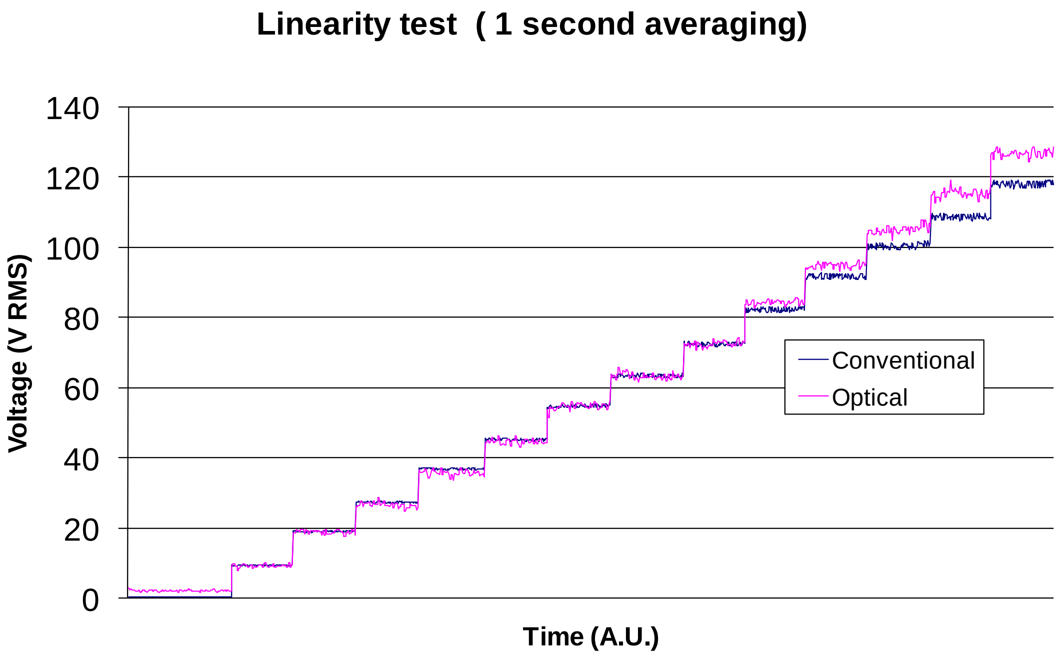

7-8 Generation 2 logged output.

It can be seen that as the test voltage increases so does the optically measured voltage. However there is a slight departure from linearity as the test voltage increases beyond about 75 V RMS. The linearity of the response and the small departure beyond 75 V RMS is better illustrated using an XY plot, by displaying optically measured voltage versus test voltage, as shown in figure 7-9 below.

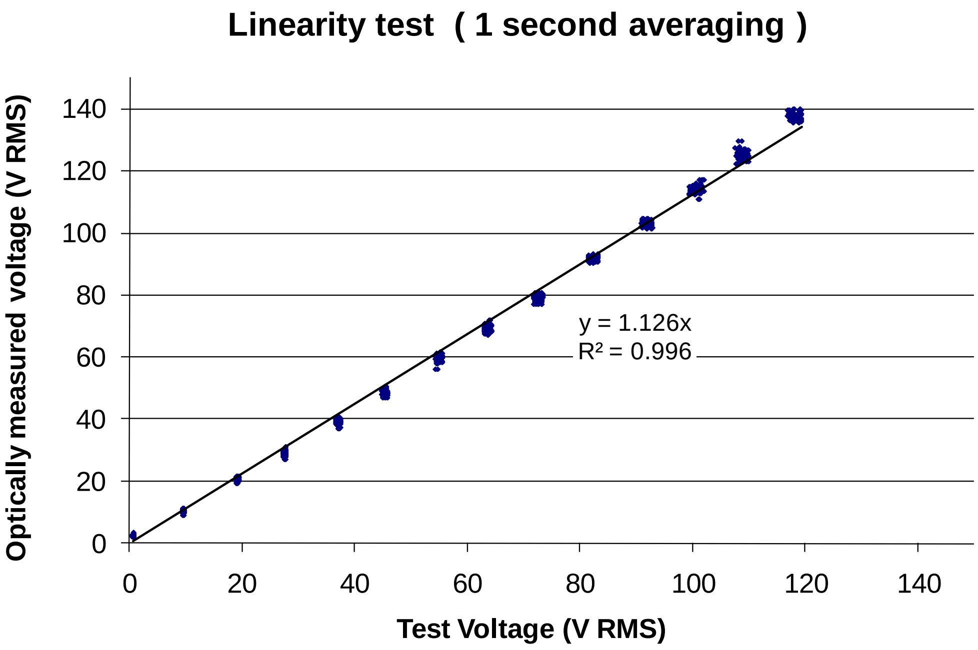

7-9 XY plot :- Optically measured voltage versus Test voltage (V RMS)

The XY plot shows both excellent linearity (R^2=0.996) over the entire test range and the system noise floor with the test voltage switched off. The noise floor can also be seen in figure 7-8 where the first batch of data is recorded with no test voltage and the optical measured voltage appears to be on average around 2 to 2.5 V RMS.

The increase in spread in both the test voltage and the optically measured voltage seen in the higher range is due to the 50 Hz filter and small variations in the supply voltage frequency. The filter centre frequency was 50 Hz and the width was approximately 1Hz FWHM. Although the spread appears to be increasing with increasing voltage the spread is on average a fixed proportion of the test voltage. The filter was applied in the Labview signal processing code and was revised in later generations to approximately 5 Hz FWHM.

The slight departure from linearity at high test current is caused by electrode movement within the holes due to electrostatic force between the wires. The wires will attract regardless of the polarity of the applied test voltage effectively reducing the average separation distance between the electrodes. The higher the test voltage, the greater the reduction in the average separation distance.

(b) The parallel plate electrode test

After removing the electrode wires the same sample of poled silica tested above was placed between two parallel plate electrodes. Each electrode was insulated with a thin layer of polyester tape and insulating paper spacer layers were placed either side of the fibre to insulate the fibre from any mechanical pressure caused by electrostatic forces between the electrode plates (see figure 7.10). The 31 cm poled section was covered by the electrode plates and the plates were separated by approximately 0.5 mm. Care was taken to ensure that the fibre was orientated so that the electric field between the electrode plates was aligned in the poling direction, since this orientation corresponds to maximum sensitivity. A 50Hz sinusoidal voltage was applied across the parallel plate electrodes using a variable transformer. Again generation 2 of the signal processing system monitored both the applied voltage and the phase of the periodic modulation seen in the interferograms. Since the spacing between the electrodes was fixed by the thin insulating layers and the paper spacer layers, it was assumed that the electric field seen by the core was linearly proportional to the voltage applied across the electrodes.

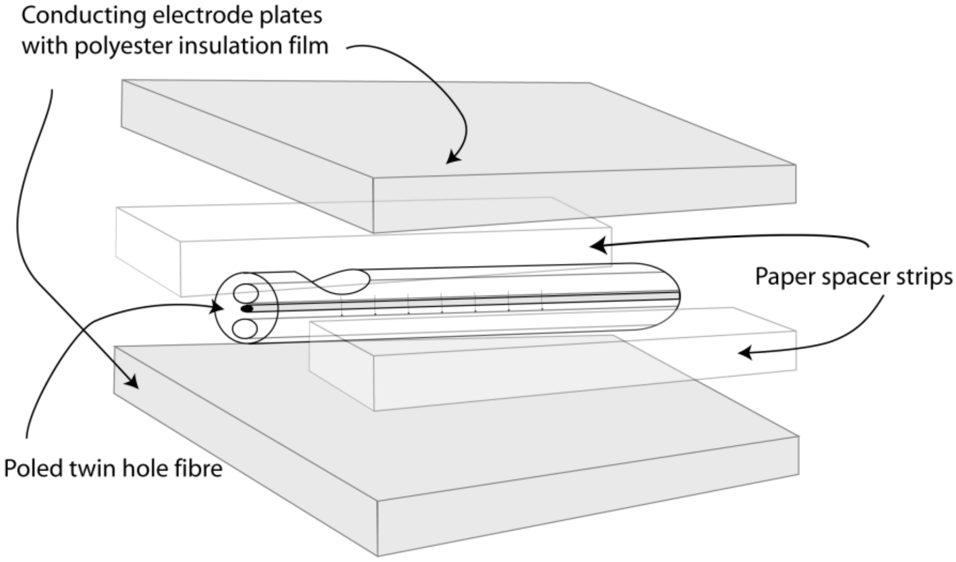

7-10 Illustration of the parallel plate electrode, external field test

Again, interferograms were collected at a rate of 500 complete spectra per second. The response of the sensing system at 50Hz was calculated and averaged over 1 second blocks of the raw phase data. These 1 second values were then averaged over approximately 2 minute intervals and the results are presented in figure 7-11. The error bars in figure 7-11 are set at +/- 1 standard deviation. The sensing system was calibrated so that the response in radians was converted to an optically measured voltage by calculating a scaling factor from the measured phase response at the maximum test voltage of 240V rms. To simplify the analysis, the optically measured voltage, versus the applied test voltage is presented.

The generation 2 sensing system response presented in Figure 7-11 clearly shows good linearity for test voltages above 50 V RMS. A noise floor of approximately 30V RMS is evident and the linearity below 50V RMS is affected by the reduced signal to noise ratio.

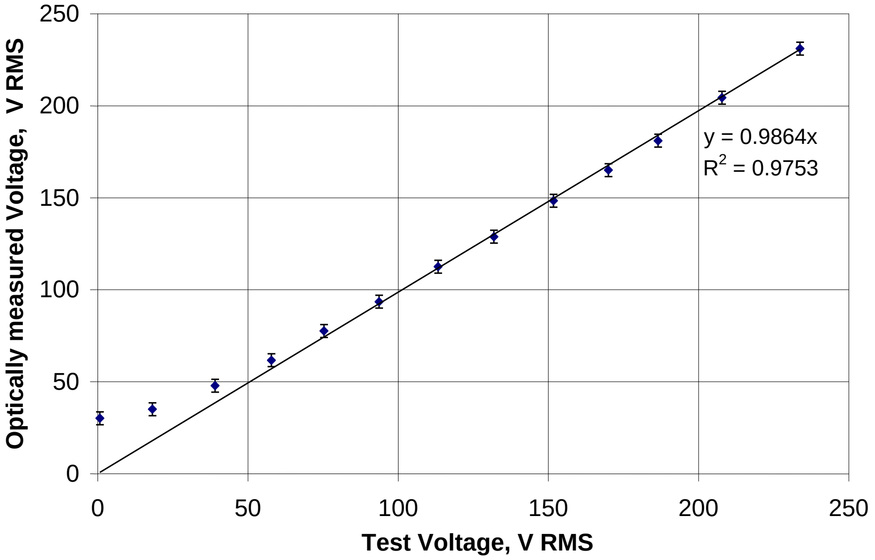

7-11 The parallel plate configuration sensing system response at 50Hz

An average electric field between the parallel plate electrodes can be calculated from the applied test voltage. The average electric field at the maximum test voltage amplitude was approximately 460 kV/m RMS. The noise floor seen in figure 7-11 corresponds to an average electric field of 60 kV/m RMS. The 50Hz filtering algorithm used in these experiments had a relatively broad bandwidth of approximately 25Hz. This corresponds to a noise floor of 12 kV/m√Hz. However the background noise spectrum is unlikely to be flat around 50Hz and using a narrower

50Hz filter may not provide the improvements typically expected when filtering out sources of white noise.

(c) Coiled fibre lab sensor configuration

In chapter 2 section 2.9 (a) the use of helically coiled poled silica fibre as the basis for a voltage sensor was introduced and a ghost view illustration of such a voltage sensor is shown in figure 7-12 below. A new fibre made from the same preform as OD-0133-03B known as OD-0133D has been developed where careful design of the fibre cross section has resulted in a preferred bending orientation when the fibre is coiled. In addition to the two longitudinal holes required for the insertion of electrode wires, there is a symmetry breaking flat. The flat was designed to ensure that when the fibre is coiled around a cylinder it will automatically align itself with the flat on the inside of the helix. A cross section of the coiled fibre cleaved close to the surface of the cylinder is shown in figure 7-13 below. The image shows a misalignment angle of the flat relative to the surface of the cylinder. Cleaving the fibre at multiple points confirmed the misalignment was consistent at each point. A more detailed discussion of the cause and cure of the consistent misalignment can be found in chapter 8.

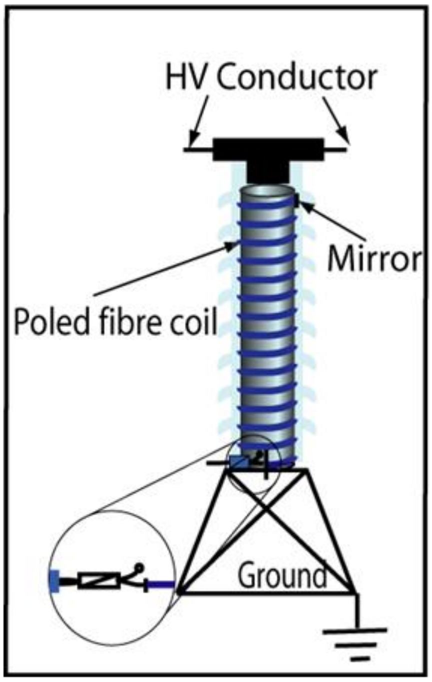

7-12 Ghost view illustration of a field deployable voltage sensor showing the coiled poled silica fibre

A sample of OD-0133D was prepared and thermally poled with 1.5m of electrode overlap at 300^0C and 3.5kV DC poling for 30 minutes. Due to the 1.5 m length of the electrode overlap the sample was poled progressively by shifting the heater every 30 minutes. The electro-optic response of the fibre was characterised using a Mach Zehnder interferometer (MZI) and the average electro-optic response a few days after poling was 0.16 +/-0.015 pm/V. As discussed in chapter 4 typically a ratio of approximately 1.17:1 for the polarisation dependence of the electro-optic response has been observed for thermally poled fibres of this type.

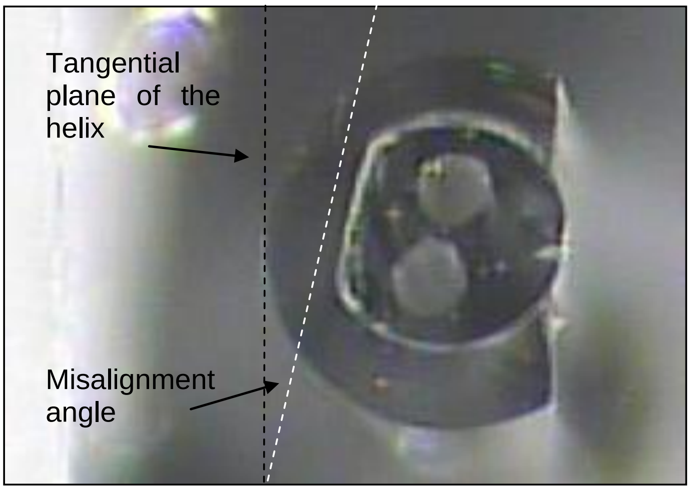

7-13 OD-0133D cross section

The orientation of the fibre flat was then checked, using a microscope, at both ends of the 1.5 metre sample and the fibre was then coiled around a 150mm diameter standard fibre spool. This provided around three full turns of fibre with a constant pitch from one flange to the other. External plate electrodes were then placed on both flanges and the coiled sensor was placed inside a custom built high voltage test enclosure capable of testing up to 40kV/m RMS at 50 Hz. A calibrated magnetic voltage transformer was used both to generate and monitor the high voltage using a low voltage input. The low voltage input was monitored by the generation 2 signal processing system that again was used to calculate the optically measured voltage from the sensor.

The sensor was then exposed to 50 Hz test voltages in the range 0-4.7kV RMS in approximately 250V RMS increments.

The same basic methods were used to determine the test voltage for the coiled sensor, however in this case an improved version of the signal processing system was used. The operating principle was identical with the only practical differences being that the sampling rate was increased to 1000 spectral scans per second and timing jitter and electronic noise were greatly improved. The bandwidth of the 50 Hz filter was also reduced to 5Hz FWHM and this resulted in improved signal to noise ratio and the results averaged over 10 seconds are presented in figure 7-14.

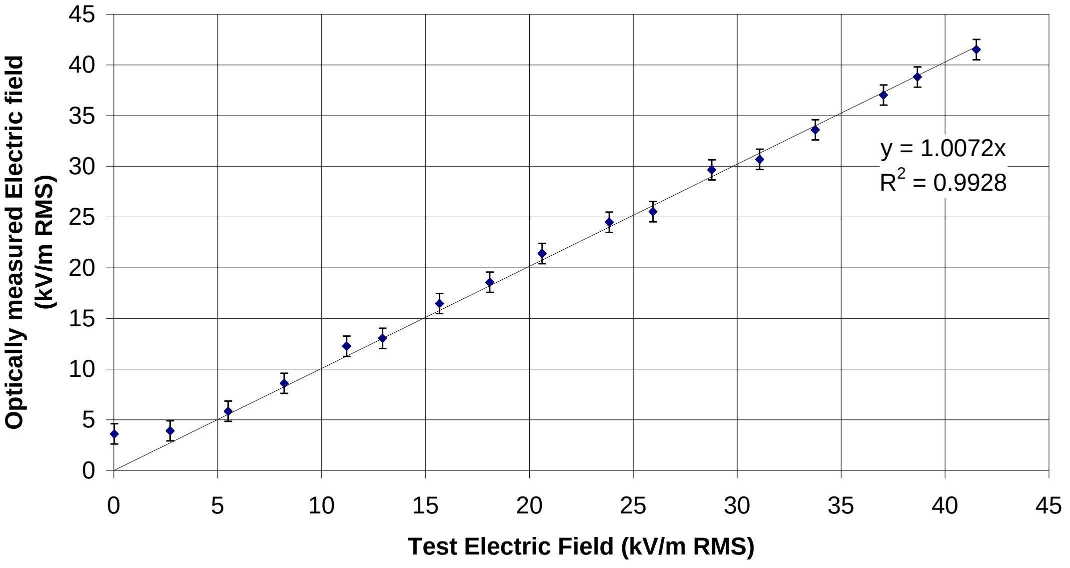

7-14 coiled fibre configuration sensing system response at 50Hz

The test voltage has been converted to an average electric field simply by dividing the test voltage by the 115mm electrode separation. This resulted in an electric field test range of approximately 0 – 40 kV/m RMS and the results are presented in figure 7-14. The sensing system response clearly shows good linearity for test voltages above approximately 6.0 kV/m RMS. A noise floor of approx 3.5 kV/m RMS is evident and the linearity below 6.0 kV/m RMS is affected by the reduced signal to noise ratio.

Conventional voltage transformers for high voltage transmission lines typically measure average electric fields in operation of 50 - 100kV/m. The results presented in figure 7-14 show excellent linearity between 6.0 – 40.0 kV/m RMS. Fortunately little variation in line voltage is present in typical high voltage transmission lines since variations in power transmission requirements are taken care of by varying the transmission line current. As a result the dynamic range requirement for a voltage transformer is greatly reduced compared with a current transformer.

7.7 Conclusion

Sensing of electric fields and voltage have been demonstrated using thermally poled silica fibre and operating at 50Hz using both internally and externally applied electric fields. Above the noise floor a linear response was observed for tests using externally applied electric fields where the effective electrode separation distance was independent of the test voltage. The tests using internally applied electric fields provided better signal to noise performance; however at high test voltage the response became non-linear due to changes in the effective electrode separation distance. The noise floor in the coiled sensor configuration is approximately 3.5 kV/m RMS and considering the filter bandwidth of approximately 5Hz gives a noise floor of 1.5 kV/m RMS√Hz. The improvement compared with the parallel plate configuration is due to a number of factors including the increased length of poled silica and the improved signal processing. This allowed the averaging time to be reduced from 2 minutes to 10 seconds between the parallel plate and coiled sensor experiments. These results indicate that a full scale voltage sensor for the electricity transmission industry could be realised using the basic principles presented in this thesis. Longer lengths of poled silica fibre may be required if further improvement in signal to noise performance is required.

Chapter 8. Generation 3 of the voltage sensing and signal processing system

8.1 Introduction

The performance of generation 2 presented in chapter 7 was promising with the results indicating that improvements in both sampling rate and noise performance were required. The data acquisition rate of generation 2 was limited by the Sony Si-CCD. The Si-CCD array contained 2080 pixels with 2048 active pixels and the maximum rate at which the data from each pixel could be clocked out was 2Mhz. This limited the maximum spectral scan rate to just less than 1000 scans per second (or more precisely 2,000,000 pixels per second / 2,080 pixels per scan ≅ 962 scans per second). The emergence of InGaAs detector arrays from manufacturers such as Goodrich, allowed for the development of a high speed compact spectrometer operating in the 1550nm range. Choosing an InGaAs detector array containing 512 pixels and a maximum pixel clock rate of 2.5 MHz allowed for the development of a high speed compact spectrometer capable of approximately 5000 scans per second (or 2,500,000/512 ≅ 4883 scans per second). This would allow the voltage to be sampled at the same rate, satisfying the requirements of the new digital instrument transformer interface standard IEC-61850.

8.2 Generation 3 voltage sensing system design

The centre operating wavelength of generation 3 was 1550nm and required the development of both a new 1550nm version of the compact spectrometer and interfacing electronics and a twin-hole fibre suitable for thermal poling that is single mode at 1550nm. The interferometer and signal processing system were essentially identical in design with the exceptions that all the optical fibres and components had to be single mode at 1550nm and the signal processing now needed to process a smaller batch of pixels per scan (512 versus 2048 pixels) at a higher rate. The schematic diagram of generation 3 is identical to that presented for generation 2 and is shown in figure 8-1 below.

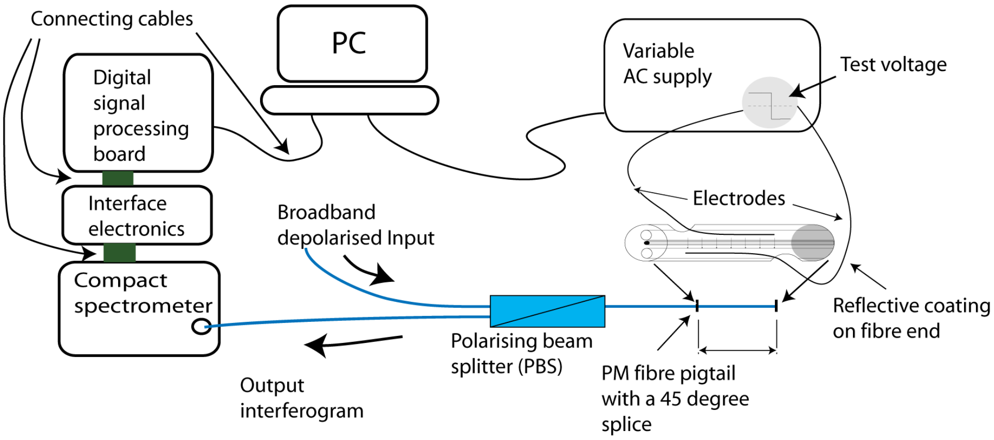

8-1 Schematic diagram of generation 2 of the signal processing system

An Oriel compact spectrometer provided by Newport was chosen since it was configurable to the user's requirements. Diffraction gratings, entrance slits and detector arrays could be selected by the user to optimise the spectral resolution, spectral span, and centre operating wavelength. A picture of the Oriel compact spectrometer is shown below in figure 8-2.

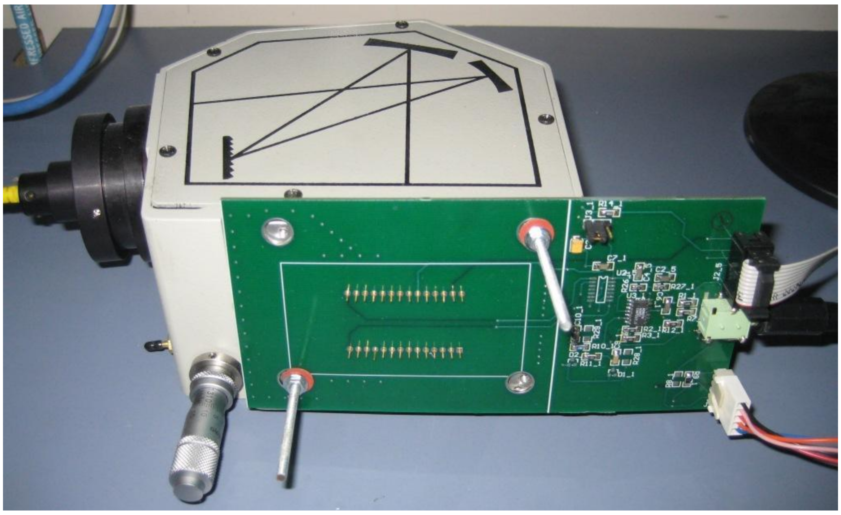

8-2 Oriel compact spectrometer and interface electronics

The custom built interface electronics board contained the Goodrich 512 detector InGaAs array and the electronic preamplifier needed to buffer the output from the detector array. The spectral data was processed, using the same Smart Digital Optics signal processing board used in generation 2, to calculate the phase of the periodic modulation seen in the interferograms.

8.3 Interferometer wavelength sensitivity

The linear-electro-optic response of the poled fibre is wavelength dependent and this is discussed in more detail in chapter 5. The experimentally determined variation over the wavelength range from 820nm to 1550nm is approximately 100% (see figure 5.13). The sensitivity of the proposed low coherence interferometer is also expected to have strong wavelength dependence since the induced phase change $\Delta\phi$ in equation (3.4) $\Delta\phi = {}^{4\pi\Delta n(E)L}/_{\lambda_0}$ is inversely proportional to wavelength. As a result by approximately doubling the operating wavelength from 820nm to 1550nm the sensitivity is expected to halve. This sensitivity penalty is expected to be compensated for by improved signal to noise performance of the 1550nm system. The availability of very high power (in excess of 10mW) broad-band depolarised light sources such as super-luminescent diodes (SLDs) and erbium doped fibre – spontaneous emission sources (EDF-ASE) combined with the low losses of 1550nm fibre and components will contribute to improved signal to noise.

8.4 Generation 3 twin-hole fibre

A single mode at 1550nm twin-hole fibre known as OD-0265-FN was fabricated at the OFTC and a cross section is shown in figure 8-3 below. The fibre was designed to have improved automatic alignment properties compared with the single flat fibre presented in chapter 7. The preferential bending orientation of the new fibre was enhanced by incorporating two flats into the design and the holes were placed symmetrically on either side of the core (double flat fibre).

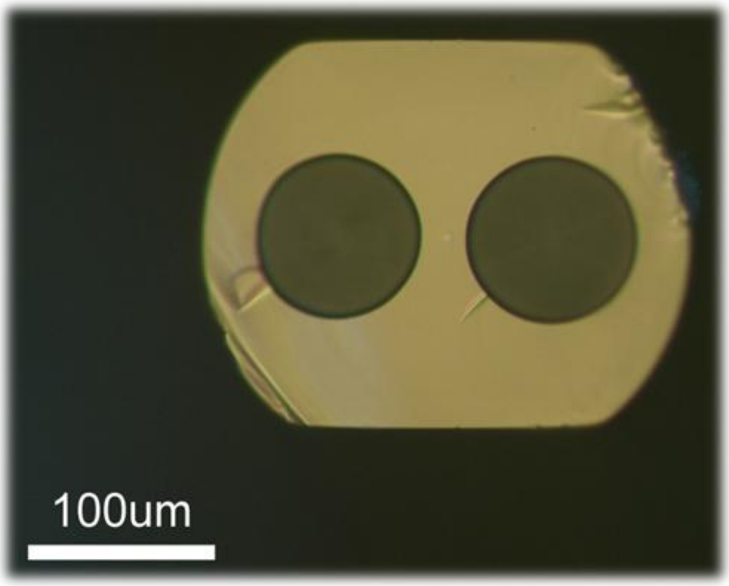

8-3 OD-0265-FN fibre cross section

OD-0265-FN was intentionally made as symmetrical as possible particularly in regard to the shape, size, and position of the electrode holes. The slight misalignment of the coiled single flat fibre presented in chapter 7 was believed to be due to the preferential bending orientation of the asymmetric holes competing with the preferential bending orientation of the single flat.

The fibre was drawn at 3 different sizes and wound on to fibre spools. The external diameter (looking in the plane of the holes) for each fibre was approximately 230, 250, and 280µm for the 3 different spools. Figure 8-3 shows a sample of the 230 µm fibre. The core is placed approximately in the centre between the two holes. The core is not visible in the image as the cleaved fibre was illuminated from above.

8.5 Helical coiling the double flat fibre

Helically coiling the double flat fibre will cause the fibre to automatically align itself with the holes positioned as shown in figure 8-4. This will result in maximum alignment of the poling direction with the local tangential surface plane of the helix. A small misalignment due to the winding pitch is unavoidable. This problem is reduced if the winding pitch is reduced. Winding trials using the double flat fibre prior to poling showed excellent automatic alignment properties (see the picture inset in figure 8-4.

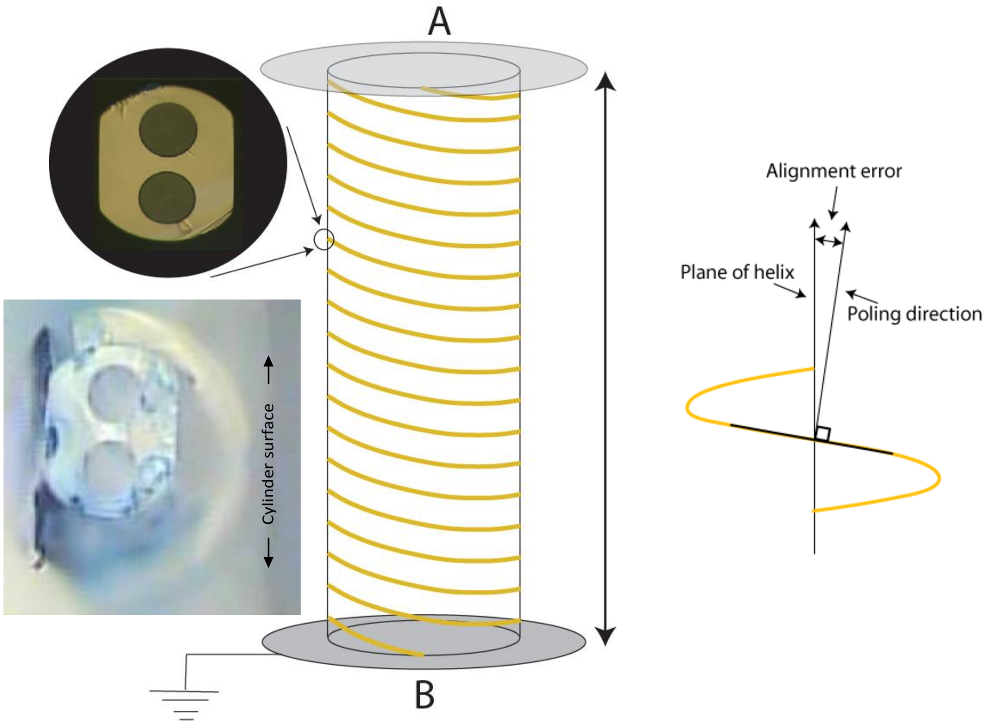

8-4 Double flat fibre coiling illustration

8.6 Experiments

The generation 3 signal processing system was characterised using the same three separate voltage sensor arrangements as presented in chapter 7 i.e. by applying test voltages across the internal electrodes, the parallel plate electrodes and finally as a coiled voltage sensor. The coiled sensor was packaged into a 36kV porcelain insulator and tested up to approximately 20kV RMS at 50 Hz.

In addition the high speed real time data acquisition and processing of generation 3 allowed for a demonstration of the capture of transients. Examples showing test voltages being switching on and off are shown in figures 8-10 – 8-13, demonstrating the system capability.

(a) **Results using a sample of OD-0265-FN @ 230µm diameter**

A sample of OD-0265-FN @ 230µm diameter was prepared with a PM pigtail spliced at 45 degrees and electrodes inserted with approximately 1.35m of overlap. The 50 µm diameter tungsten wires, supplied by Luma Metals AB (Sweden), were inserted

by side polishing the fibre to expose the holes. The wires were inserted from the same end to maximise electrode overlap. After side polishing and inserting the first electrode, the fibre was turned over. To prevent the electrodes from being too close together at the entry points, where the only insulation is the air gap, a new hole was side polished approximately 5 cm away from the initial hole. This allowed for thermal poling at 3.5kV DC and 300 deg C for 20 minutes without electrical breakdown.
After thermal poling a residual linear electro-optic coefficient of approximately 0.2 pm/V was measured using a Mach-Zehnder interferometer operating at 1550nm.

The poled device was then configured as a voltage sensor using the Michelson two polarisation interferometer (M-TPI), as has been used in the preceding generations 1 and 2. Test voltages at 50Hz when then applied across the internal electrodes. The response in radians, at 50 Hz, was then recorded by the signal processing and the results are presented in figure 8-5 below. The pink diamonds represent data averaged over 200 ms (or 10 cycles @ 50 Hz) corresponding to a bandwidth of approximately 5Hz. The black diamonds represent the average of 20 consecutive 200ms samples and effectively correspond to 4 seconds of averaging.

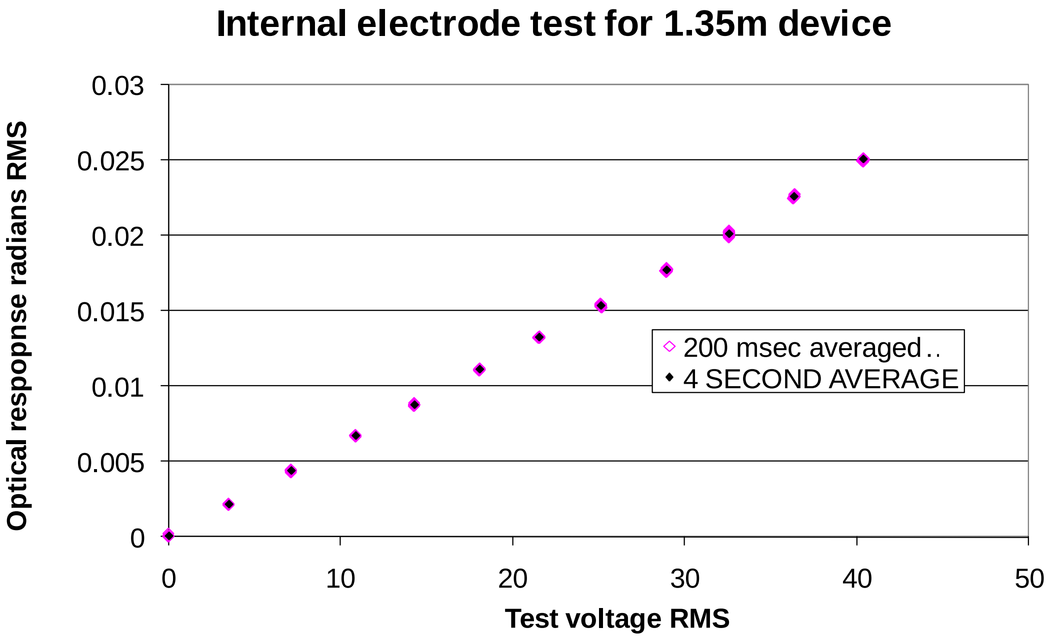

8-5 Internal electrode test for 1.35 m device

The linearity is excellent using both the 200ms and 4 s averaging. The noise floor is very low and cannot be seen in figure 8-5. Switching the test voltage off and recording the response at 50Hz using the 200ms averaging gave a noise floor of 50µrad or approximately 22µrad/√Hz. If a coarse calibration is made where the optical response in radians with a test voltage of 42 V RMS @ 50 Hz is scaled to give an optical response of 42 V RMS, then the noise floor for the optically measured voltage is $42\text{V RMS}\times\frac{0.05\text{mrad}}{25\text{mrad}}\cong 84\text{m V RMS}$.

The internal electrodes were then removed and the poled fibre placed between two parallel plate electrodes. The fibre was coiled in a flat spiral onto the lower electrode plate to take advantage of the automatic alignment properties of the double flat fibre and also to prevent the electrode plates from becoming too long, as the poled section alone was now 1.35m in length. A fixed thickness spacer (2mm) was then placed on the lower electrode and the upper electrode was placed on top of the spacer.

Test voltages at 50Hz were then applied across the electrode plates and the results are presented below.

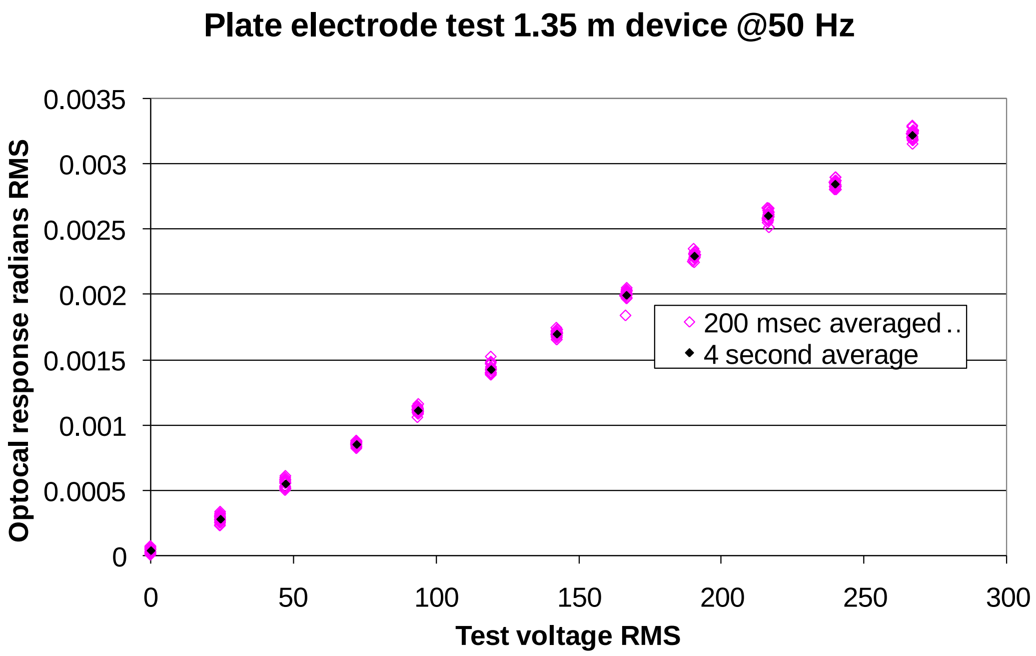

8-6 Plate electrode test for 1.35 m device

Linearity is still excellent using both 200ms and 4s averaging with an apparent small increase in spread for the 20 consecutive 200ms samples. The noise floor in radians is unchanged from the previous experiment; it is simply the magnitude of the electric fields that is reduced. Using the internal electrodes the optical response at 42V RMS is approximately 25mrad RMS and with 270V RMS applied across the parallel plates the optical response is approximately 3.2mrad RMS. Making a coarse calibration using the same method used above results in a noise floor for the optically measured response of $270\text{V RMS}\times\frac{0.05\text{mrad}}{3.2\text{mrad}}=4.2\text{V RMS}$ for the parallel plate electrode configuration.

The same poled fibre was then coiled around a cylindrical former made from insulation grade paper tube known as a press board tube. The tube was 500mm long and 95mm in diameter and designed to fit snugly inside a 36kV porcelain insulator. End electrode plates were then fitted that held the press board tubing in place and also provided an electrical connection for the high voltage tests. An example photo of the coiled fibre on a press board tube is shown in figure 8-7 below.

8-7 Left: Press board tubing and coiled double flat fibre, Right: Porcelain insulator and end electrode plates.

The coiled sensor was then placed inside the high voltage test enclosure described in chapter 7 above and shown below in figure 8-8. Test voltages were applied across the external electrode plates in approximately 1-2 kV RMS steps from 0 – 17kV RMS and the results are presented in figure 8-9 below.

8-8 Left: Magnetic voltage transformer used to both generate and monitor the test voltage, Right: A coiled sensor being tested without the porcelain insulator.

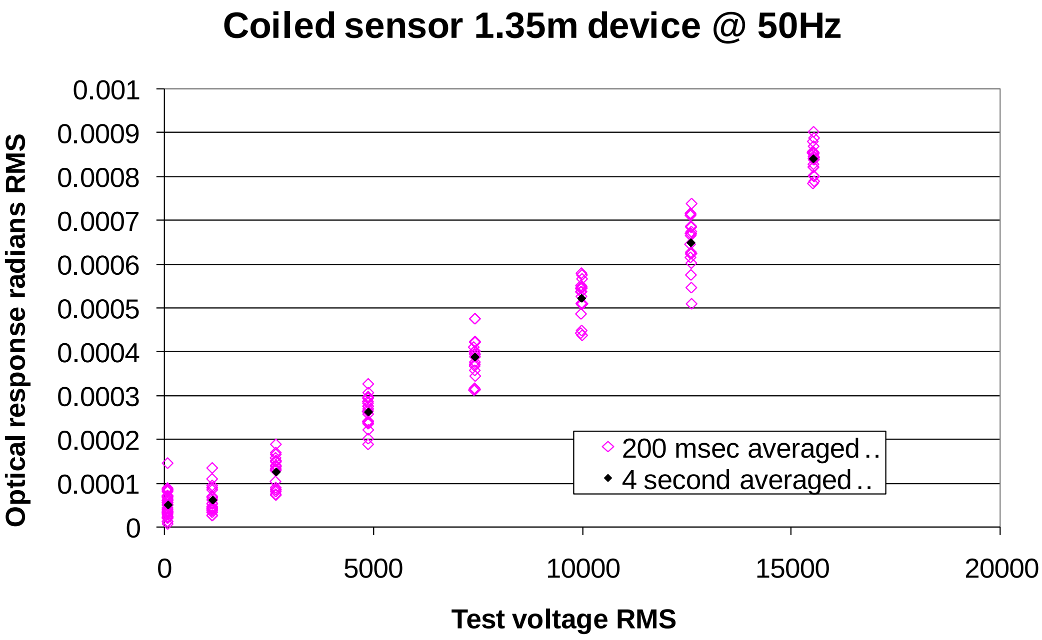

8-9 Coiled sensor test for 1.35 m device

Linearity of the response can still be seen using both 200ms and 4s averaging with an apparent large increase in spread for the 20 consecutive 200ms samples. Again, the average noise floor in radians is unchanged from the previous experiment, and the magnitude of the electric field has been further reduced. In the coiled sensor the optically measured response at 17kV RMS was 0.85μrad giving a noise floor of $17\text{kV RMS}\times\frac{0.05\text{mrad}}{0.85\text{mrad}}=690\text{V RMS}$ for the parallel plate electrode configuration.

(b) **Results using a sample of OD-0265-FN @ 250μm diameter**

A poled sample of the 250 μm fibre was prepared using the same methods presented above. Approximately 2m of electrode overlap was achieved and the poled sample was again configured as an M-TPI and connected to the generation 3 signal processing system. Improvements in the signal processing between the tests on the 230 μm fibre and tests on the 250 μm fibre resulted in better real time data acquisition and data logging functionality and allowed for the simulation of transient recording. Transients are of great interest for network control as they are used to detect system faults such as short circuits and form part of a system known as “protection”. Instrument transformers used in protection systems are required to have enhanced dynamic range and response time but with reduced demands on accuracy. As a demonstration of transient recording capability test voltages were switched on and off during 1 second of data logging and the results are shown in figures 8-10 and 8-11 below.

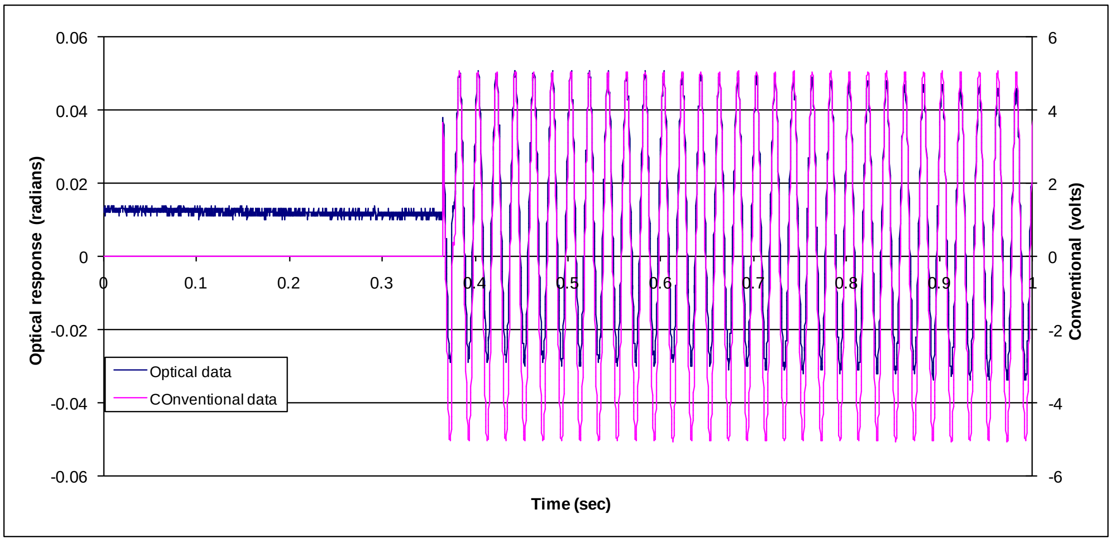

8-10 Transient recording – test voltage switched on

The effective sampling rate, for generation 3, is approximately 5000 sps and figure 8-10 shows all 5000 raw samples collected over a second of both the test voltage and the optical response in radians. The data is plotted against time. The slight DC offset seen in the optical response is due to the slow drift in the interferometer.

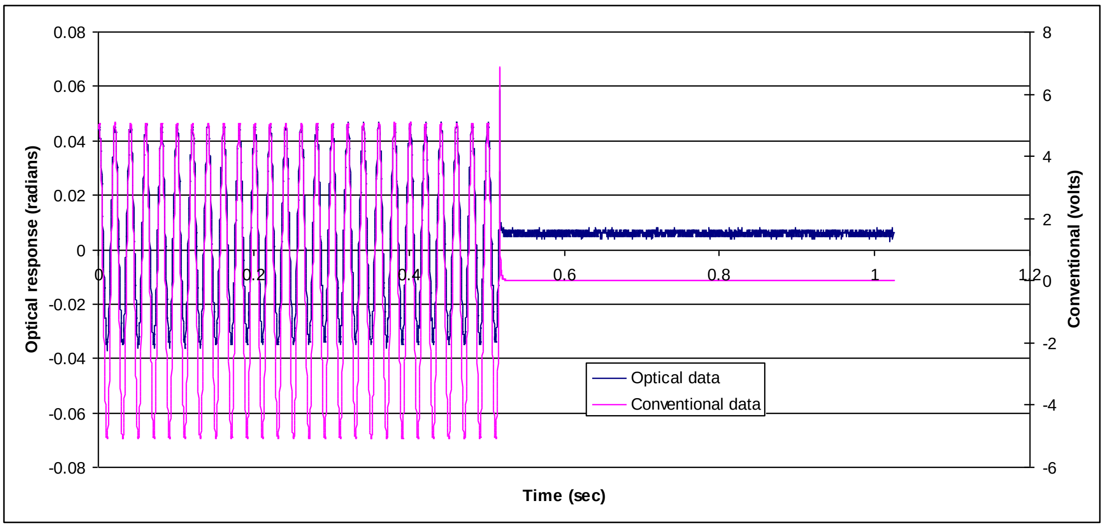

8-11 Transient recording – test voltage switched off

Zooming in around the switching time in both cases clearly shows the optical response is tracking the test voltage, indicating qualitatively that the bandwidth of the system is only limited by the sampling rate i.e 5000sps giving a maximum bandwidth of 2.5kHz. During the switch on transient, switch bounce can be seen, where a momentary interruption is present during the first cycle after switching. Similarly, during the switch off transient a positive spike can be seen.

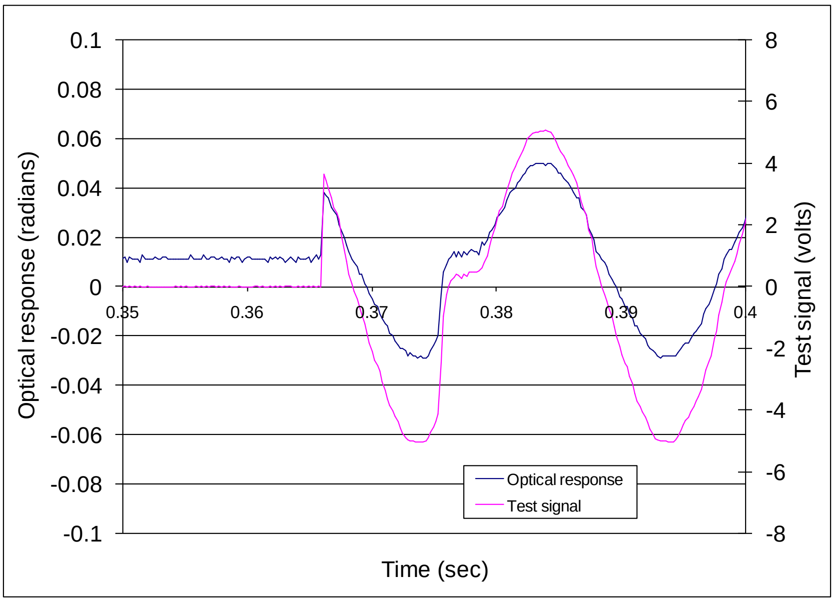

8-12 Transient recording – switch on zoomed in

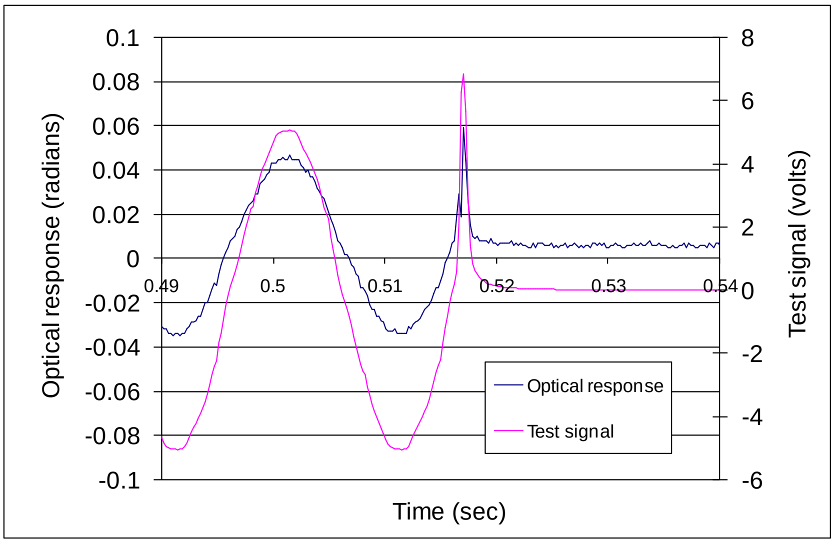

8-13 Transient recording – switch off zoomed in

The 2m sample of the 250 µm fibre was then tested for accuracy by applying test voltages across the internal electrodes. The voltage sensor system amplitude and phase errors were determined for both 1 cycle and 1 second averaging intervals. First a linearity test was performed and the optical versus test voltage was plotted and a calibration constant determined. The RMS optical response versus RMS test voltage at 50 Hz was plotted using both the 1 cycle and 1 second averaging. At each test voltage 20 consecutive samples were recorded and in both cases excellent linearity can be seen. The small increase in spread using 1 cycle averaging can barely be seen in the XY plots.

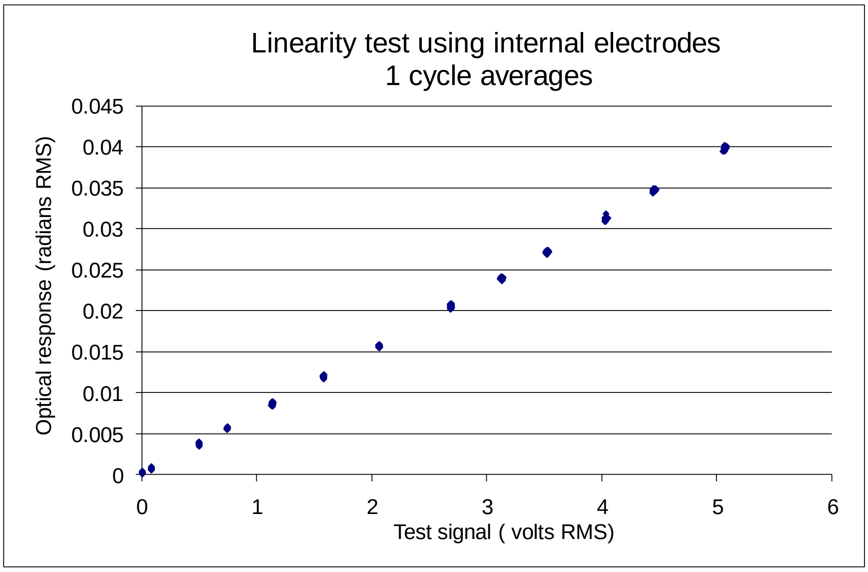

8-14 Linearity test using 1 cycle averaging

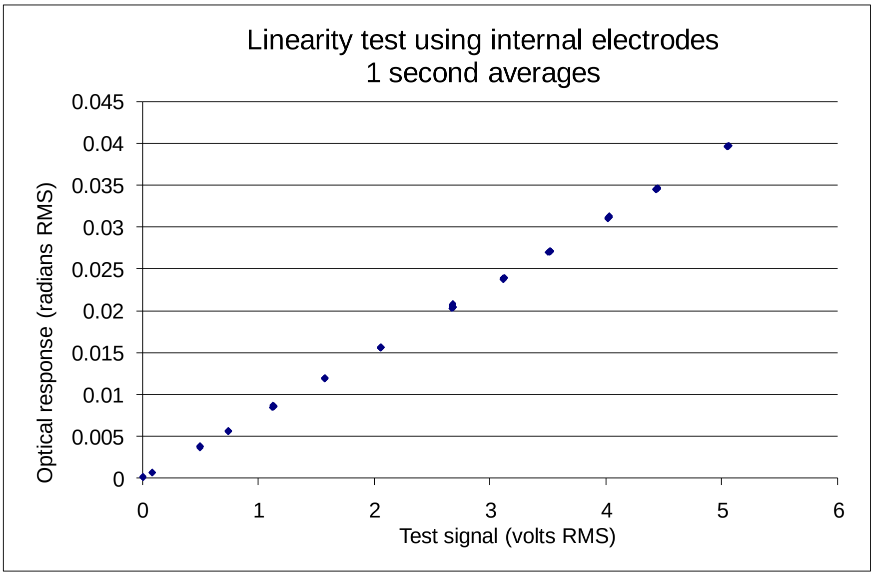

8-15 Linearity test using 1 second averaging

From the linearity tests a calibration constant was determined that converted the optical response in radians to an optically measured voltage. The data was then processed to determine the accuracy of the optically measured voltage versus test voltage. Figure 8-16 shows % amplitude error versus test voltage and figure 8-17 shows the phase error versus test voltage. In both cases the spread increases as the test voltage is reduced due to the reduced signal to noise ratio. The results using 1 cycle averaging also shows increased spread versus the 1 second averaging due to the increased bandwidth of the 50Hz filter. The slight non-linearity in the amplitude accuracy is believed to be due to electrode movement. This is in agreement with the results presented in chapter 7 using generation 2 of the signal processing where a similar response was observed.

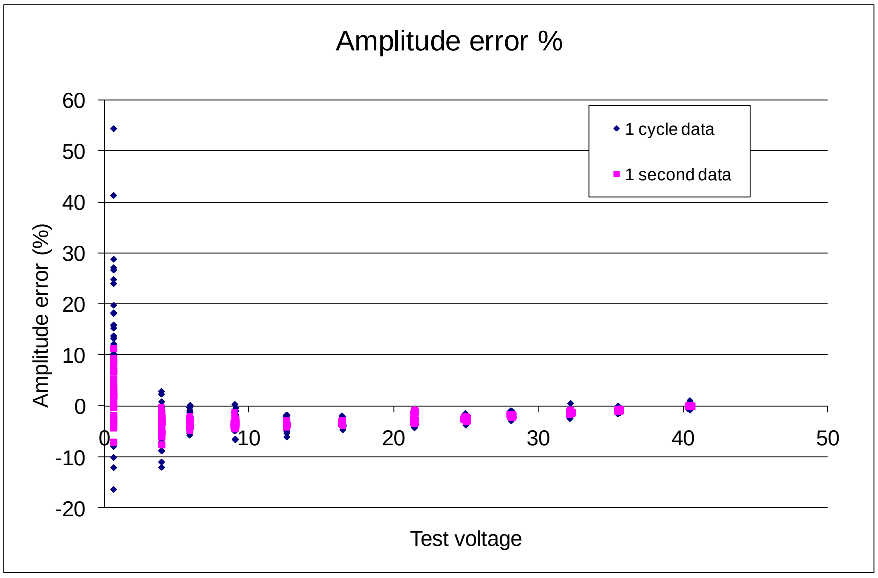

8-16 Accuracy test showing amplitude measurement errors

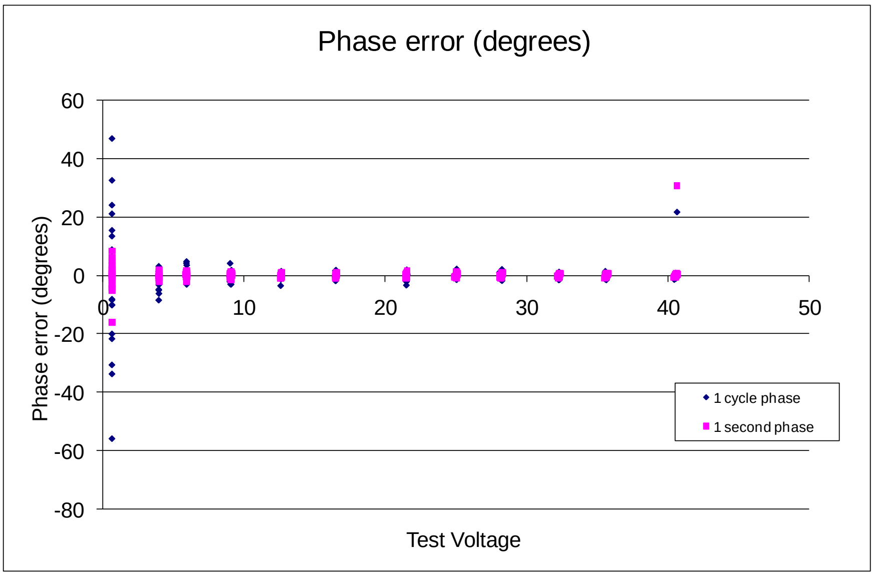

8-17 Accuracy test showing phase measurement errors

Chapter 9. Temperature independent highly birefringent photonic crystal fibre

9.1 Introduction

The topic of birefringence in optical fibre was introduced in section 2.10 above and in this chapter the discussion is extended to include high birefringence (HiBi) in the recently introduced photonic crystal fibre (PCF). Birefringence in highly birefringent photonic crystal fibres (HiBi-PCF) arises mostly from the fibre waveguide geometry i.e. form birefringence, where two-fold rotational asymmetry in the arrangement, position and/or shape of both the holes and the core region causes birefringence [8].

For reference the modal birefringence introduced in chapter 2 above is described in more detail in appendix C. Using the definition presented in appendix C (equation C.1) , i.e. $B_m = \left|n_{eff}^x - n_{eff}^y\right| = \Delta n_{eff}$ where n_{eff}^x and n_{eff}^y are the effective phase (or modal) refractive indices of the x and y polarised modes. Significant form birefringence i.e $B_m \geq 10^{-4}$ can be created in PCFs by suitably designing the fibre cross section. Constructing PCFs using a silica host with an array of air holes offers increased refractive index contrast relative to conventional step index HiBi fibres further contributing to greater flexibility in design. In PCFs, guidance properties are determined by the interaction of the modes with the core region and the surrounding rings of holes, and it is to be expected that the wavelength dependence of many properties of these fibres is different from that found in conventional stress birefringence fibres. This has lead to the development of polarising HiBi-PCFs where single polarisation operation over a very large wavelength range has been demonstrated [57, 58].

9.2 Temperature dependence in HiBi fibres

(a) **Bow-tie and Panda fibre**

Two main designs of stress birefringence fibres have gained broad acceptance and they are known as bow-tie and Panda fibres. The fibre cross section, in both of these designs, includes stress applying parts (SAP), placed in the cladding region on either side of the core [26, 27]. The glass used to make up the bulk of the fibre is based on very high purity silica glass. The core region has a raised index of refraction and this is achieved through doping, typically with germanium. The SAPs found in bow-tie and Panda fibres are typically made of borosilicate glass that has a higher coefficient of thermal expansion than the host material. The fibre is made by drawing down, at high temperature, a fibre preform typically around 10-20mm in diameter to the final fibre diameter of either 80 or 125 µm. When the fibre cools the differential thermal expansion of the host material and the stress applying parts creates large internal stress. Birefringence of $B_m \cong 10^{-4}$ is readily available in both bow-tie and Panda fibre from a number of commercial suppliers.

Since birefringence arises from thermal stresses in bow-tie and Panda fibres their birefringence is highly temperature dependent. HiBi fibres with low temperature dependence would be of significant interest for a number of applications, particularly those involving sensing where temperature variations are in most applications undesirable. For example, temperature effects in the highly stressed conventional HiBi fibre limit the accuracy of fibre optic gyroscopes, as well as current sensors based on spun elliptically polarising optical fibre [59, 60]. PCFs with birefringence comparable to and greater than conventional highly stressed bow-tie and Panda fibre have been demonstrated previously [5, 8, 61].

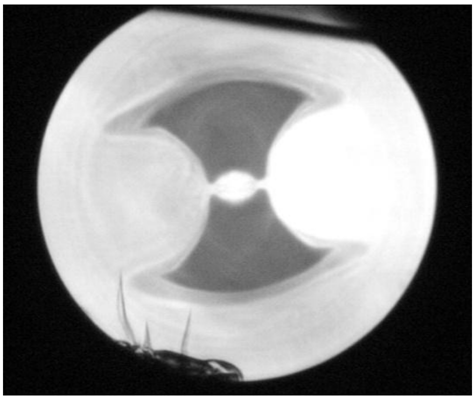

9-1 A bow-tie fibre cross section clearly showing the dark bow-tie shaped borosilicate regions that form the stress applying parts

(b) Highly birefringent photonic crystal fibre

The temperature dependency of the birefringence of fibres based on waveguide geometry promises to be much less than that of stress induced birefringence. The dominant mechanism that has been suggested to contribute to the temperature dependence of the birefringence in HiBi-PCFs is thermo-optic effects in the waveguide material [62]. Silica is an excellent choice as a host material for the fabrication of HiBi-PCFs since for silica the thermo-optic coefficient is *dn/dT* = 1.1×10^{-5}K^{-1}. This is approximately an order of magnitude lower than poly methylmethacrlyate (PMMA) which has a thermo-optic coefficient of *dn/dT* = 1.1×10^{-4}K^{-1}. The thermo-optic coefficient of the air in the holes is negligible, *dn/dT* = 1×10^{-6}K^{-1}.

In this chapter the temperature dependency of the birefringence of a HiBi-PCF is studied. Results are presented over a temperature range from –25 to 800°C, and for comparison, a conventional bow-tie HiBi fibre is studied over the range from –25 to 175°C. In addition a method that allows the modal birefringence B_m to be determined from the experimentally measured group birefringence B_g is introduced using the definitions set out in appendix C.

9.3 *Methods*

(a) Experiments

Figure 8.2 shows the cross-section of the fibre used in this study. The air holes are arranged in a triangular lattice. The average hole diameter is 4.4μm and the pitch

7.4µm. The elliptical shaped fibre core has an approximate dimensional ratio of 2:1 (10.9µm: 5.6µm), with position and geometry of the holes of the innermost ring structure also slightly distorted from a perfect six fold rotationally symmetric structure. The highly birefringent photonic crystal fibre was manufactured by stacking capillaries.

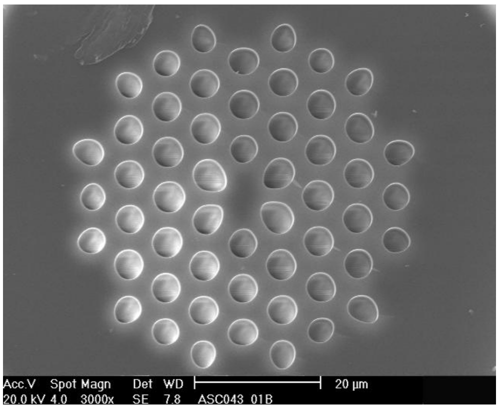

9-2 SEM image of the cross-section of the fibre

The Michelson two polarisation interferometer (M-TPI) introduced in section 3.2 above was constructed with a section of the HiBi-PCF shown above as the sensing fibre or fibre under test. A diagram of the interferometer using HiBi-PCF as the fibre under test is shown in figure 9.3. Both a white light source and an erbium doped fibre – amplified spontaneous emission broadband depolarised (EDF-ASE) light source were used to illuminate the interferometer. A polarisation maintaining fusion splicer was used to perform the 45 degree splice between the polarisation maintaining pigtail of the polarisation beam splitter and the HiBi-PCF under test.

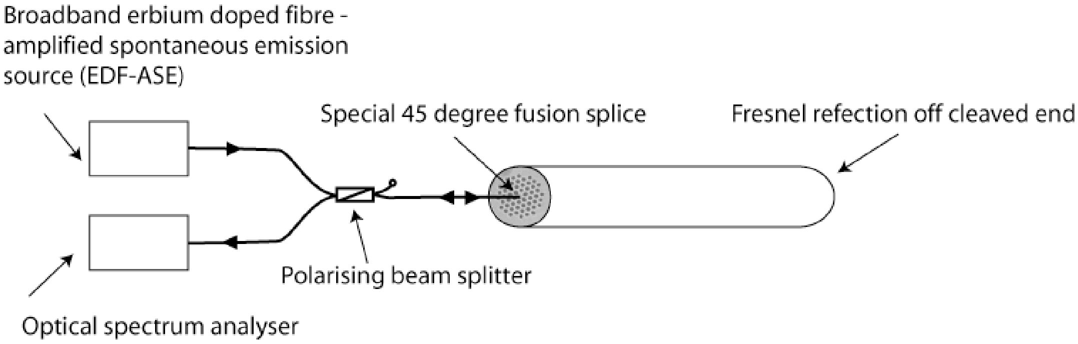

9-3 Experimental set up for measuring group birefringence

The 4% Fresnel reflection from the cleaved end of the HiBi-PCF resulted in a clearly observable output spectrum or interferogram from the interferometer. The interferograms were recorded using an optical spectrum analyser and then stored and processed in a personal computer.

As discussed in sections 3.2 - 3.4 above the observed period of the spectral ripple is a function of the path imbalance between the two polarisation modes arising through birefringence in the sensing section. By heating the sensing fibre and observing the phase and period of the spectral ripple any change in the path imbalance can be detected. The signal processing was automated and determined both the phase and average period of the interferogram by applying a fast Fourier transform.

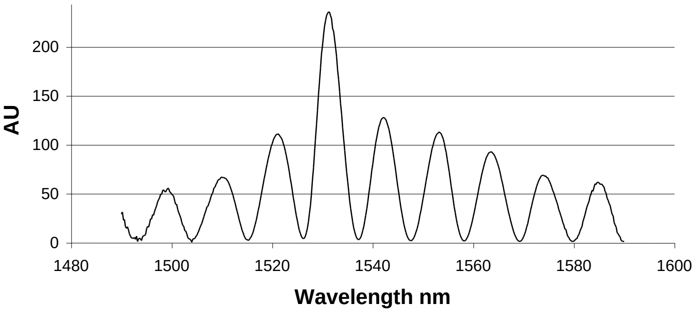

9-4 A typical interferogram as measured on the optical spectrum analyzer.

(b) Group and modal birefringence analysis

The average group birefringence of the test section of a fibre can be determined from the spectral ripple period, $\Delta\lambda$, seen in the interferogram. The method is detailed in the following analysis.

The phase difference between the two polarisation modes after two trips through the sensing section of fibre of length, L is,

$$\phi = {}^{4\pi L B_m(\lambda)}/_{\lambda} \tag{9.1}$$

where $B_m(\lambda)$ is a function of wavelength see appendix C. A single period of the spectral ripple $\Delta\lambda$ obtained from the interferogram corresponds to a 2π phase shift between the two polarisation modes. Differentiating the phase with respect to wavelength and substituting $d\phi = 2\pi$, and $d\lambda \cong \Delta\lambda$ leads to the following relationship between the group birefringence, B_g, and wavelength - see appendix C,

$$\frac{d\phi}{d\lambda} = \frac{2\pi}{\Delta\lambda} = \frac{d^{4\pi L B_m(\lambda)}/_{\lambda}}{d\lambda} = 4\pi L \frac{dB_m(\lambda)}{\lambda d\lambda} - 4\pi L \frac{B_m(\lambda)}{\lambda^2} \tag{9.2}$$

$$= -\frac{4\pi L}{\lambda^2}\left(B_m(\lambda) - \frac{\lambda d B_m(\lambda)}{d\lambda}\right) = -\frac{4\pi L}{\lambda^2} B_g \tag{9.3}$$

rearranging

$$B_g = -\left(\frac{\lambda d B_m(\lambda)}{d\lambda} - B_m(\lambda)\right) = -\frac{\lambda^2}{2L\Delta\lambda} \tag{9.4}$$

The period of the spectral modulation $\Delta\lambda$ combined with the length of the fibre L can then be used to find the group birefringence using (9.4) above.

The modal birefringence $B_m(\lambda)$ is often of more interest as it determines the polarisation holding power of the fibre. Polarisation maintaining properties are important in most sensing and interferometric applications. To calculate the modal birefringence for the HiBi-PCF from the typical interferogram shown in Fig. 9.4, the wavelength dependence of the modal birefringence must be determined. If for example, the modal birefringence increases with wavelength this would have the effect of compressing (or reducing the period) of the spectral ripple seen in the interferogram at the long wavelength end, and stretching (or increasing the period) of the spectral ripple at the short wavelength end. The relationship $B_g = \left(B_m(\lambda) - \frac{\lambda d B_m(\lambda)}{d\lambda}\right)$ implies that evaluating B_g over a broad wavelength range may reveal information regarding the wavelength dependence of $B_m(\lambda)$. The assumption that the wavelength dependence of the birefringence in HiBi-PCFs follows an empirical power law dependence of the form $B_m = \alpha\lambda^k$, where α and k are constants to be determined, is strongly supported in the literature [5, 8, 63]. Substituting this assumption into (9.4) it follows that

$$B_g = -\alpha(k-1)\lambda^k \tag{9.5}$$

As a result, the constants α and k can be determined by plotting group birefringence versus wavelength and numerically fitting a power law function $B_g = -\alpha(k-1)\lambda^k$. The modal birefringence can then be calculated from the group birefringence using

$$B_m = {}^{-B_g}\big/_{(k-1)} = \alpha\lambda^k \tag{9.6}$$

Eq. (9.6) shows that the group and modal birefringence differ not only in magnitude but for typical k values for HiBi-PCFs of between 2 and 3 [5, 8, 63] they are also opposite in sign. Consequently, the fast and slow polarisation axes are interchanged when modal and group are interchanged.

In practice the wavelength dependence of the group birefringence can be determined by dividing the interferogram up into wavelength sections and processing each section as a separate interferogram with a separate centre wavelength. The group birefringence for each section can then be calculated and the resulting data can be processed. This is valid, in the wavelength region covered by the interferogram, provided there is good agreement with the experimental data, i.e. it is a good fit.

Moreover, this is true for any function that is a good fit for the experimental data in the wavelength range examined. An alternative is to use a power series of the form

$$B_m = a_0 + a_1\lambda + a_2\lambda^2 + a_3\lambda^3 + a_4\lambda^4 \ldots \tag{9.7}$$

Evaluating the expression $B_g = \left(B_m(\lambda) - \frac{\lambda d\, B_m(\lambda)}{d\lambda}\right)$ using (9.7) gives

$$B_g = a_0 - a_2\lambda^2 - 2a_3\lambda^3 \ldots \tag{9.8}$$

Interestingly, (9.8) implies that a linear wavelength dependence makes no contribution to the group birefringence. In addition if the wavelength dependence is entirely linear then the fibre would possess non zero B_m and zero B_g. Such a fibre would be polarisation maintaining and at the same time have zero polarisation mode dispersion.

Unfortunately, fitting a power series does not allow the coefficient a_1 to be determined readily and the power law method was used throughout the following experimental study.

9.4 Results

(a) **Temperature dependence experiments**

A 1.2 m sample of the HiBi-PCF was placed in an environmental chamber and temperature tested from –25 to 95°C. Interferograms were recorded at approximately 25 degree intervals between –25 and 95°C. The test sample was then shortened to 0.53m to fit it inside a tube furnace where the fibre was tested over the temperature range from 95 to 800°C and interferograms were recorded at 50-degree intervals. Over the entire test temperature range the modal birefringence only varied between 1.11×10^{-4} and 1.14×10^{-4}, which corresponds to a range of approximately +/- 1.5%. This is within the range of the experimental error. The modal birefringence, at the central wavelength (1540nm), as a function of temperature is represented by the crosses in Fig. 9.5. For comparison, the temperature dependence of the modal birefringence of conventional bow-tie HiBi fibre is also shown on the same graph. A large slope is evident for the bow-tie HiBi fibre, whereas the HiBi-PCF is flat within experimental error throughout the entire temperature range.

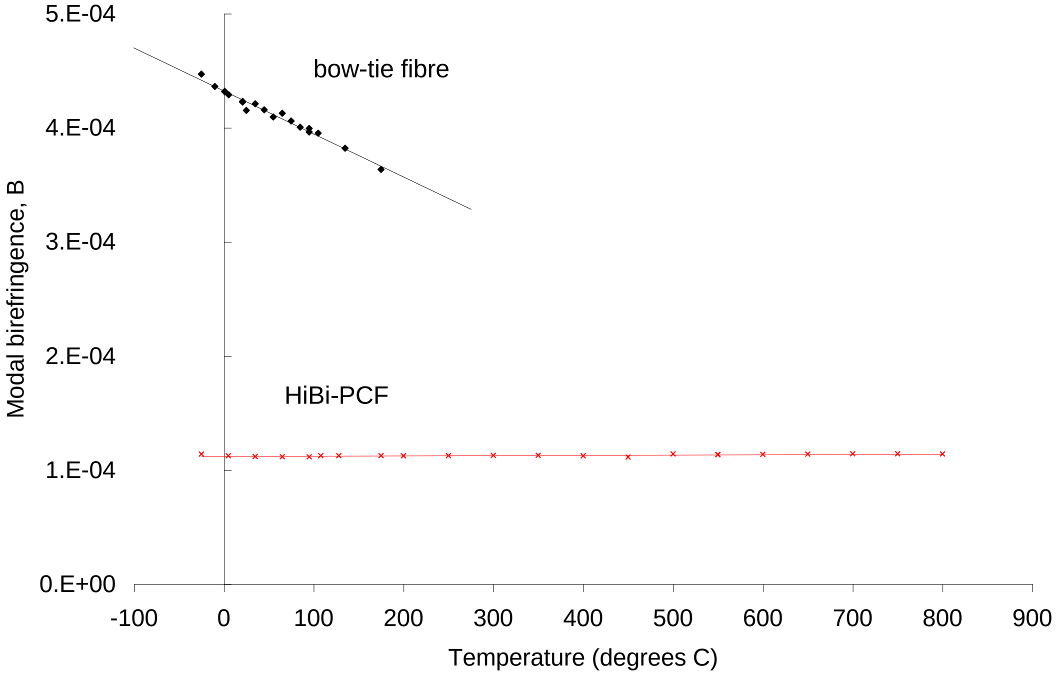

9-5 Temperature dependence of modal birefringence for a bow-tie fibre and HiBi-PCF

(b) Determining the wavelength dependence of the HiBi-PCF

The group birefringence of the HiBi-PCF was measured over a broad wavelength range using both a white light source and an EDF-ASE source. These values were then plotted (see Fig. 9-6) and a power law function of the form $B_g = -\alpha(k-1)\lambda^k$ was numerically fitted to the data to determine the *k* value. This *k* value was then used to calculate the modal birefringence of the HiBi-PCF using (9.6) (also shown in Fig. 9-6). When the two curves are plotted they appear to diverge with increasing wavelength. However, the modal birefringence is a constant fraction of the group birefringence in accordance with (9.6). The resulting modal birefringence measured at 1540nm for this HiBi-PCF is 1.13×10^{-4}.

The group birefringence of a sample of conventional bow-tie HiBi fibre was also characterised using the same methods. In this case the fibre was designed to operate around 800nm and was too lossy at 1550nm to use the EDF-ASE source and the white light source only was used. The relatively flat wavelength dependence can be seen in Fig. 9.6.

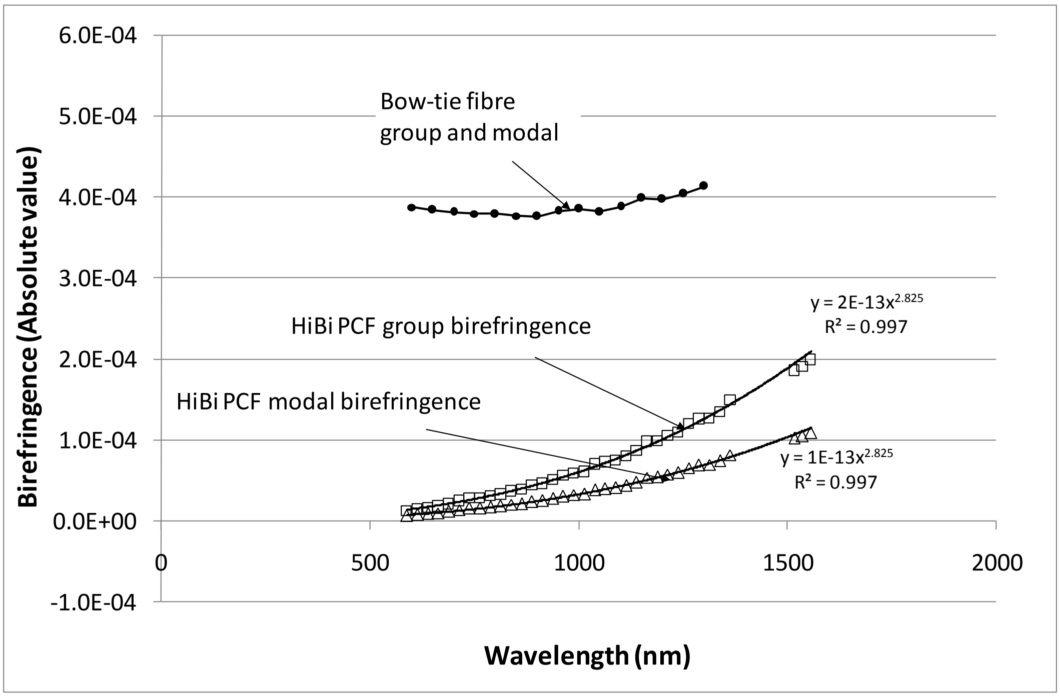

9-6 Birefringence as a function of wavelength of a bow-tie fibre and the HiBi-PCF

4. Discussion and conclusion

The group birefringence of the HiBi-PCF studied here is, within experimental error, independent of temperature over the range –25 to 800°C. These results not only reinforce the assumption that birefringence based purely on waveguide geometry is largely temperature independent, they also suggests the absence of residual thermal stresses in this fibre. The large temperature range for these tests suggests a possible usefulness beyond the normal operating range for optical fibres. During these tests the acrylate coating material was completely burnt away above 400°C leaving behind bare uncoated fibre. The challenge may be in finding coating materials that could operate over an equally extended temperature range.

Sensing and interferometric applications requiring polarisation maintaining fibre with little or no temperature dependence may benefit greatly from using such HiBi-PCFs. HiBi-PCFs with low temperature dependence could also be designed to incorporate other features such as special dopants for sensing and amplification such as in a singly and strongly polarised high power fibre laser, for example. In addition polarising fibre with large and thermally stable polarizing windows could be manufactured.

It has also been shown that by studying the wavelength dependence of the group birefringence, the modal birefringence can be determined. The experimentally determined value of k, defined in equation 9.5 above, for this fibre was found to be 2.82. Substituting this k value into (9.5) gives a group and modal birefringence that are opposite in sign. This means that the fast and slow axes of the fibre are reversed when considering the phase and group velocities of the polarisation modes. In addition the analysis suggests that a HiBi fibre that is characterized by having birefringence that is entirely linearly wavelength dependent will possess polarisation maintaining properties but will not suffer from polarisation mode dispersion.

Chapter 10. Spun elliptically birefringent photonic crystal fibre for current sensing

10.1 Introduction

Since the first photonic crystal fibre (PCF) was reported, PCFs have been expected to take on major importance in shaping the future of optical fibre sensing technology [3, 64, 65]. PCFs utilize an internal structure that offers alternative guidance mechanisms, such as band gap structures, a single material construction and the possibility of optical interaction with the contents of the holes. This single material construction potentially removes any residual thermal stresses in the fibre due to differential thermal expansion coefficients during the drawing process. This internal structure can also be designed to produce significant form birefringence and in chapter 9 it has been demonstrated that these fibres have negligible temperature dependence of birefringence over extended temperature ranges [4, 7].

Electric current sensing using Spun Highly Birefringent (Spun HiBi) optical fibres is an idea that has been around since the late 1980s [66]. Linear birefringence in the sensing fibre quenches the Faraday-induced rotation effectively reducing the sensitivity to magnetic fields. Spinning a HiBi fibre preform during the fibre draw process adds circular birefringence to a structure that would otherwise have very large linear birefringence [66, 67]. The resulting elliptical birefringence partially restores the sensitivity to magnetic fields and retains the desirable polarisation maintaining properties normally associated with HiBi fibres. In addition, this fibre allows for flexible and ruggedised packaging through being largely insensitive to bending birefringence and other environmental perturbations.

Conventional stress induced hi-birefringence optical fibres and their spun counterparts suffer from significant changes in linear birefringence with temperature.

This presents a real problem for both the fibre optic gyroscope (FOG) and the fibre optic current sensor (FOCS) that employs stress birefringence fibre where errors and sensitivity changes can occur if temperature gradients occur within the sensor packaging. Overcoming this problem has proven difficult and expensive solutions such as active stabilisation of temperature and other environmental perturbations have emerged for high accuracy sensor systems [68, 69]. The development of low cost temperature insensitive optical fibres would go a long way towards addressing this issue.

Fibre optic gyroscopes (FOG) have been demonstrated using bandgap fibres, where the light is guided in a hollow core region surrounded by a periodic structure made up of the host material and rings of holes [70]. These fibres offer reduced temperature dependence, and low non-linearity, since the light is guided mostly in the air core region. Although these fibres largely remove the temperature dependence in the effective refractive index of the material the temperature performance was limited by changes in the physical path length due to the thermal expansion of the host material. These fibres are generally far more expensive to make than solid photonic crystal fibres and have another set of technical challenges (including splicing and coupling) that have yet to be dealt with. Ideally, the low loss properties of conventional effective index guiding (commonly known as modified total internal reflection guiding) photonic crystal fibres combined with low temperature dependence are desired.

The beat length of HiBi-PCFs at 1550nm has been made as low as 0.27mm, an order of magnitude shorter than conventional bow-tie fibres (typically >2mm @ 1550nm) [6]. Loss in PCF fibres has also become more than acceptable with improvements in fabrication techniques and PCFs are now beginning to challenge the more conventional step index fibres with loss as low as 0.37dB/km at 1550nm [71].

A HiBi-PCF preform, made using the same methods described in chapter 9 [4], has been spun during the fibre draw process. In this chapter the ellipticity of the resulting Spun HiBi-PCF has been determined using a simple approach outlined in the next section. Further, the temperature dependence of the birefringence has been characterised and the results are also presented.

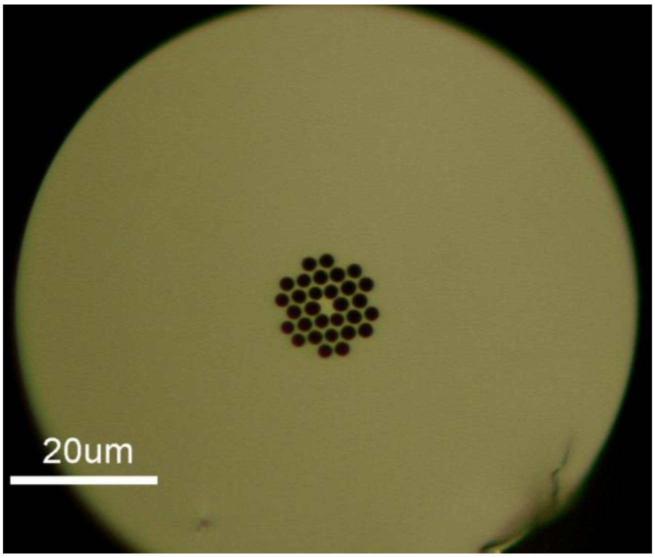

10-1 Spun Hi-Bi photonic crystal fibre cross-section

Spinning PCF preforms during the drawing process will produce a permanent twist that is frozen into the fibre. The longitudinal array of holes will now be effectively arranged helically along the length of the fibre. This helical structure will possess circular birefringence and when combined with the large inherent linear birefringence will give a resulting elliptical birefringence. The use of elliptically birefringent fibres for current sensing has been widely studied [59, 66, 67, 72]. When using this spun PCF for current sensing, only the temperature dependence of the Verdet constant remains.

The Spun Hi-Bi-PCF initial preform was fabricated by the conventional capillary stacking method. Three rings are employed with an elliptical core whilst otherwise maintaining a more or less regular triangular lattice. In order to spin the optical fibre, a custom preform spinning unit capable 4000 revs/min was designed and installed into a commercial grade draw tower. The six fold rotationally symmetric preform was first drawn, preserving the preform geometry, into an unspun optical cane with a core of approximately 10µm. The cane was then inserted into a second tube for a second stage fibre draw that resulted in a flattened collapse to produce an approximately elliptical shaped core, with a major and minor core diameters of 3 x 2µm respectively, whilst spinning at ~1300revs/min and drawing at 10m/s. This produced a spin pitch of approximately 7.7mm. Fig. 10-1 shows the final fibre cross section achieved.

10.2 *Elliptical birefringence*

(a) **Background**

To understand the effect of spinning the fibre preform on the birefringence of the fibre it is convenient to use the Poincaré sphere. Figure 10.2 shows elliptical polarisation eigenmodes P^+ and P^- that are the preserved polarisation states (relative to local axes, which keep up with the spin) of the elliptically birefringent Spun HiBi-PCF. The elliptical birefringence can be represented by the vector $\vec{\rho}$ passing through these preserved states in Poincaré space. The length of the vector $\vec{\rho}$ represents the magnitude of the phase shift per metre induced by the birefringence. Similarly $\vec{\tau}$ represents the spin induced circular birefringence and $\vec{\eta}$ represents the local linear birefringence of the equivalent unspun fibre. The terms $\overrightarrow{\eta}$, $\vec{\tau}$ and $\vec{\rho}$ all have the units radians per metre (rad/m). The magnitude of these phase shift terms can be expressed as

$$|\vec{\eta}\,| = {}^{2\pi}/_{L_B} \qquad |\vec{\tau}\,| = {}^{4\pi}/_{L_T} \qquad |\vec{\rho}\,| = {}^{2\pi}/_{L_{B'}} \tag{10.1}$$

where L_B is the familiar beatlength of the linear birefringence term, L_T is the spin pitch and $L_{B'}$ is the elliptical beatlength in metres [8,9]. In Poincaré space a 2π rotation of any polarisation state is equivalent to a π rotation in the laboratory frame. As a result spinning the fibre preform through 2π radians is equivalent to a 4π rotation in Poincaré space. Hence the factor 4π that appears in the second member of (10.1).

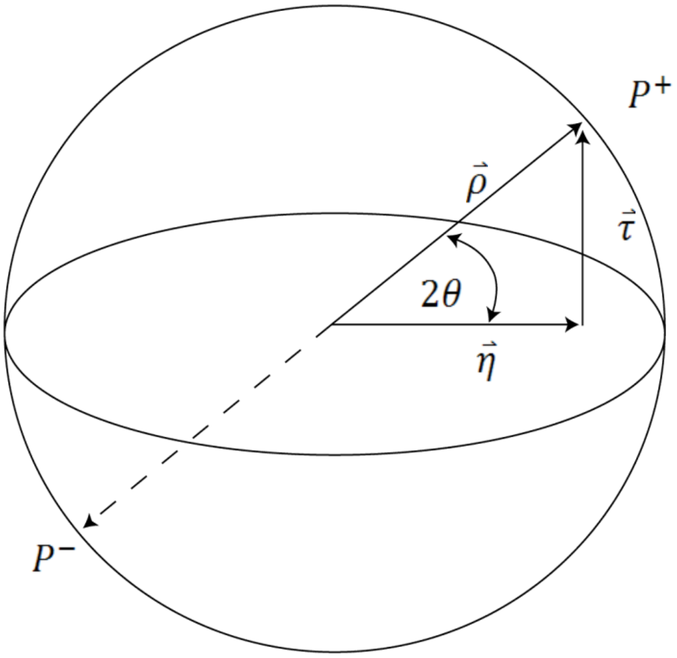

10-2 Representation of polarisation states and birefringence in Poincaré space

10.3 Current sensitivity

The strength of the Faraday effect in a material is represented by V the material's Verdet constant where V describes the phase shift per unit length between orthogonal circular polarisation states when exposed to a magnetic field parallel to the direction of propagation of light [13]. The sensitivity to current of the Spun HiBi due to the Faraday Effect can be represented by an effective Verdet constant V_s and the phase shift per unit length between the orthogonal elliptical polarisation states P^+ and P^- is

$$V_s = V sin 2\theta \tag{10.2}$$

where V is the Verdet constant of straight non birefringent fibre and θ is the ellipticity measured as discussed in section 10.4(a) below [22, 73]. From (10.2) it can be seen that fibre with only circular birefringence, where $2\theta = \pi/_2$, has the same sensitivity as straight non birefringent fibre.

10.4 Measurement approach

(a) **Introduction**

A modified version of the Mach-Zehnder two polarisation interferometer (MZ-TPI) presented in section 3.1 was used to analyse the elliptical birefringent Spun HiBi PCF. Broadband light from an erbium doped fibre amplified spontaneous emission (EDF-ASE) light source was passed through a fibre pigtailed polarising beam splitter (PBS) spliced to a section of Spun HiBi PCF. The fibre end was rotated and aligned to excite roughly equal amounts of power into each elliptical polarisation mode of the Spun HiBi PCF. The light emerging from the Spun HiBi PCF end was then analysed with a linear polariser and the wavelength dependent modulation, or interferogram, was observed. In the case of linearly birefringent fibre the output spectrum from a single linear polarisation state can be observed by simply rotating the polariser at the output until the modulation is completely extinguished. The orthogonal state can then be observed simply by rotating the output polariser through +/- 90 degrees.

For the Spun HiBi-PCF the modulation could not be completely extinguished by rotating the output polariser due to elliptical birefringence. With the linear output polariser aligned with one of the preserved polarisation states of the linear birefringence vector $\vec{\eta}$, (i.e. with the minor axis of the ellipse of the elliptical polarisation state), the modulation was minimised. The addition of a Babinet-Soleil phase (BSP) compensator between the output end of the Spun HiBi-PCF and the linear polariser allows for some retardance to be added effectively turning the linear output polariser into an elliptical polariser. Alignment and adjustment of the BSP allowed the output modulation to be completely extinguished. The BSP was then calibrated at the operating wavelength to determine the retardance and the ellipticity (θ) was then calculated.

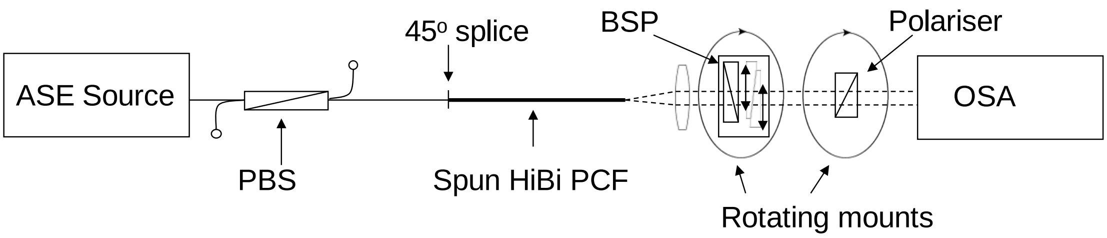

10-3 Experimental set up for measuring the ellipticity of the spun HiBi PCF

(b) Birefringence measurement

The modal (or phase) birefringence B_m is defined as [Appendix C, (C.1)]

$$B_m = \left| n_{eff}^{x} - n_{eff}^{y} \right| = \Delta n_{eff} \tag{10.3}$$

where n_{eff}^{x} and n_{eff}^{y} are the effective refractive indices for each polarisation mode. The birefringence is often presented in the form of a beat length given by

$$L_B = {}^{\lambda}\!/_{B_m} \tag{10.4}$$

where λ is the free space wavelength. Using the same methods presented in chapter 9 the group birefringence, B_g, can be determined by measuring the period of the modulation seen in the output spectrum and using the following relationship [4]

$$B_g = -\left(\frac{\lambda d\, B_m(\lambda)}{d\lambda} - B_m(\lambda)\right) = -\frac{\lambda^2}{2L\Delta\lambda} \tag{10.5}$$

where L is the length of the Spun HiBi-PCF being tested and $\Delta\lambda$ is period of the spectral modulation seen in the output. However, to determine the modal birefringence from the interferogram the wavelength dependence of the birefringence must be known. For HiBi PCF a power law dependence has been widely used and requires measuring the interferogram over a very broad wavelength range [4].

Figure 10-2 shows that if the spin-induced circular birefringence and the ellipticity are known then either the elliptical birefringence of the Spun HiBi-PCF or the local linear birefringence of the equivalent unspun HiBi-PCF can be calculated using simple trigonometry. As a result this method allows the modal birefringence of the Spun

HiBi-PCF to be determined without the need for characterisation over an extended wavelength range.

The spin induced circular birefringence $\vec{\tau}$ can be calculated using equation (10.1). The elliptical modal birefringence $\vec{\rho}$ can then be calculated once the ellipticity θ has been determined using the following simple trigonometric relationship

$$\vec{\rho} = {}^{\vec{\tau}}\!/_{sin2\theta} = {}^{4\pi}\!/_{L_T sin2\theta} \qquad (10.6)$$

Similarly the value of $\vec{\eta} = 2\pi/L_B$ can be calculated using

$$\vec{\eta} = \vec{\tau}cot2\theta \qquad (10.7)$$

(c) Temperature dependence measurements

The group birefringence, B_g, was calculated using (10.5) from the recorded interferograms obtained using the crossed polariser method configured in reflection. The EDF-ASE source provided enough power that the Fresnel reflection from the cleaved end of the Spun HiBi-PCF produced a clear interferogram at the output.

The entire Spun HiBi-PCF was subsequently placed in an environmental chamber and the group birefringence was recorded from -25°C to +100°C. Below 20°C condensation on the cleaved fibre end reduced the Fresnel back reflection and increased the experimental noise.

10.5 Results and Discussion

A 630mm length of Spun HiBi-PCF was tested using the experimental set up shown in figure 10-3 and described above. The periodic modulation seen in the output spectrum (figure 10-4) was recorded using an optical spectrum analyser and the period and depth of the modulation were determined. The linear polariser at the output was then rotated and the modulation depth minimised but not fully extinguished. The BSP compensator was initially set to zero retardance $(R_i = 0)$ and was arbitrarily orientated relative to the linear polariser. The BSP was then re-orientated so that its fast and slow axes were aligned at 45^0 to the linear polariser. The retardance was then adjusted to fully extinguish the periodic modulation and the retardance $(R_1 = \theta_1)$ was recorded. The BSP was then calibrated by continuing to add retardance until the periodic modulation was again extinguished $(R_2 = \theta_2)$.

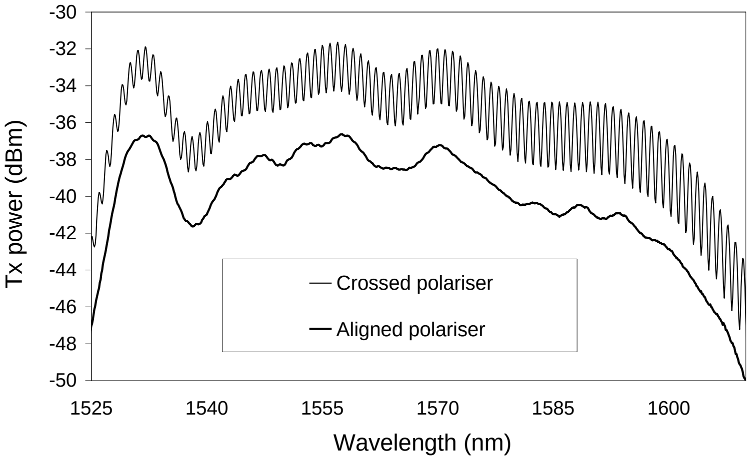

10-4 Interferograms recorded both when the periodic modulation is extinguished and also when it is maximised.

The difference in retardance indicated by the BSP settings R_1 and R_2 for these two positions corresponds to π radians in Poincaré space. From the ratios of the two, the ellipticity of the Spun HiBi-PCF birefringence reduces to

$$\theta = \left[{}^{R_1}\!/_{2(R_2 - R_1)} \right] . \pi \text{ rad.} \tag{10.8}$$

For this section of Spun HiBi an ellipticity of approx $\theta = (0.12 \pm 0.02)$ rad was observed. Using (10-2) above the Spun HiBi-PCF would retain approx (22 ± 4) % of the sensitivity to current of an entirely circularly birefringent fibre.

Using this measured value for $\theta = (0.12 \pm 0.02)$ rad and the spin pitch of $L_T = 7.7$mm we can estimate the effective modal birefringence of the Spun HiBi-PCF using (10.1) and (10.6) as follows. A circular birefringence of $|\vec{\tau}\,| = {}^{4\pi}\!/_{L_T} \cong 1631$ rad/m is produced by spin pitch of $L_T = 7.7$mm (10.1). Inserting into (10.5) and (10.6) gives $|\vec{\eta}\,| = {}^{2\pi}\!/_{L_B} = 6970 \pm 600$ rad/m and $|\vec{\rho}\,| = {}^{2\pi}\!/_{L_{B'}} = 7159$ rad/m. At 1550nm, the average test wavelength, the corresponding beatlengths are $L_B = 0.90 \pm 0.06$ and $L_{B'} = 0.88 \pm 0.06$ mm. For comparison the elliptical beatlength of $L_{B'} = 0.83$mm was calculated from the periodic modulation using the methods described in chapter 9 and assuming the same k value of 2.8 for this fibre. This represents good agreement between the two different methods for determining the modal birefringence of the Spun HiBi PCF and is supportive of the analysis presented above.

The same section of Spun HiBi PCF was then configured in reflection and placed inside the environmental chamber. The group birefringence was recorded every 10 degrees between -25 and 100°C. The change in group birefringence relative to the value recorded at room temperature is presented in figure 10.5 along with results for a HiBi Panda fibre. The increased temperature sensitivity for the Panda fibre is clearly evident in the graph and no change in group birefringence within the experimental error range is observed for the Spun HiBi-PCF. In the case of Spun Panda fibre the ellipticity, and the corresponding sensitivity to current, is then affected by changes in temperature. Although the spin pitch remains relatively constant the Panda fibre's birefringence changes significantly with temperature resulting in large changes in ellipticity and sensitivity to current. The use of Spun HiBi-PCF fibre removes this problem since the ellipticity is now largely temperature independent. Although there remains a small temperature dependence in the basic material Verdet constant, of the order of 70ppm/°C [74], for silica based fibres this effect is still an order of magnitude smaller than the high temperature dependence seen in spun Stress HiBi fibres.

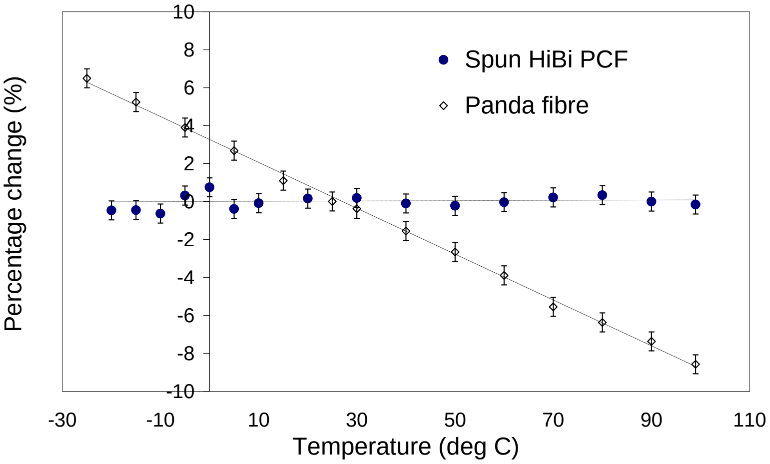

10-5 Group birefringence versus temperature for both a conventional stress birefringence Panda fibre and the Spun HiBi -PCF

10.6 Conclusion

A spun highly birefringent photonic crystal optical fibre has been characterised for the first time for ellipticity and temperature dependence. This fibre offers a stable effective Verdet constant with low temperature dependence and low packaging sensitivity. In addition what can be observed is that in contrast to bandgap fibres a much lower number of rings are used allowing a significant amount of silica in the cladding. This in turn permits conventional splicing and coupling techniques to be employed in the practical packaging of such fibres.

The use of the Poincaré sphere to represent polarisation and elliptical birefringence allows for an alternative method that is simple to implement for determining the modal birefringence of the Spun HiBi-PCF structure that does not require measurements over a very large wavelength range.

Further refinements in design will potentially provide broad band polarising properties that will allow Spun HiBi-PCFs to be used effectively for current sensing and other variations will undoubtedly find application in established areas such as fibre optic gyroscopes. Additionally, these fibres may permit a level of temperature independent control of polarisation that may be of benefit for new areas such as quantum communications based on polarisation degeneracy between entangled light paths.

Chapter 11. Conclusion

11.1 Interferometry

The majority of the experiments and analysis presented in this thesis are based on a simple low coherence interferometer that was introduced in chapter 3 (sections 3.1 and 3.2), and described as a two polarisation interferometer (TPI). The TPI allows for the two separate optical paths to be contained within the core of a single piece of birefringent sensing fibre, providing for excellent common mode rejection. The TPI has been configured both as a Michelson (M-TPI) and as a Mach-Zehnder (MZ-TPI) interferometer. Due to the reflection configuration, in most cases the M-TPI was the preferred configuration since remote sensing, over a few metres in the lab, was possible as the interferometer could be interrogated from a single end of the sensing fibre. Since the optical fibre cable connections from the TPI to the light source and the optical receiver were ordinary single mode fibres the remote sensing distance could be readily extended and is limited mainly by loss and power budget issues. Remote sensing over the typical distance of up to 1km between the control room and the voltage sensor in an air insulated, outdoor electricity substation is considered possible. Both the M-TPI and the MZ-TPI produced a small and relatively stable path imbalance. The path imbalance resulted in strong and repeatable wavelength dependence in the output spectrum, with the phase and period, around the average wavelength, determined by the total retardance in the birefringent sensing fibre. The TPIs are then predominantly sensitive to changes in total retardance ideally through modulating the sensing fibre birefringence, but also to a lesser extent through changes in the length of the sensing fibre. The initial analysis indicated that slow changes (or drifts) in the total retardance of the birefringent sensing fibre were considered both possible and unavoidable but were likely to be small due to the excellent common mode rejection properties of the TPIs. When applying the M-TPI to voltage sensing it was only ever considered as a possible AC solution since slow DC drifts would be present. The DC drift could then be removed by filtering at the operating frequency i.e. 50 or 60Hz.

11.2 The signal processing system

Recording the output spectrum from the M-TPI or the MZ-TPI with an optical spectrum analyser and then processing in a digital signal processing system allowed for the phase, period and magnitude of the periodic modulation to be determined. A simplified version of a Discrete Fourier Transform (DFT) was used to process the output spectral data very quickly and efficiently. Three generations of the signal processing system were produced with the effective sampling rate ranging from approximately 1 Hz to 5000Hz for generation 1 to generation 3. Sampling at 5000Hz involves collection of a complete spectral scan (or spectrum) and calculating the phase of the periodic modulation using the simplified DFT 5000 times per second.

11.3 The application to voltage sensing

The application of the M-TPI to voltage sensing for the electricity transmission industry using thermally poled silica optical fibre that possesses a small polarisation dependence in its electro-optic response has been the main focus of the work presented in this thesis. The electric field arising from the high voltage electricity transmission lines modulates the birefringence of the sensing fibre and this can be observed as a phase change in the periodic modulation seen in the output spectrum.

The experiments and the 3 generations of the voltage sensor signal processing system are presented in the chronological order of their development. The work began by confirming the existence of a small polarisation dependence in the electro-optic response and verifying that the M-TPI only responds to the polarisation dependent differential electro-optic response (DLEO). These results are presented in chapter 4.

The signal processing system then evolved through the 3 generations by focussing on continually improving the targets and performance of the spectral data acquisition and signal processing system. The interferometer design remained the same throughout the three generations. The design, analysis and performance characterisation of the three generations is presented in chapters 6-8. Improvements in the sensing fibre design that aided the packaging of the sensing fibre, such as the double flat for automatic alignment, are included as part of the system performance discussions in chapter 8.

The results presented in chapter 8 (section 8.3) for the coiled voltage sensor, packaged in a porcelain insulator designed for operation at 36 kV RMS, were very promising. The sensor responded linearly when varying the test voltage over the range 0-17kV RMS. The noise floor of 690V RMS is high and needs to be improved. International standards for the electricity transmission industry have various accuracy class requirements for voltage and current transformers such as 0.2% and 0.5%. The noise floor of 690V RMS obtained in the experiments (section 8.3) corresponds to accuracy of approximately 2% at an operating voltage 36 kV RMS. To satisfy the international standards, signal to noise performance needs to be improved by at least an order of magnitude. This may be achieved either by making the length of poled fibre longer or increasing the differential electro-optic response of the poled fibre, or both.

In summary, voltage sensing using coiled thermally poled silica fibre has been demonstrated and the design, analysis and results are presented in this thesis.

11.4 Insights into poling

Since the voltage sensor employed thermally poled silica as the electric field and voltage sensing fibre, many experiments were performed to prepare lengths of poled silica fibre. These experiments often lead to interesting observations and potential distractions from the main focus of producing a voltage sensing system.

(a) **Polarisation dependence**

The observed polarisation dependence that proved to be significantly smaller than suggested by the analysis presented in Appendix B, deserved further attention. Fortunately the broader research community studying the distribution of the non-linear region have provided beautiful images showing how the non-linear region wraps itself around the core of the twin-hole fibre. The mode then effectively sees a lower average polarisation dependence. This qualitatively explains a significant contributing factor to the smaller than expected polarisation dependence. Finite element analysis methods could be used to more quantitatively verify this hypothesis.

(b) **Multi-wavelength experiments**

The voltage sensor can potentially operate with poled fibres that have a lower electro-optic response than that required to make commercially viable electro-optic modulators for the telecommunications industry. However, the coiled voltage sensor arrangement presented in this thesis does require a sufficiently uniform electro-optic response along the entire length of the poled fibre. The modelling of the intensity distribution of the guided mode over a broad wavelength range, along with the multi-wavelength measurements presented in chapter 5, have lead to a potential non destructive method for optimising the poling conditions so that the core can be placed in a region of relatively uniform non-linearity. Designing a fibre cross section where the core is deliberately placed in the region with the most uniform non-linearity is expected to make the electro-optic response of the poled fibre less dependent on variations in poling conditions.

11.5 The application to characterisation of HiBi PCFs

Both the M-TPI and the MZ-TPI were used to characterise HiBi-PCFs. The temperature and wavelength dependence of the birefringence of both spun and unspun HiBi PCFs were studied and novel methods are presented for determining the wavelength dependence of the modal birefringence from the measured wavelength dependence of the group birefringence. The extremely low temperature dependency observed in the HiBi-PCFs is likely to be a significant driving factor in the adoption these fibres where temperature gradients within sensor packages limit performance.

11.6 Opportunities for further research work

The voltage sensor work is continuing through an Australian Research Council (ARC) linkage grant with ABB and TransGrid. One of the outcomes of this project is to test the voltage sensor system in ABB's High Voltage (HV) test lab. This work is expected to be completed in 2008. Following this, a greater understanding of the performance of the voltage sensor system will be gained and any necessary improvements in sensitivity will be highlighted. Further mechanical testing of the packaged sensor will be required, including tests such as immunity to shock and vibration. Environmental testing over a broad temperature and humidity range will also be required and perhaps most importantly the thermally poled silica fibre itself will need to be tested for long term stability of its electro-optic response. The lifetime of the electro-optic response in thermally poled optical fibres has been studied and it appears to be highly dependent on the fibre composition and fibre cross section design [32, 75]. Encouragingly the GLAMOROUS project reported at the Bragg Gratings, Poling and Photosensitivity (BGPP/ACOFT 2005) that their thermally poled fibres have shown no decay in electro-optic response over 1 year at room temperature [35].

11.7 The commercial opportunity

Ultra high voltage (UHV) electricity transmission at 800 -1200 kV AC is considered a goal for bulk power transmission, particularly in emerging and rapidly developing markets such as India and China. Transmission systems built in Russia and China that are designated 1000kV systems only operate at less than 800kV. Instrument transformers that can measure voltage at greater than 800kV are at present not offered by any of the three biggest suppliers of electricity transmission equipment i.e. ABB, Siemens and Areva. The voltage sensing methods presented in this thesis form a technology foundation that may prove successful in realising an ultra high voltage sensor. Commercially this technology will be competing with the existing capacitive voltage transformers (CVTs) that will undoubtedly be improved and redesigned for increased operating voltage. Ultimately, a significant commercial opportunity exists for the successful technology.

Appendix A Non linear optics and tensors for poling

This appendix contains a more detailed analysis of some of the non-linear effects that are particularly useful when working with poled optical fibres.

A.1 Notations, conventions and symmetry arguments

A detailed and lengthy literature search on the topic of non-linear optics for poling can be frustrating due to a number of factors such as inconsistency in notation. Even greater frustration occurs when, in the literature, derivations and discussions for interesting non-linear phenomena are prematurely abbreviated with text equivalent to *symmetry constraints imply* without any further discussion. This appendix attempts to fill in these missing steps and explain the relationship between some of the alternative notations found.

In addition, the index ellipsoid is introduced to explain the relationship between the susceptibility χ, the refractive index n, and the electro-optic response. The commonly presented forms of the Pockels and Kerr coefficients are discussed using the scalar, and tensor form and the popular shorthand tensor form.

The polarisation dependence of the electro-optic response, on which the low coherence interferometric system relies, is discussed using the tensor form of the polarisability. To support this analysis the symmetry considerations that greatly reduce the complexity of the problem are explained in appendix B.

A.2 Electric impermeability, index ellipsoid, dielectric constant and refractive index

In many optical fibre applications, such as interferometry, the effective refractive index of the guided modes is of great interest. In the case of electro-optic responses, due to both $\chi^{(2)}\ and\ \chi^{(3)}$, it is often more informative to know how the refractive index responds to an incident electric field than to completely understand the non-linear polarisation.

The electric displacement field **D** is defined by the relation

$$\mathbf{D} = \varepsilon_0 \mathbf{E} + \mathbf{P} \tag{A.1}$$

where **E** is the electric field, ε_0 is the permittivity of free space, and **P** is the dipole moment per unit volume or polarisation density.

The electric displacement field **D** can be expressed in terms of the electric polarisability $\boldsymbol{\chi}$ as

$$\mathbf{D} = \varepsilon_0 (1 + \boldsymbol{\chi}) \mathbf{E} = \boldsymbol{\varepsilon} \mathbf{E} \tag{A.2}$$

where $\boldsymbol{\varepsilon}$ is the electric permittivity.

The electric impermeability tensor $\boldsymbol{\eta} = {}^{\varepsilon_0}\!/_{\boldsymbol{\varepsilon}}$ can be used to construct the index ellipsoid i.e.

$$\sum_{ij} \eta_{ij} x_i x_j = 1, \qquad i,j = 1,2,3, \tag{A.3}$$

where η_{ij} are the elements of the impermeability tensor $\boldsymbol{\eta}$. The index ellipsoid and the electric impermeability tensor can be used to describe dielectrics and anisotropic materials such as crystals. The principal axes of the ellipsoid are the principal optical axes of the dielectric and the dimensions along these axes are the corresponding refractive indices (see figure A-1). In the case of optical fibre where the propagation direction or axis of the fibre may be assigned to the z direction, or axis, of the index ellipsoid and then the dimensions along the x and y axis are the refractive indices for x and y polarised modes. i.e.

$$\eta_x = {}^{\varepsilon_0}\!/_{\varepsilon_x} = {}^{1}\!/_{{n_x}^2} \text{ and } \eta_y = {}^{\varepsilon_0}\!/_{\varepsilon_y} = {}^{1}\!/_{{n_y}^2} \qquad \text{respectively} \tag{A.4}$$

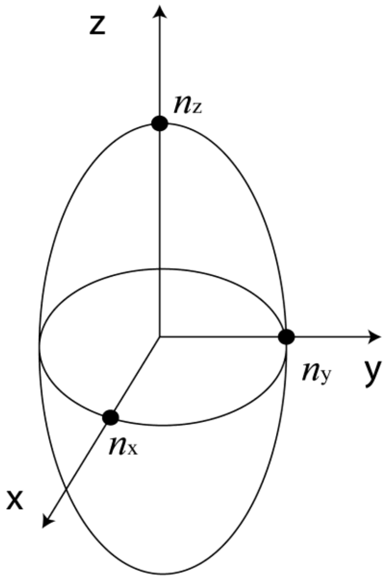

11-1 The index ellipsoid showing the principal axes of the dielectric (x,y,z) and the corresponding refractive indices (n_x,n_y,n_z)

The presence of a DC electric field will alter the index ellipsoid so that elements of the index ellipsoid become a function of the electric field i.e $\eta_{ij}(E)$. To include the non-linear response the electric impermeability tensor can be expanded in a Taylor's series about E=0 as follows.

$$\eta_{ij}(E) = \eta_{ij} + \mathfrak{r}_{ijk} E_k + \mathfrak{s}_{ijkl} E_k E_l \qquad i,j,k,l = 1,2,3, \tag{A.5}$$

where $\eta_{ij} = \eta_{ij}(0)$, $\mathfrak{r}_{ijk} = {}^{\partial \eta_{ij}}\!/_{\partial E_k}$, $\mathfrak{s}_{ijkl} = \frac{1}{2}\, {}^{\partial^2 \eta_{ij}}\!/_{\partial E_k \partial E_l}$ and the derivatives are evaluated at E=0. The summation notation over repeated indices is implied and the $\mathfrak{r}_{ijk}$ and $\mathfrak{s}_{ijkl}$ coefficients are called the Pockels and Kerr coefficients respectively.

A.3 Alternative notations

In the literature the scalar form of the susceptibility is often presented in one of two basic forms below

$$P = \varepsilon_0(\chi^{(1)}E + \chi^{(2)}E^2 + \chi^{(3)}E^3) \tag{A.6}$$

or

$$P = \varepsilon_0 \mathcal{X}^{(1)}E + 2dE^2 + 4\mathcal{X}^{(3)}E^3 \tag{A.7}$$

The second order non-linear coefficient d is widely used in the literature to describe the second order non-linear response of a dielectric and the relationship between d

and $\chi^{(2)}$ is obtained by equating the coefficients of the second order terms in equations (A.6) and (A.7) giving

$$d = \varepsilon_0 \frac{\chi^{(2)}}{2} \tag{A.8}$$

In the following text the second order non-linear coefficient *d* is italicised to distinguish it from the incremental change dX in a quantity X when a derivative is implied.

A.4 Linking together the non-linear susceptibilities, and the Pockels and Kerr coefficients

In section A.2 above the influence of an incident electric field on the electric impermeability $\boldsymbol{\eta}$ is introduced. A simplified scalar form of equation (A.5) is

$$\eta(E) = \eta + \mathfrak{r}E(0) + \mathfrak{s}E(0)^2 \tag{A.9}$$

where $\boldsymbol{\eta} = \frac{1}{n^2} = {}^{\varepsilon_0}/_{\boldsymbol{\varepsilon}}$ and $E(0)$ is the incident DC electric field at frequency ω=0.

Since the change $\Delta\eta$ induced by the DC electric field $E(0)$ is small relative to η the quantity ${}^{\Delta\eta}/_{\Delta\mathrm{n}} \cong {}^{\mathrm{d}\eta}/_{\mathrm{dn}} \ = -{}^{2}/_{\mathrm{n}^3}$

Rearranging, $\Delta\mathrm{n} = {}^{-\mathrm{dn}}/_{\mathrm{d}\eta}\,\Delta\eta = -\frac{1}{2}\mathrm{n}^3\Delta\eta$, and substituting $\Delta\eta = \ \mathfrak{r}E(0) + \mathfrak{s}E(0)^2$ we obtain the following expression for the refractive index

$$\mathrm{n}(E) = \mathrm{n} + \Delta\mathrm{n} = \mathrm{n} - \overbrace{\frac{1}{2}\mathrm{n}^3\ \mathfrak{r}E(0)}^{1} - \overbrace{\frac{1}{2}\mathrm{n}^3\ \mathfrak{s}E(0)^2}^{2} \tag{A.10}$$

Term 1 in equation (A.10) represents the linear change in the refractive index in response to the incident electric field $E(0)$ and term 2 represents the quadratic response.

To extend this analysis to include the induced polarisation the example presented in chapter 2, section 2.7 can be used i.e. an incident electric field $E_{(t)} = E_{(0)} + E_{(\omega)}$ will induce the following polarisation in the dielectric

$$P = \overbrace{\varepsilon_0\left(\chi^{(1)}E_{(0)} + \chi^{(1)}E_{(\omega)}\right)}^{1} + \overbrace{\varepsilon_0\left(\chi^{(2)}{E_{(0)}}^2\right)}^{2} + \overbrace{2\varepsilon_0\left(\chi^{(2)}E_{(0)}E_{(\omega)}\right)}^{3} +$$
$$\overbrace{\varepsilon_0\left(\chi^{(2)}{E_{(\omega)}}^2\right)}^{4} + \overbrace{\varepsilon_0\left(\chi^{(3)}{E_{(0)}}^3\right)}^{5} + \overbrace{3\varepsilon_0\left(\chi^{(3)}{E_{(0)}}^2E_{(\omega)}\right)}^{6} + \overbrace{3\varepsilon_0\left(\chi^{(3)}E_{(0)}{E_{(\omega)}}^2\right)}^{7} +$$
$$\overbrace{\varepsilon_0\left(\chi^{(3)}{E_{(\omega)}}^3\right)}^{8}\ldots \qquad \text{(A.11)}$$

If we consider a Pockels dielectric that has a strong second order non-linearity and where the third order non-linearity is very small then all the terms in equation (A.11) containing the term $\chi^{(3)}$ can be neglected. If we then specify that the optical field is much smaller than the DC electric field then we can ignore the terms containing ${E_{(\omega)}}^2$. The resulting polarisation is

$$P = \overbrace{\varepsilon_0\left(\chi^{(1)}E_{(0)} + \chi^{(1)}E_{(\omega)}\right)}^{1} + \overbrace{\varepsilon_0\left(\chi^{(2)}{E_{(0)}}^2\right)}^{2} + \overbrace{2\varepsilon_0\left(\chi^{(2)}E_{(0)}E_{(\omega)}\right)}^{3} \qquad \text{(A.12)}$$

and the induced polarisation at the optical frequency $E_{(\omega)}$ is

$$P_{(\omega)} = \overbrace{\varepsilon_0\left(\chi^{(1)}E_{(\omega)}\right)}^{1} + \overbrace{2\varepsilon_0\left(\chi^{(2)}E_{(0)}E_{(\omega)}\right)}^{2} \qquad \text{(A.13)}$$

Term 1 is the linear component at the optical frequency and term 2 is the non-linear component at the optical frequency, i.e.

$$P_{NL(\omega)} = \varepsilon_0\,\Delta\chi E(\omega) = 2\varepsilon_0\left(\chi^{(2)}E_{(0)}E_{(\omega)}\right) \qquad \text{(A.14)}$$

where $$\Delta\chi = 2\,\chi^{(2)}E_{(0)} \text{ or } 4\,{}^{d}\!/_{\varepsilon_0}\,E_{(0)} \qquad \text{(A.15)}$$

For completeness equation A.15 is presented using both $\chi^{(2)}$, and d.

Now since the changes are small $\frac{\Delta\chi}{\Delta \mathrm{n}} \cong \frac{\mathrm{d}\chi}{\mathrm{dn}}$ and using the relation $\mathrm{n}^2 = 1 + \chi$ and $\frac{\mathrm{d}\chi}{\mathrm{dn}} = 2\mathrm{n}$ it follows that

$$\Delta\chi = 2\mathrm{n}\Delta\mathrm{n} \qquad \text{(A.16)}$$

Substituting $\Delta\mathrm{n} = -\frac{1}{2}\mathrm{n}^3\,\mathrm{r}E(0)$ into A.16, an expression for r in terms of *d*, or $2\chi^{(2)}$ can be obtained as follows

$$\Delta\chi = 2\mathrm{n}\Delta\mathrm{n} = -\mathrm{n}^4\,\mathrm{r}E_{(0)} = 2\chi^{(2)}E_{(0)} = 4\,{}^{d}\!/_{\varepsilon_0}\,E_{(0)} \qquad \text{(A.17)}$$

$$\mathfrak{r} = -\,{}^{2\chi^{(2)}}\!/_{\mathrm{n}^4} = -4\,{}^{d}\!/_{\varepsilon_0 \mathrm{n}^4}$$

(A.18)

A Kerr dielectric material that has zero second order non-linearity, but does possess a third order non-linearity, can be treated using the same method where the terms in equation (A.9) containing $\chi^{(2)}$can be neglected and if the optical field is much smaller than the DC electric field then we can ignore the terms containing ${E_{(\omega)}}^2$ and ${E_{(\omega)}}^3$. In this case the induced polarisation is

$$P = \overbrace{\varepsilon_0\left(\chi^{(1)}E_{(0)} + \chi^{(1)}E_{(\omega)}\right)}^{1} + + \overbrace{\varepsilon_0\left(\chi^{(3)}{E_{(0)}}^3\right)}^{2} + \overbrace{3\varepsilon_0\left(\chi^{(3)}{E_{(0)}}^2 E_{(\omega)}\right)}^{3} \qquad \text{(A.19)}$$

and the induced polarisation at the optical frequency $E_{(\omega)}$is

$$P_{(\omega)} = \overbrace{\varepsilon_0\left(\chi^{(1)}E_{(\omega)}\right)}^{1} + \overbrace{3\varepsilon_0\left(\chi^{(3)}{E_{(0)}}^2 E_{(\omega)}\right)}^{2} \qquad \text{(A.20)}$$

Again term 1 is the linear component at the optical frequency and term 2 is the non-linear component at the optical frequency, i.e.

$$P_{NL(\omega)} = \varepsilon_0\,\Delta\chi E(\omega) = 3\varepsilon_0\left(\chi^{(3)}{E_{(0)}}^2 E_{(\omega)}\right) \qquad \text{(A.21)}$$

where $$\Delta\chi = 3\,\chi^{(3)}{E_{(0)}}^2 \qquad \text{(A.22)}$$

Again substituting $\Delta\mathrm{n} = -\frac{1}{2}\mathrm{n}^3\ \mathfrak{s}{E_{(0)}}^2$ into $\Delta\chi = 2\mathrm{n}\Delta\mathrm{n}$, an expression for $\mathfrak{s}$ in terms of $\chi^{(3)}$ can be obtained i.e. $\Delta\chi = 2\mathrm{n}\Delta\mathrm{n} = -\mathrm{n}^4\ \mathfrak{s}{E_{(0)}}^2 = 3\chi^{(3)}{E_{(0)}}^2$ and rearranging

$$\mathfrak{s} = {}^{-3\chi^{(3)}}\!/_{\mathrm{n}^4} \qquad \text{(A.23)}$$

The alternate notation described in equation (A.7) above is rarely used to describe third order non-linearities, however it can be derived by equating the third order non-linear coefficients in equations (A.6) and (A.7) to obtain.

$$\mathfrak{s} = {}^{-12\mathcal{X}^{(3)}}\!/_{\varepsilon_0\mathrm{n}^4} \qquad \text{(A.24)}$$

Appendix B Tensors for poling – polarisation dependence, symmetry considerations and notation conventions

The following is an analysis of the tensor manipulations that allow the non-linear susceptibilities to be simplified to a more manageable form. To do this some basic properties of tensors such as permutation symmetry are explained along with a study of an isotropic poled dielectric.

B.1 Power series

A function $f(x)$ can typically be expanded in a power series

$$f(x) = \sum_{n=0} a_n x^n = f(0) + \sum_{n=1} a_n x^n \tag{B.1}$$

with a useful domain of convergence which without loss of generality we may assume to include $x = 0$. The coefficients a_n are uniquely determined in the sense that if also $f(x) = \sum_{n=0} b_n x^n$ in a common region of convergence then $a_n = b_n$, all n. Consider now a power series expansion of a function of two variables $f(x_1, x_2)$

$$f(x_1, x_2) = f(0,0) + \gamma_i x_i + \gamma_{ij} x_i x_j + \gamma_{ijk} x_i x_j x_k + \gamma_{ijkl} x_i x_j x_k x_l \ldots \tag{B.2}$$

where the summation convention has been used. The main difference from equation (B.1) is that the coefficients γ cannot be unique beyond the linear term. For example, writing out the quadratic term

$$\gamma_{11} x_1^2 + \gamma_{12} x_1 x_2 + \gamma_{21} x_2 x_1 + \gamma_{22} x_2^2 = \gamma_{11} x_1^2 + (\gamma_{12} + \gamma_{21}) x_1 x_2 + \gamma_{22} x_2^2 \tag{B.3}$$

Only the sum of γ_{12} and γ_{21} is determined by the given function $f(x_1, x_2)$, and in order to fully define the γ_{ij} we may assume that

$$\gamma_{ij} = \gamma_{ji} \tag{B.4}$$

Similarly for the higher order terms in the expansion of B.2 we may without loss of generality assume that $\gamma_{ij\,...k} = \gamma_{ab\,...c}$ where $[a, b \,...\, c]$ is any permutation of $[i, j \,...\, k]$. Let us now consider possible symmetries with respect to rotation in the x_1, x_2 plane

$$\begin{bmatrix} x_1^{'} \\ x_2^{'} \end{bmatrix} = R \begin{bmatrix} x_1 \\ x_2 \end{bmatrix} = \begin{bmatrix} \cos\theta & \sin\theta \\ -\sin\theta & \cos\theta \end{bmatrix} \begin{bmatrix} x_1 \\ x_2 \end{bmatrix} \tag{B.5}$$

We shall assume that $f(x_1, x_2)$ is invariant under rotation, i.e. that it is a scalar – or in other words, just a function of the radius $\sqrt{x_1^2 + x_2^2}$. This has implications for the symmetries of the the γ's in each of the terms of the expansion B.2 – in addition to their symmetry with respect to permutation of subscripts. Not only must the sum of the series on the right hand side of equation B.2 be scalar but so must each term be scalar. If we write R_{ij} for the i, j element of the 2×2 matrix R, we can show that because of the scalar property of f, for the general term in the expansion

$$\gamma_{ijk}^{'} = R_{ia} R_{jb} \,..\, R_{kc} \gamma_{ab\,..c} \tag{B.7}$$

Equation B.7 can be expressed in words by saying that $\gamma_{ij\,..k}$ is a tensor with respect to the rotation set out in equation B.5 of rank equal to the number of subscripts. A derivation of the property expressed by equation B.7 is given below in the context of poling.

B.2 Poling optical fibre

From electromagnetic theory, and in the usual notation, **D** and **E** are ordinary 3D vectors, i.e. they transform under rotation of the coordinate system according to

$$\mathbf{E}^{'} = R\mathbf{E} \tag{B.8}$$

We take it that **E** is the column vector whose components are in order the x, y, z cartesian components of the electric field (and that is **D** similarly specified). The rotation matrix R is then a 3×3 matrix whose elements are defined by the rotation, and can in general be specified by three “Euler angles”', or in other ways. It is probably enough for our purposes to illustrate R for a familiar case, rotation about a single axis - say the z axis. Then

$$R = \begin{bmatrix} \cos\theta & sin\,\theta & 0 \\ -\sin\theta & \cos\theta & 0 \\ 0 & 0 & 1 \end{bmatrix} \tag{B.9}$$

where θ is the angle of rotation. One can confirm that this represents correctly, with positive θ, a positive rotation of the coordinate axes. We could here adopt the alternative view, that R is to represent a rotation of an object such as the **E** field, rather than a rotation of the coordinate system. One does not usually have to worry about which it is, so long as one is consistent. In any case there is only a change of sign.

The Euler angle representation of a general rotation is as a product of rotations about three successive axes- say y then the new z and then the final y axis. But it means that the general rotation is a product of three matrices more or less like B.9. These matrices are real and orthogonal and so is their product. A real matrix A is said to be orthogonal if

$$A^T = A^{-1}\ or\ AA^T = 1 \tag{B.10}$$

where A^T means the transpose of A. If matrices A and B are orthogonal so is their product

$$(AB)^T = B^T A^T = B^{-1} A^{-1} = (AB)^{-1} \tag{B.11}$$

So any rotation matrix R is real and orthogonal.

From the fact that **D** and **E** transform according to equation B.8 it follows that the dot product **D.E** is a scalar. In terms of the components

$$\mathbf{D}.\mathbf{E} = \sum_{i=1}^{3} D_i E_i \tag{B.12}$$

is a scalar. Calling a quantity a scalar in this context means that it is invariant under rotation. We can establish this invariance by the properties of a general rotation. Indicating a rotated quantity by a superscript dash, and using the index summation convention for simplicity

$$\begin{aligned}(D_i E_i)' = D_i{}' E_i{}' &= R_{ip} D_p R_{iq} E_q = R_{ip} R_{iq} D_p E_q \\ &= \delta_{pq} D_p E_q = D_p E_p \end{aligned} \tag{B.13}$$

Equation B.13 provides an example of what is called contraction in tensor analysis, viz a summation over repeated indices. This reduces a tensor of rank n to one of rank $n-2$. Here, a tensor of rank 2, $T_{pq} = D_p E_q$, is reduced to a tensor of rank zero, that is a scalar, $T_{pp} = D_p E_p$.

In the particular application of interest,

$$D = \varepsilon_0(\mathbf{E} + \mathbf{P}) \tag{B.14}$$

where **P** is necessarily an ordinary Cartesian vector like **D** and **E.** The physical significance of **P** is the electric dipole moment per unit volume. It is standard practice, and appears reasonable, to express **P** as a power series expansion in the components of the electric field. For the i component P_i of **P**, and using the tensor summation convention

$$P_i = \varepsilon_0\left(\chi_{ij}^{(1)} E_j + \chi_{ijk}^{(2)} E_j E_k + \chi_{ijkl}^{(3)} E_j E_k E_l + \cdots\right) \tag{B.15}$$

At this point the χ 's are just coefficients of a power series expansion. But they have tensor properties which follow from the fact that $E_i P_i$ is a scalar (cf equation B.13) or the equivalent fact that P_i is a tensor of rank 1 (an ordinary 3D vector under rotation). Consider the $\chi^{(3)}$contribution to the invariant (i.e.scalar) quantity $E_i P_i$. This term has four E field factors, it is quartic in the components of the electric field. Because equation B.15 is an identity, i.e. true for all (real) values of the components E_1, E_2, E_3 of the electric field, the scalar property must hold not only for the sum of the series but for each term. So

$$\chi^{(3)}_{ijkl} E_i E_j E_k E_l \tag{B.16}$$

is a scalar quantity. It follows from this that the coefficients $\chi^{(3)}_{ijkl}$ form a fourth rank tensor. While it can be directly inferred from the form of the expression equation B.16 together with the fact that it is as a whole scalar, we can plod through the derivation as follows. Denoting the values in a rotated coordinate system by a dash

$$\chi^{(3)'}_{ijkl} E_i' E_j' E_k' E_l' = \chi^{(3)}_{ijkl} E_i E_j E_k E_l \tag{B.17}$$

Now the left hand side of equation (B.17) may equally be written

$$\chi^{(3)'}_{pqvw} E_p' E_q' E_v' E_w' = \chi^{(3)'}_{pqvw} R_{pi} E_i R_{qj} E_j R_{vk} E_k R_{wl} E_l \tag{B.18}$$

and the right hand side of equation B.17 must be equal to this so

$$\chi^{(3)'}_{pqvw} R_{pi} E_i R_{qj} E_j R_{vk} E_k R_{wl} E_l = \chi^{(3)}_{ijkl} E_i E_j E_k E_l \tag{B.19}$$

This last equation in the components of the electric field is an identity and so the coefficients of each term must be equal

$$\chi^{(3)}_{ijkl} E_i E_j E_k E_l = \chi^{(3)'}_{pqvw} R_{pi} R_{qj} R_{vk} R_{wl} \tag{B.20}$$

By multiplying the last equation on both sides by $R_{ai} R_{bj} R_{jk} R_{dl}$ we obtain

$$\begin{aligned} \chi^{(3)}_{ijkl} R_{ai} R_{bj} R_{jk} R_{dl} &= \chi^{(3)'}_{pqvw} R_{pi} R_{qj} R_{vk} R_{wl} R_{ai} R_{bj} R_{jk} R_{dl} \\ &= \chi^{(3)'}_{pqvw} \delta_{pa} \delta_{qb} \delta_{vc} \delta_{wd} = \chi^{(3)'}_{abcd} \qquad \text{or} \\ \chi^{(3)'}_{abcd} &= R_{ai} R_{bj} R_{jk} R_{dl} \chi^{(3)}_{ijkl} \end{aligned} \tag{B.21}$$

This last equation is the transformation rule for a fourth rank tensor. Any term in the expansion equation B.15 can be shown in the same way to have coefficients which are nth order tensors.

Without loss of generality these tensors may be defined to be symmetric with respect to permutation of the subscripts, as illustrated in the above preface (paragraph following equation B.4), and independently of any other symmetries which the situation may possess or lack.

B.3 Symmetries of the poled substance

(a) Isotropic

Let us suppose that the poled substance is isotropic. We consider the implications for $\chi^{(3)}_{ijkl}$. The quantity

$$\mathbf{D}.\mathbf{E} = \varepsilon_0(\mathbf{E}+\mathbf{P}) \quad \text{or} \quad D_iE_i = \varepsilon_0 E_i(E_i + P_i) \tag{B.22}$$

is the energy density and is in principle observable. It is also a scalar, that is, if the same rotation is applied both to the material and to the field, the result is unchanged. This much is true whether or not the material is isotropic. The second term on the right hand side of equation B.22 is that part of the energy density arising from polarisation of the medium, and may be taken as a measure of the response of the medium to the field E_i. In an isotropic medium therefore

$$E_iP_i \tag{B.23}$$

is independent of the direction of the field (but not independent of its magnitude). Let us consider three fields with only one component different from zero and with the same magnitude

$$[E_1, E_2, E_3] = [A, 0,0] \ or \ [0, A, 0] \ or \ [0,0, A] \tag{B.24}$$

or equivalently

$$E_i = A\delta_{i1} \; or \; A\delta_{i2} \; or \; A\delta_{i3} \tag{B.25}$$

where δ_{ij} is the Dirac delta function.

For these three fields the value of the expression B.23 must be the same. For the first field $E_i = A\delta_{i1}$

$$E_i P_i = \varepsilon_0\left(\chi_{ij}^{(1)} E_i E_j + \chi_{ijk}^{(2)} E_i E_j E_k + \chi_{ijkl}^{(3)} E_i E_j E_k E_l + \cdots\right) \tag{B.26}$$

$$= \varepsilon_0\left(\chi_{11}^{(1)} A^2 + \chi_{111}^{(2)} A^3 + \chi_{1111}^{(3)} A^4 + \cdots\right) \tag{B.27}$$

Since the quantity B.27 is independent of the direction of the field, it must be the same for the other two fields in the expression B.25. This gives three power series expansions for the same quantity and these must be equal, and indeed equal term by term so that for an isotropic material

$$\chi_{i..i}^{(n)} \tag{B.28}$$

is independent of i or in other words the same for $i = 1, 2, or\ 3$. In particular

$$\chi_{1111}^{(3)} = \chi_{2222}^{(3)} = \chi_{3333}^{(3)} \tag{B.29}$$

Let us now consider the case in which just the first two elements of $[E_1, E_2, E_3]$ differ from zero, say

$$[E_1, E_2, E_3] = A[\cos\theta, sin\theta, 0] \tag{B.30}$$

This field changes direction with θ, and has constant magnitude A. For this field and writing c, s for $\cos\theta, sin\,\theta$

$$\begin{aligned} \frac{E_i P_i}{\varepsilon_0} &= \chi_{ij}^{(1)} E_i E_j + \chi_{ijk}^{(2)} E_i E_j E_k + \chi_{ijkl}^{(3)} E_i E_j E_k E_l + \cdots \\ &= A^2\left(\chi_{11}^{(1)} c^2 + \chi_{22}^{(1)} s^2 + 2\chi_{12}^{(1)} cs\right) \\ &\quad + A^3\left(\chi_{111}^{(2)} c^3 + 3\chi_{112}^{(2)} c^2 s + 3\chi_{122}^{(2)} c^2 s + \chi_{222}^{(2)} s^3\right) + \cdots \end{aligned} \tag{B.31}$$

For the moment we have shown the series only as far as the $\chi^{(2)}$ terms. We have made partial use of the fact that the χ's are unaffected by a permutation of the subscripts to shorten the expressions, for example among the χ's we need only $\chi_{111}^{(2)}, \chi_{222}^{(2)}, \chi_{112}^{(2)}$ and $\chi_{122}^{(2)}$. Each term in the expansion in powers of A must be independent of θ. Looking at the term in A^2, this must have the same value for $\theta = 0$ and for $\theta = {}^{\pi}/_{2}$, so

$$\chi_{11}^{(1)} = \chi_{22}^{(1)} \tag{B.32}$$

The factor multiplying A^2 is therefore equal to
$\chi_{11}^{(1)}(c^2 + s^2) + 2\chi_{11}^{(1)}cs = \chi_{11}^{(1)} + 2\chi_{11}^{(1)}cs$ and for this to be independent of θ we must have $\chi_{12}^{(1)} = 0$.
The two other selections of pairs of non-zero field components lead to similar results. Putting these together we find that for an isotropic medium, the second order response tensor satisfies the constraints

$$\chi_{ij}^{(1)} = \chi_{11}^{(1)}\delta_{ij} \tag{B.34}$$

or in other words is a multiple of the unit tensor. It says that the dielectic matrix is a multiple of the unit matrix.

Let us now look at the term in A^3 in the expansion B.31. For $\theta = 0$ the value is $\chi_{111}^{(2)}$ and for $\theta = {}^{\pi}/_{2}$ it is $\chi_{222}^{(2)}$ and for $\theta = -{}^{\pi}/_{2}$ it is $-\chi_{222}^{(2)}$. Hence $\chi_{111}^{(2)} = \chi_{222}^{(2)} = 0$ and by extension also $\chi_{333}^{(2)} = 0$. The factor multiplying A^3 in equation B.31 is thus
$3\chi_{112}^{(2)}c^2s + 3\chi_{122}^{(2)}c^2s$. This remaining term must be independent of θ. Again setting $\theta = 0, \pm {}^{\pi}/_{2}$ shows that $\chi_{112}^{(2)}$ and $\chi_{122}^{(2)}$ are zero. Hence, for an isotropic material

$$\chi_{ijk}^{(2)} = 0, all\ i, j, k \tag{B.35}$$

Let us now deal with the item of main interest, the factor multiplying A^4 in the expansion B.31. This factor is

$$\chi^{(3)}_{1111}c^4 + 4\chi^{(3)}_{1112}c^3s + 6\chi^{(3)}_{1122}c^2s^2 + 4\chi^{(3)}_{1222}cs^3 + \chi^{(3)}_{2222}s^4 \qquad \text{(B.36)}$$

Here, as in equation B.31 we have used the permutability of the subscripts. The coefficient of $\chi^{(3)}_{1112}c^3s$ is 4 because there are 4 permutations giving 4 equal items (and with the same factor c^3s) viz $\chi^{(3)}_{1112}, \chi^{(3)}_{1121}, \chi^{(3)}_{1211}, \chi^{(3)}_{2111}$. When two subscripts are different as in $\chi^{(3)}_{1122}$ there are similarly 6 equal terms (the number of ways of selecting two items from four without regard to order, $4!/_{2!\,2!} = 6$). The expression B.36 must be independent of θ. Its values for $\theta = 0, \pi/_2$ are $\chi^{(3)}_{1111}$ and $\chi^{(3)}_{2222}$ which are therefore equal, and by extension also equal to $\chi^{(3)}_{3333}$.

$$\chi^{(3)}_{1111} = \chi^{(3)}_{2222} = \chi^{(3)}_{3333} \qquad \text{(B.37)}$$

For $\theta = \pi/_4$ the expression B.36 has the value $\frac{1}{2}\chi^{(3)}_{1111} + \chi^{(3)}_{1112} + \frac{3}{2}\chi^{(3)}_{1122} + \chi^{(3)}_{1222}$ where we have used the fact that $\chi^{(3)}_{1111}$ and $\chi^{(3)}_{2222}$ are equal. For $\theta = -\pi/_4$ the expression B.36 has the value $\frac{1}{2}\chi^{(3)}_{1111} - \chi^{(3)}_{1112} + \frac{3}{2}\chi^{(3)}_{1122} - \chi^{(3)}_{1222}$. From the equality of the last two expressions

$$\chi^{(3)}_{1112} + \chi^{(3)}_{1222} = -\chi^{(3)}_{1112} - \chi^{(3)}_{1222} = 0 \qquad \text{(B.38)}$$

$$\text{and so } \chi^{(3)}_{1112} = -\chi^{(3)}_{1222} \qquad \text{(B.39)}$$

Substituting into the expression B.36 from the last two equations, we find that the following shorter expression must be independent of θ

$$\chi^{(3)}_{1111}(c^4 + s^4) + 6\chi^{(3)}_{1122}c^2s^2 + 4\chi^{(3)}_{1112}(c^3s - cs^3) \qquad \text{(B.40)}$$

Reversing the sign of θ reverses the sign of the last term in the expression B.40, and leaves the first two terms the same, so the last term must be equal to its opposite, and consequently $\chi^{(3)}_{1112} = 0$. By extension

$$\chi^{(3)}_{1112} = \chi^{(3)}_{1113} = \chi^{(3)}_{2221} = \chi^{(3)}_{2223} = \chi^{(3)}_{3331} = \chi^{(3)}_{3332} = 0 \tag{B.41}$$

Substituting into the expression B.40 from the equations B.41 we obtain the shorter expression, which must be independent of θ

$$\chi^{(3)}_{1111}(c^4 + s^4) + 6\chi^{(3)}_{1122}c^2 s^2 \tag{B.42}$$

Substituting $c^2 = 1 - s^2$ we find the following expression to be independent of θ

$$\chi^{(3)}_{1111} + (s^2 - s^4)(6\chi^{(3)}_{1122} - 2\chi^{(3)}_{1111}) \tag{B.43}$$

The first term $\chi^{(3)}_{1111}$ is constant by construction, and the second can be independent of θ only if

$$\chi^{(3)}_{1111} = 3\chi^{(3)}_{1122} \tag{B.44}$$

Summing up and extending: for an isotropic material, only two kinds of $\chi^{(3)}_{ijkl}$ are different from zero (1) those with all subscipts the same such as $\chi^{(3)}_{1111}$ and (2) those with just two different subscripts such as $\chi^{(3)}_{1122}$. The members of the first class have a common value, as do the members of the second class, and the common value of the first class is 3 times that of the second. All elements of χ are independent of any permutation of the subscripts.

B.4 Neumann's principle

The symmetry properties used in section B.3 above are bound by the fundamental postulate known as Neumann's principle. Neumann's principle can be used in systems/materials that exhibit spatial symmetry. Crystals, amorphous glasses and individual molecules are examples of systems that have spatial symmetry properties and that are of particular interest in non-linear optics. Simply stated Neumann's principle requires that any physical property of the system must include all the characteristic point symmetries of the system. In the case of the susceptibility tensor all the elements of χ^{η} represent physical properties that must be invariant under any transformation of coordinate systems that satisfy the spatial symmetry of the system.

In the case of the isotropic material presented above it is this basic postulate i.e. Neumann's principle that allows for arbitrary choice of co-ordinates.

B.5 Shorthand notation

The permutation symmetry discussed in section B.2 above results in many of the elements in the susceptibility tensors being equal e.g. $\chi_{(ijk)}=\chi_{(ikj)}$. This allows for the use of a shorthand notation where pairs of indices (*i*,*j*) are replaced by a shorthand index (*I*). The table below gives a commonly used recipe for the shorthand indices and the second and third order susceptibility tensors $\chi_{(ijk)}$, and $\chi_{(ijkl)}$ are typically written as $\chi_{(iK)}$ *and* $\chi_{(IK)}$ respectively.

j:	*i*:1	2	3
1	1	6	5
2	6	2	4
3	5	4	3

Table 1: Look up table for the index *I*, i.e. shorthand notation of pairs of indices (*i*,*j*)

Table 1 above can be used to generate a label *I* that represents a pair of indices (*i*,*j*). For example pairs of indices (1,3) and (3,1) are both labelled I=5.

B.6 Notation conventions and variations

The scalar form of the polarisability was presented in A.3 above using the following two alternative notations

$$P = \varepsilon_0(\chi^{(1)}E + \chi^{(2)}E^2 + \chi^{(3)}E^3) \tag{B.45}$$

or

$$P = \varepsilon_0\mathcal{X}^{(1)}E + 2dE^2 + 4\mathcal{X}^{(3)}E^3 \tag{B.46}$$

where the second order susceptibility coefficient is represented by d in B.46. The tensor form of d is often presented in the literature using the shorthand notation i.e. d_{iK}. Similarly the Pockels and Kerr coefficients are often presented in their shorthand tensor forms as

$$\mathfrak{r}_{iK} = -4\, {}^{d_{iK}}\!\big/_{\varepsilon_0 \mathrm{n}^4} = {}^{2\chi^{(2)}_{iK}}\!\big/_{\mathrm{n}^4} \text{ and} \tag{B.47}$$

$$\mathfrak{s}_{IK} = {}^{-12\chi^{(3)}_{IK}}\!\big/_{\varepsilon_0 \mathrm{n}^4} \tag{B.48}$$

Discussions in the literature regarding electro-optic responses in poled optical fibres will commonly present values for $\mathfrak{r}$ and/or $\mathfrak{r}_{iK}$. The $\mathfrak{r}$ value is often used when no discussion of the tensor nature of $\mathfrak{r}$ is included. When polarisation dependence is included in the discussion the $\mathfrak{r}_{iK}$ value is presented. When $\mathfrak{r}_{iK}$ is used, the poling direction (or axis), and the corresponding subscript, is assigned the value of 3. Similarly, the propagation direction is assigned the value of 2 and the orthogonal axis 1. If the poled fibre is then probed with light polarised in the poling direction the $\mathfrak{r}_{33}$ value is presented, and $\mathfrak{r}_{31}$ is used if the probe is polarised in the orthogonal direction. The same assignment of axes is often used when discussing the second order non-linear coefficient d_{iK} i.e d_{33} and d_{31}.

Appendix C Phase and Group Birefringence in single mode fibres

The birefringence of an optical fibre describes the difference between the effective refractive indices for the two polarisation modes. The phase birefringence and group birefringence may be defined as the difference between the phase and group refractive indices respectively. The phase birefringence is important when considering cross talk between the two polarisation modes. The group birefringence results in polarisation mode dispersion.

(a) Phase and group birefringence

The phase (or modal) birefringence is defined as,

$$B_m = \left|n_{eff}^{x} - n_{eff}^{y}\right| = \Delta n_{eff} \tag{C.1}$$

where n_{eff}^{x} and n_{eff}^{y} are the effective phase (or modal) refractive indices of the x and y polarised modes. In birefringent single mode fibres, with step index cross sections, the light in each polarisation mode samples both the core and the inner cladding region. The effective index is essentially the average index seen by the mode and can be calculated by evaluating the overlap integral between the fibre cross section and the mode distribution itself.

Similarly the group birefringence can be defined as

$$B_g = \left|n_g^{x} - n_g^{y}\right| = \Delta n_g \tag{C.2}$$

where n_g^{x} and n_g^{y} are the group refractive indices of the x and y polarised modes.

The phase and group velocities in a single mode fibre are more familiar concepts. The phase velocity is defined as

$$V_p = {}^{c}/_{n_{eff}} = {}^{\omega}/_{\beta} \tag{C.3}$$

where V_p is the phase velocity and n_{eff} is the phase refractive index.

Similarly the group velocity is defined as

$$V_g = {}^{c}/_{n_g} = {}^{d\omega}/_{d\beta} \tag{C.4}$$

where V_g is the group velocity, ω is the angular frequency and β is the modal propagation constant.

To formulate a relationship between the phase and group birefringence we need to consider the relationship between the phase and group velocity. The group velocity ${}^{d\omega}/_{d\beta}$ can be expanded as follows.

$${}^{d\beta}/_{d\omega} = {}^{d\beta}/_{d\lambda} \cdot {}^{d\lambda}/_{d\omega} \tag{C.5}$$

Using $c = 2\pi\omega\lambda$ and rearranging $\omega = {}^{c2\pi}/_{\lambda}$ to obtain

$${}^{d\omega}/_{d\lambda} = -{}^{c2\pi}/_{\lambda^2} \tag{C.6}$$

Substituting equation (C.6) into (C.5) gives

$${}^{d\beta}/_{d\omega} = {}^{-d\beta}/_{d\lambda} \cdot {}^{\lambda^2}/_{c2\pi} \tag{C.7}$$

Now, $\beta = {}^{n_{eff}\,2\pi}/_{\lambda}$, and ${}^{d\beta}/_{d\lambda} = 2\pi\left({}^{1}/_{\lambda}\,{}^{dn_{eff}}/_{d\lambda} - {}^{n_{eff}}/_{\lambda^2}\right)$ (C.8)

The group index $n_g = c\,{}^{d\beta}/_{d\omega}$ can be evaluated by using C.7 and C.8 to obtain

$$n_g = C\, {}^{d\beta}\!/_{d\lambda}\, {}^{d\lambda}\!/_{d\omega} = \left(n_{eff} - \lambda\, {}^{d_{neff}}\!/_{d\lambda}\right) \tag{C.9}$$

The group birefringence is then found by evaluating $B_g = \left|n_g^x - n_g^y\right| = \Delta n_g$ substituting n_{eff}^x and n_{eff}^y for n_{eff}

$$\left|\Delta n_g\right| = \left|n_g^x - n_g^y\right| = \left|\left(n_{eff}^x - \lambda\, {}^{dn_{eff}^x}\!/_{d\lambda}\right) - \left(n_{eff}^y - \lambda\, {}^{dn_{eff}^y}\!/_{d\lambda}\right)\right|$$

$$= \left|\Delta n_{eff} - \lambda\left({}^{d\Delta n_{eff}}\!/_{d\lambda}\right)\right|$$

$$\left|\Delta n_g\right| = B_g = \left|\Delta B_m - \lambda\left({}^{dB_m}\!/_{d\lambda}\right)\right| \tag{C.10}$$

In summary, C.10 relates the phase and group birefringence and as discussed in chapter 2 if the phase birefringence is independent of wavelength then the derivative term vanishes and the group and phase birefringence are equal.

(b) Retardance in birefringent fibre

If light is launched into the two modes of a birefringent optical fibre then the relative phase after traveling along a length L will be

$$\phi = {}^{2\pi L B_m}\!/_{\lambda} \tag{C.11}$$

The wavelength dependence of the phase ϕ at the output is described by

$$ {}^{d\phi}\!/_{d\lambda} = 2\pi L\left({}^{dB_m}\!/_{\lambda d\lambda} - {}^{B_m}\!/_{\lambda^2}\right) B_m \tag{C.12}$$

$$ {}^{d\phi}\!/_{d\lambda} = {}^{-2\pi L}\!/_{\lambda^2}\left(B_m - {}^{\lambda B_m}\!/_{d\lambda}\right) = {}^{-2\pi L}\!/_{\lambda^2}\, B_g \tag{C.13}$$

This result C.13 is used in many of the HiBi-PCF characterisation experiments presented in the preceding chapters.

Appendix D References

1. Osterberg, U. and W. Margulis, *Dye laser pumped by Nd YAG laser pulses frequency doubled in a glass optical fiber.* Optics Letters, 1986. **11**(8): p. 516-18.
2. Kazansky, P.G., P. Russell, and H. Takebe, *Glass fiber poling and applications.* Journal of Lightwave Technology, 1997. **15**(8): p. 1484-93.
3. Birks, T.A., J.C. Knight, and P.S.J. Russell, *Endlessly single-mode photonic crystal fiber.* Optics Letters, 1997. **22**(13): p. 961-3.
4. Michie, A., et al., *Temperature independent highly birefringent photonic crystal fibre.* Optics Express, vol.12, no.21, 18 Oct. 2004,, 2004. **12**.
5. Issa, N.A., et al., *Fabrication and study of microstructured optical fibers with elliptical holes.* Optics Letters, 2004. **29**(12): p. 1336-8.
6. Ortigosa-Blanch, A., et al., *Ultrahigh birefringent nonlinear microstructured fiber.* IEEE Photonics Technology Letters, 2004. **16**(7): p. 1667-9.
7. Ortigosa-Blanch, A., et al., *Temperature independence of birefringence and group velocity dispersion in photonic crystal fibres.* Electronics Letters, 2004. **40**(21): p. 1327-9.
8. Ortigosa-Blanch, A., et al., *Highly birefringent photonic crystal fibers.* Optics Letters, 2000. **25**(18): p. 1325-7.
9. Rogers, A.J., *Optical methods for measurement of voltage and current on power systems.* Optics and Laser Technology, 1977. **9**(6): p. 273-83.
10. Rogers, A.J., *Polarization-optical time domain reflectometry: a technique for the measurement of field distributions.* Applied Optics, 1981. **20**(6): p. 1060-74.
11. Smith, A.M., *Polarization and magnetooptic properties of single-mode optical fiber.* Applied Optics, 1978. **17**(1): p. 52-6.
12. Daqing, H. and J. Roberts, *Capacitive voltage transformer: transient overreach concerns and solutions for distance relaying.* 1996 Canadian Conference on Electrical and Computer Engineering. Conference Proceedings. Theme: Glimpse into the 21st Century (Cat. No.96TH8157). IEEE. Part vol.1, 1996: p. 119-25.
13. Saleh.B.E.A and Teich.C.M., *FUNDAMENTALS OF PHOTONICS*. 1994: JOHN WILEY & SONS, INC.

14. Franken, P., et al., *Generation of Optical Harmonics.* Phys Rev Lett, 1961. **7**(4): p. 3.

15. Butcher, P.N. and D. Cotter, *Elements of nonlinear optics*, in *Cambridge University Press.* . 1990. p. xiv+344.

16. Ohmori, Y. and Y. Sasaki, *2-WAVE SUM-FREQUENCY LIGHT GENERATION IN OPTICAL FIBERS.* Ieee Journal of Quantum Electronics, 1982. **18**(4): p. 758-762.

17. Alley, T.G. and S.R.J. Brueck, *Visualization of the nonlinear optical space-charge region of bulk thermally poled fused-silica glass.* Optics Letters, 1998. **23**(15): p. 1170-2.

18. Wong, D., et al., *Frozen-in electrical field in thermally poled fibers.* Academic Press. Optical Fiber Technology: Materials, Devices and Systems, 1999. **5**(2): p. 235-41.

19. Butcher, P.N. and D. Cotter, *Elements of nonlinear optics.* Cambridge University Press. , 1990: p. xiv+344.

20. Michie, A., I. Bassett, and J. Haywood, *Polarisation dependence of the linear electro-optic coefficient in thermally-poled twin-hole silica fibre.* SPIE-Int. Soc. Opt. Eng. Proceedings of the SPIE - The International Society for Optical Engineering, 2004. **5502**(1): p. 366-9.

21. Michie, A., I. Bassett, and J. Haywood, *A low coherence interferometric sensing method with analysis and experimental results for voltage sensing.* SPIE - The International Society for Optical Engineering. Proceedings of the SPIE - The International Society for Optical Engineering, 2005. **5855**(1): p. 206-9.

22. Udd, E., *Fiber Optic Sensors An Introduction for Engineers and Scientists*. 1991: John Wiley % Sons, Inc.

23. Glenn, W.H., *Noise in interferometric optical systems: an optical Nyquist theorem.* IEEE Journal of Quantum Electronics, 1989. **25**(6): p. 1218-24.

24. Rogers, A., *Distributed optical-fibre sensing.* Measurement Science & Technology, 1999. **10**(8): p. R75-99.

25. Rogers, A.J., *Distributed optical-fibre sensors.* Journal of Physics D (Applied Physics), 1986. **19**(12): p. 2237-55.

26. Noda, J., K. Okamoto, and Y. Sasaki, *Polarization-maintaining fibers and their applications.* Journal of Lightwave Technology, 1986. **LT-4**(8): p. 1071-89.

27. Rashleigh, S.C., *Origins and control of polarization effects in single-mode fibers.* Journal of Lightwave Technology, 1983. **LT-1**(2): p. 312-31.

28. Xu, W., *Thermally Poled Fibre Devices*, in *Physics*. 1999, University of Sydney: Sydney.

29. Lee, K., *Poling long lengths of Optical fibre*, in *Physics*. 2006, University of Sydney: Sydney.

30. Marckmann, C.J., et al., *Strength and symmetry of the third-order nonlinearity during poling of glass waveguides.* IEEE Photonics Technology Letters, 2002. **14**(9): p. 1294-6.

31. Kazansky, P.G. and P. Russel, *Thermally poled glass: frozen-in electric field or oriented dipoles?* Optics Communications, 1994. **110**(5-6): p. 611-14.

32. Deparis, O., et al., *Enhanced stability of the second-order optical nonlinearity in poled glasses.* Applied Physics Letters, 2004. **84**(24): p. 4857-9.

33. Janos, M., et al., *Growth and decay of the electrooptic effect in thermally poled B/Ge codoped fiber.* Journal of Lightwave Technology, 1999. **17**(6): p. 1037-41.

34. Myren, N. and W. Margulis, *Time evolution of frozen-in field during poling of fiber with alloy electrodes.* Optics Express, vol.13, no.9, 2 May 2005,.

35. Margulis, W., et al. *The Achievements of the GLAMOROUS Proljeect on Poling*. in *Bragg Gratings, Poling and Photosensitivity (BGPP/ACOFT 2005)*. 2005. Sydney, Australia.

36. Honglin, A. and S. Fleming, *Hindering effect of the core-cladding interface on the progression of the second-order nonlinearity layer in thermally poled optical fibers.* Applied Physics Letters, 2005. **87**(10): p. 101108-1-3.

37. Honglin, A., S. Fleming, and G. Cox, *Visualization of second-order nonlinear layer in thermally poled fused silica glass.* Applied Physics Letters, 2004. **85**(24): p. 5819-21.

38. Xu, W., D. Wong, and S. Fleming, *Evolution of linear electro-optic coefficients and third-order nonlinearity during prolonged negative thermal poling of silica fibre.* Electronics Letters, 1999. **35**(11): p. 922-3.

39. Prasad P, U.D., *NONLINEAR OPTICAL AND ELECTROACTIVE POLYMERS*. 1987: PLENUM PRESS.

40. Kielich, S., *Optical second-harmonic generation by electrically polarized isotropic media.* IEEE Journal of Quantum Electronics, 1969. **QE-5**(12): p. 562-8.

41. Alley, T.G., R.A. Myers, and S.R.J. Brueck, *An ion exchange model for extended-duration thermal poling of bulk fused silica.* Bragg Grating, Photosensitivity, and Poling in Glass Fibers and Waveguides: Applications and Fundamentals. Technical Digest. Postconference Edition. Opt. Soc. America. 1997: p. 293-5.

42. Xu, W., et al., *Direct measurement of frozen-in field in thermally poled fibre devices.* ACOFT'98 Proceedings. 23rd Australian Conference on Optical Fibre Technology. IREE Soc. 1998: p. 201-4.

43. Dominic, V. and J. Feinberg, *High-resolution map of the dc electric field in second-harmonic-generating glass.* Journal of the Optical Society of America B (Optical Physics), 1994. **11**(10): p. 2016-22.

44. Blazkiewicz, P., et al., *Mechanism for thermal poling in twin-hole silicate fibers.* Journal of the Optical Society of America B (Optical Physics), 2002. **19**(4): p. 870-4.

45. Kudlinski, A., et al., *Complete characterization of the nonlinear spatial distribution induced in poled silica glass with a submicron resolution.* Applied Physics Letters, 2003. **83**(17): p. 3623-5.

46. Kudlinski, A., et al., *Evidence of second-order nonlinear susceptibility sign reversal in thermally poled samples.* Applied Physics Letters, 2003. **83**(16): p. 3242-4.

47. Quiquempois, Y., A. Kudlinski, and G. Martinelli, *Zero-potential condition in thermally poled silica samples: evidence of a negative electric field outside the depletion layer.* Journal of the Optical Society of America B (Optical Physics), 2005. **22**(3): p. 598-604.

48. Margulis, W. and F. Laurell, *Interferometric study of poled glass under etching.* Optics Letters, 1996. **21**(21): p. 1786-8.

49. Kazansky, P.G., et al., *Thermally poled silica glass: laser induced pressure pulse probe of charge distribution.* Applied Physics Letters, 1996. **68**(2): p. 269-71.

50. Jeunhomme, L.B., *SINGLE-MODE FIBER OPTICS PRINCIPLES AND APPLICATIONS*. OPTICAL ENGINEERING. 1990: MARCEL AND DEKKER, INC.

51. Digonnet, M., *Rare-Earth_Doped Fiber Lasers and Amplifiers*. 1993: Marcel Dekker, Inc.

52. Issa, N.A. and L. Poladian, *Vector wave expansion method for leaky modes of microstructured optical fibers.* Journal of Lightwave Technology, 2003. **21**(4): p. 1005-12.

53. Bansal, N.P. and R.H. Doremus, *Handbook of Glass Properties*. 1986: Orlando, FL: Academic.

54. Xu, W., et al., *Evidence of space-charge effects in thermal poling.* IEEE Photonics Technology Letters, 1999. **11**(10): p. 1265-7.

55. Godbout, N., et al., *Measurement and calculation of electrostrictive effects in a twin-hole silica glass fiber.* Journal of the Optical Society of America B (Optical Physics), 2000. **17**(1): p. 1-5.

56. Buckland, E.L. and R.W. Boyd, *Electrostrictive contribution to the intensity-dependent refractive index of optical fibers.* Optics Letters, 1996. **21**(15): p. 1117-19.

57. Kubota, H., et al., *Absolutely single polarization photonic crystal fiber.* IEEE Photonics Technology Letters, 2004. **16**(1): p. 182-4.

58. Saitoh, K. and M. Koshiba, *Single-polarization single-mode photonic crystal fibers.* IEEE Photonics Technology Letters, 2003. **15**(10): p. 1384-6.

59. Bassett, I., et al., *Elliptically polarizing optical fiber.* SPIE-Int. Soc. Opt. Eng. Proceedings of the SPIE - The International Society for Optical Engineering, 1999. **3860**: p. 501-6.

60. Mohr, F. and F. Schadt, *Bias error in fiber optic gyroscopes due to elasto-optic interactions in the sensor fiber.* SPIE-Int. Soc. Opt. Eng. Proceedings of the SPIE - The International Society for Optical Engineering, 2004. **5502**(1): p. 410-13.

61. Nielsen, M.D., et al., *Modelling birefringence in isolated elliptical core photonic crystal fibers.* LEOS 2001. 14th Annual Meeting of the IEEE Lasers and Electro-Optics Society (Cat. No.01CH37242). IEEE. Part vol.2, 2001: p. 707-8.

62. Szpulak, M., et al., *Influence of temperature on birefringence and polarization mode dispersion in photonic crystal holey fibers.* Proceedings of 2002 4th International Conference on Transparent Optical Networks (IEEE Cat. No.02EX551). IEEE. Part vol.2, 2002: p. 89-92.

63. Suzuki, K., et al., *Optical properties of a low-loss polarization-maintaining photonic crystal fiber.* Optics Express, vol.9, no.13, 17 Dec. 2001,.

64. Jones, J.D.C., et al., *Photonic crystal fibres for sensor applications.* 2002 15th Optical Fiber Sensors Conference Technical Digest. OFS 2002(Cat. No.02EX533). IEEE. Part vol.1, 2002: p. 565-8.

65. Monro, T.M., et al., *Sensing with microstructured optical fibres.* Measurement Science & Technology, 2001. **12**(7): p. 854-8.

66. Laming, R.I. and D.N. Payne, *Electric current sensors employing spun highly birefringent optical fibers.* Journal of Lightwave Technology, 1989. **7**(12): p. 2084-94.

67. Bassett, I.M., *Design principle for a circularly birefringent optical fiber.* Optics Letters, 1988. **13**(10): p. 844-6.

68. Szafraniec, B. and G.A. Sanders, *Theory of polarization evolution in interferometric fiber-optic depolarized gyros.* Journal of Lightwave Technology, 1999. **17**(4): p. 579-90.

69. Blake, J., B. Szafraniec, and J. Feth, *Partially polarized fiber-optic gyro.* Optics Letters, 1996. **21**(15): p. 1192-4.

70. Kim, H.K., et al., *Fiber-optic gyroscope using an air-core photonic-bandgap fiber.* SPIE - The International Society for Optical Engineering. Proceedings of the SPIE - The International Society for Optical Engineering, 2005. **5855**(1): p. 198-201.

71. Tajima, K., et al., *Ultralow loss and long length photonic crystal fiber.* Journal of Lightwave Technology, 2004. **22**(1): p. 7-10.

72. Bassett, L.M., I.G. Clarke, and J.H. Haywood, *Polarization dependence in a Sagnac loop optical fibre current sensor employing a 33 optical coupler.* Proceedings of the SPIE - The International Society for Optical Engineering, 1994. **2360**: p. 596-9.

73. Born, M. and E. Wolf, *Principles of Optics*
Electromagnetic theory of propagation interference and diffraction of light
Sixth edition. 1980, Pergamon Press (Aust) Pty Ltd.

74. Williams, P.A., et al., *Temperature dependence of the Verdet constant in several diamagnetic glasses.* Applied Optics, 1991. **30**(10): p. 1176-8.

75. Xu, W., et al., *Specialty optical fibre for stabilising and enhancing electro-optic effect induced by poling.* Electronics Letters, 2000. **36**(15): p. 1265-6.